Onsets of nuclear deformation from measurments with the ISOLTRAP mass spectrometer

Sarah Naimi

Université Paris 7 Denis Diderot
Formation doctorale: Champs, Particules, Matière

Thèse en vue de l'obtention du diplôme de
docteur de l'université de Paris 7
en physique

Onsets of nuclear deformation from measurements with the Isoltrap mass spectrometer

Présenté par

Sarah NAIMI

Thèse soutenue le mercredi 27 octobre 2010 devant le jury:

Mme **Gerda NEYENS**	Présidente
M. **Elias KHAN**	Examinateur
Mme **Emily LAMOUR**	Rapporteur
M. **Bertram BLANK**	Rapporteur
M. **David LUNNEY**	Directeur de thèse

Remerciements

Cette thèse n'a pas était le fruit de seulement trois années de travail mais de plusieurs années de succession d'évènements et de croisement de plusieurs chemins. J'ai eu la chance de mettre noir sur blanc cette histoire et espère qu'elle pourrait être le commencement d'autres histoires. Je tiens donc à remercier toutes les personnes qui ont contribué de loin ou de près à cette histoire. Je ne pourrai malheureusement citer tout le monde sans que ça prenne des pages et des pages et j'avoue que ma mémoire a tendance à me trahir (ceux qui sont d'un certain âge me comprendront).

Je vais d'abord commencé par ceux qui ont validé et approuvé cette thèse, les membres du jury : Gerda Neyens, Elias Khan, Emily Lamour, Bertram Blank et David Lunney. Je vous remercie tous d'avoir accepté l'invitation de faire partie de mon jury de thèse. Merci Gerda d'être venu de loin et d'avoir fait des efforts pour parler français ainsi pour les corrections et remarques constructives. Merci à Elias d'avoir pris le temps de lire ma thèse et surtout m'expliquer certain points théoriques dans le cadre de cette thèse. Merci aux deux rapporteurs Emily et Bertram qui ont beaucoup contribué à l'amélioration du manuscrit. Emily, c'était un plaisir de discuter avec vous. Les questions que vous m'avez posées lors de nos entretiens m'ont beaucoup appris. Bertram, merci pour les remarques importantes et d'avoir corrigé aussi méticuleusement le manuscrit. Enfin je remercie Dave, mon directeur de thèse, de m'avoir conduit jusqu'au jour J. Il a était maître et guide en même temps. Sa vision de la physique nucléaire a l'élégance d'un poète amoureux d'une déesse. On a qu'une envie en le côtoyant, c'est d'adhéré à son culte. J'ai trouvé en lui les qualités d'un scientifique complet; brillant, précis et en même temps avec une imagination débordante sans jamais perdre sa lucidité de scientifique. Merci Dave de m'avoir enseigné tout cela, tu m'as donné les outils nécessaires pour trouver mon propre chemin.

J'ai eu la chance de travailler dans deux équipes formidables : au CSNSM et aussi à ISOLDE au CERN. J'aimerai d'abord commencer par le corps administratif : Réjane Bodson, Annie Ballouard, Patricia Duarte, Sonia Martineau, Michèle Fréret, Alain Rufas et Jenny Weterings. Merci Réjane pour ta bonne humeur permanente et ton efficacité. Patricia et Sonia, merci pour vos sourires et votre gentillesse et de m'avoir régler tant de problèmes administratifs. Annie et Michèle, merci pour les missions (et les sous) et votre bonne humeur et tout le reste. Alain, merci pour ton accueil chaleureux tous les matins qui me donna le sourire chaque jour. Jenny, merci pour ton aide auprès des services du CERN. Je n'oublie pas notre directeur au CSNSM Gabriel Chardin et aussi notre leadeur de groupe à ISOLDE Yorick Blumenfeld d'avoir soutenu mon travail de thèse. Je tiens aussi à remercier le workshop d'ISOLDE notamment, Ermanno Barbero et Bernard Crepieux qui m'ont sauvé la vie plusieurs fois, merci pour votre efficacité et votre disponibilité. Merci aussi au workshop du CSNSM, grand merci à Stéphane

Cabaret et Silvin Herve.

I would like to thank all Isolde and Isoltrap collaboration. It was really a nice time at Isolde. I would like first to start with the Isoltrap group leader Klaus Blaum for supporting my work and also for being so close and so careful about all the members of his 'crew'. I also would like to thank Lutz Schweikhard for its long but nice and helpful advices and discussions. Also I would like to thank Frank Herfurth, Dietrich Beck, Sebastian George, Alex Herlert, Alban Kellerbauer, Jurgen Kluge and all the collaboration for fruitful discussions.

I also would like to thank my colleagues at Isoltrap: Madga Kowalska, Martin Breitenfeldt, Dennis Neidherr,Christine Böhm, Marco Rosenbusch, Daniel Fink, Robert Wolf, Christopher Borgmann, Susanne Kreim (I hope I didn't forget anyone). Thanks to all of you for the nice time, your hard work and your contribution to my work. Thank you also for making my stay in Geneva a very lovely memory. Thank you very much Martin for teaching me so much about the experimental work and for being a friend and for all your wise advices. Also thanks for your jokes (sometimes very bad but make me laugh anyhow!) and also thanks for cutting my hair so many times. Marco, thanks for introducing me Aikido and for all the nice 'cheese and wine' and playstation evenings that we had together after the Aikido trainings. Christine, thank you for your smile every morning and your good mood the whole day, it was really nice to work in such atmosphere. Daniel, mein Freund, you are my favorite rugby-man, thanks for your good mood and all the coffee-breaks that we had together; it was 'A little warmth in this cold world'. Thank you very much Magda for being my local supervisor, my office mate and also my friend. It was great pleasure to work with you. Building the tape station was a lot of fun but I also learned a lot from you. Thank you also for being my local 'mummy'...

A mon retour du CERN, j'étais accueilli par une équipe formidable au CSNSM qui m'a tout de suite adopté. Georges Audi, Enrique Minaya, Carole Gaulard, Lara Risegari, David Lunney, Georgi Georgiev, Enrico Fiori, Meng Wang, Catherine Thibault, Joa Ljungvall... la liste est encore longue. Merci à tous de m'avoir accueilli si chaleureusement et de m'avoir aidé de loin ou de près dans mon travail. Un grand merci à Georges qui était toujours disponible pour répondre à mes questions et d'avoir était un excellent professeur de rigueur et de précision. Merci pour toutes les discussions très constructives et aussi pour tous les chiffres que tu as sorti de la machine de l'évaluation des masses. Ce travail n'aurai pas été possible sans ta contribution essentielle. Merci de m'avoir donné ta thèse et pour les discussions qui s'en est suivi, j'ai beaucoup appris sur les masses. Merci Enrique pour ton soutien et tes conseils surtout à la fin de ma thèse. Merci aussi pour ton aide à Isoltrap notamment durant les beamtimes, c'était un plaisir de travailler avec toi. Merci à Catherine pour les discussions et tes remarques concernant mon manuscrit et ma présentation de thèse. Merci Carole, Enrico, Lara, Georgi, Joa, Meng pour les pauses café et pour votre bonne humeur et aussi pour toutes les discussions (scientifiques ou pas) qu'on a eu et qui m'ont beaucoup apporté.

Enfin je remercie mes amis et ma famille qui m'ont tant soutenu durant ma thèse et bien avant. Je ne peux commencer que par ceux qui m'ont conçu, mes parents. Merci

Papa pour ton soutien, ta bonne humeur permanente et surtout ton amour. Grande était ma tristesse le jour de ma soutenance, j'aurai aimé que tu vois l'accomplissement de mon travail pour lequel j'ai sacrifié tant d'année loin de toi et que je ne rattraperai hélas jamais. Merci Mama de m'avoir soutenu et encouragé durant toutes ses années. Merci pour ton courage, tes conseils ainsi que ton amour. Merci aussi de m'avoir transmis l'amour de la science. Merci à ma tante Luisa et mon oncle Mouloud, qui m'ont adopté dès mon arrivée en France. Merci de m'avoir soutenu et aimé comme votre propre fille. Grâce à vous je ne sentais pas le vide familial puisque je rentrais le weekend 'chez moi' et je revenais avec les boites en plastique remplie de bons plats préparer avec amour par ma chère tante. J'avais des repas de famille et je fêtais noël avec vous, j'avais même des cadeaux. Merci d'avoir rendu mes années d'études si douces et si agréables. Merci à ma petite soeur Amel, mon frère Naim et sa femme Sara, ma cousine Nawell, ma cousine Assia et tout le reste de la famille (je ne peux citer tout le monde, la liste est encore plus longue) de m'avoir soutenu et encouragé durant mes longues années d'études. Un grand merci à tous mes amis qui m'ont soutenu et aidé de près ou de loin pendant ma thèse : Pauline, Rafik, sa chérie Sarah, Aurélie, Julien, Rym, Sara, Nassima, Michalina, Elian, Larissa, Ladiu, Michel... Merci pour votre amour et soutien durant toutes ces années. Merci Pauline d'avoir lu une bonne partie de ma thèse et de m'avoir écouté pendant des heures répéter ma soutenance de thèse. Tes remarques et corrections m'ont beaucoup aidé à améliorer ma présentation ainsi que mon manuscrit. Merci pour ton amour et ton affection qui m'ont donné tant de courage pour finir cette thèse. Merci pour les petits sauts à Gex lors de tes passages au CERN, ils me manqueront beaucoup ces petites soirées. Merci Rafik pour ta grande écoute et ta patience. Merci pour ton amour qui m'a tant apporté ainsi que les soirées passées à tes côtés en méditant sur un fond de Ganawi, Jazz ou sur un des textes philosophiques que tu aimes tant.

Merci François et Patricia, mes adorables proprios à l'impasse de Genève (à Villebon-sur-Yvette) de m'avoir accueilli chez vous et m'avoir permis d'écrire ma thèse dans une ambiance agréable. Merci François pour les compotes et les desserts que tu préparais pour moi quand je n'avais pas le temps, merci aussi pour toutes BDs que tu me ramenais vue que je n'avais pas le temps non plus de passer à la bibliothèque. Merci à Patricia et la petite Lucille pour votre bonne humeur, je me sentais presque comme un membre de la famille. Merci pour tout!

Merci à tous ceux que je n'ai pas cité et qui m'ont aidé dans la réalisation de ma thèse.

Contents

List of Figures

List of Tables

Mass measurements provide important information concerning nuclear structure. This work presents results from the pioneering Penning trap spectrometer ISOLTRAP at CERN-ISOLDE. High-precision mass measurements of neutron-rich manganese ($^{58-66}$Mn) and krypton isotopes (^{96,97}Kr) are presented, of which the ^{66}Mn and ^{96,97}Kr masses are measured for the first time. In particular, the mass of ^{97}Kr was measured using the preparation trap and required the definition of a new fit function.

In the case of the manganese isotopes, the $N = 40$ shell closure is addressed. The two-neutron-separation energies calculated from the new masses show no shell closure at $N = 40$ but give an estimation of the proton-neutron interaction (around 0.5 MeV) responsible for the increase of collectivity and nuclear deformation in this mass region. The new krypton masses show behavior in sharp contrast with heavier neighbors where sudden and intense deformation is present, interpreted as the establishment of a nuclear quantum shape/phase transition critical-point boundary. The new masses confirm findings from nuclear mean-square charge-radius measurements up to $N = 60$ but are at variance with conclusions from recent gamma-ray spectroscopy.

Another part of this work was the design of new decay spectroscopy system behind the ISOLTRAP mass spectrometer. The beam purity achievable with ISOLTRAP will allow decay studies with γ and β detection coupled to a tape-station. This system has been mounted and commissioned with the radioactive beam ^{80}Rb.

Foreword

Why are we here? One of the oldest questions of humanity. Contrary to what we think, there are many answers to this question[1]. Actually, as many as human imagination can provide and as many as observation tools that humans have built. Here are some answers:

William Shakespeare: "*All that lives must die, passing through nature to eternity.*" - Hamlet, Act 1, Scene 2.

Martin Luther King: "*If a man hasn't discovered something he's willing to die for, he isn't fit to live.*"

Erich Fromm: "*Man's main task in life is to give birth to himself.*"

Albert Einstein: "*A human being is a part of the whole called by us universe, a part limited in time and space. He experiences himself, his thoughts and feelings as something separated from the rest, a kind of optical delusion of his consciousness. This delusion is a kind of prison for us, restricting us to our personal desires and to affection for a few persons nearest to us. Our task must be to free ourselves from this prison by widening our circle of compassion to embrace all living creatures and the whole of nature in its beauty.*"

Peter Deunov: "*We have come to earth to learn to love God who has created and loves us. When we learn how to love Him we shall understand the meaning of our life, and our relationships with others will become clear.*"

Scientists, artists, philosophers, men of faith and every human being have one common goal of finding *the answer*. Each one places his building block and sees how it fits in the '*truth*' edifice. If human beings are still searching for an answer it could be because the existing ones are not satisfactory or maybe it is just because it is more interesting to seek than to find.

The contribution of my thesis to this question is a pebble on the scale of the knowledge nowadays. As one can expect from the title, this work treats the behavior of nuclei; more precisely, deformation of exotic nuclei from mass measurements. Now, why study nuclei? Why exotic? Why their deformation? To understanding some strange features like the $N = 40$ shell closure and a quantum nuclear phase transition? And why do I think that this work is relevant to be in the '*truth*' edifice? I hope this manuscript will answer all these questions.

[1] Thanks to *Google* and *Wikipedia*.

1. Introduction

The nucleus is a fascinating system, very simple but behaving in a very complex way. *Simple* because it has only two components (nucleons): protons and neutrons. *Very complex behavior* because it is one of the standard sentences that scientists use to hide their ignorance. A friend of mine (a computer scientist) told me one day: "*Nuclear physicists are lazy: they are studying nuclei for more than a century and they still don't understand what is happening inside!*". I will not comment on the first part of the sentence but I somehow agree with the second part. The difficulty is coming from the fact that we are studying a quantum bound system of many particles interacting with each others. Each nucleon is interacting with its close neighbors and with the "mean field" created by the whole bound system. This is a very complex system, known also under the name of "many-body problem", usually one cannot make exact and/or analytical calculations due to the complexity of the wave function of the system which holds a large amount of entangled information.

Why exotic nuclei? Most of the exotic nuclei are born before the stable nuclei. These exotic nuclei are usually produced in massive stars and are either neutron-rich or neutron-deficient compared to the proton number. This makes them very unstable and they "die" or decay to give birth to the stable nuclei.

Testing any system in its extreme conditions provides very precious information about its behavior and makes it more predictable. Exoticsm is considered as such for nuclei since the number of protons and neutrons is unbalanced and the nucleus tries to find its stability by converting protons to neutrons or *vice versa* through the β-decay process[1]. Figure 1.1 shows the nuclear chart, the thin black line represents the stable nuclei and the colored regions represent exotic nuclei with different decay modes. Some of our knowledges well established from the study of stable nuclei limp in the first excursion towards exotic nuclei.

Exotic nuclei are produced in nuclear facilities since half a century. Otto Kofoed-Hansen and Karl Ove Nielsen at the Niels Bohr Institute in Copenhagen were the first to perform such an experiment in 1951. Their method, the so-called ISOL (Ion-Source-On-Line) technique, was introduced in 1967 to CERN and the first nuclear facility ISOLDE was born [KH76]. Since then, many other nuclear facilities were built around the world and many studies were performed on these exotic nuclei. Actually, nuclear physicists are not so lazy and we do understand a lot of things about the nuclei from the huge amount of data available. We just cannot connect the dots. The pen we need for that is the nuclear interaction which still has no analytical expression.

[1] is a radioactive decay in which a beta particle (electron or positron) and anti-neutrino or neutrino is emitted which leads to convert a neutron into a proton or a proton into a neutron, respectively.

Why deformations of exotic nuclei? One of the nuclear properties for which the nuclear interaction is responsible is the nuclear shape. Actually, we do not know if some of the nuclei are really deformed since the optical instruments available today don't allow us to see the nucleus. But there are many indirect observations which lead us to this conclusion. If we consider the nucleus isotropic and rotating, we will see no change if it is spherical. If it is deformed then we will see some rotational characteristics, *e.g.* specific γ-rays emitted when the nucleus decays. We can also see the deformation from the distribution of the charge in the nucleus which will tell us how the nucleons are distributed inside the nucleus and gives a hint of deformation. However, this notion of deformation stays very abstract and one can talk about deformation only in the framework of certain models.

Now, why these deformations naturally occur in the nuclei (in the ground state) and especially in exotic nuclei? Actually, we do not know! First we thought we can explain it with the help of the models established from the studies of stable nuclei but with exotic nuclei, it is more and more difficult to use these models to predict and explain deformations. The only thing we can say is: some nuclei prefer being deformed to minimize their energy and we can accuse this unknown nuclear interaction as being responsible of this behavior.

In this work, deformation of the nucleus is studied in two key neutron-rich regions, extremely far from stability: the zirconium region (at $N = 60$) and the nickel region (at $N = 40$). We can consider these two regions as the upper and the lower limit of what is called the medium mass region.

Some of the nuclear models treat the nucleus as particles moving on specific orbitals, these models are more adapted to lighter masses where the nucleus is made of a small number of nucleons. Other models are better adapted to heavy nuclei where the number of nucleons is large and a single particle behavior is washed out. In between, the nucleus seems to have both behaviors and many models get more troubles to follow this *dual* behavior of the nucleus in this mass region. In this work we are interested in the nuclear deformations in the two regions, we tried to treat a specific question in each region: nuclear phase/shape transition for the zirconium region and $N = 40$ magic number for the nickel region. In the zirconium region, by adding only one neutron, the nuclei go from spherical or moderately deformed to strongly deformed. By doing so, the nucleus gains energy in comparison with its lighter neighbor. This sudden change in shape is nicely described in the framework of the Interacting Boson Model (IBM) as a quantum shape/phase transition. In this work, we extended this region by measuring the masses of ^{96,97}Kr in order to understand better this sharp transition. Below the nickel region, we also measured the masses of the more exotic nuclei, $^{58-66}$Mn, aiming to understand the magicity at $N = 40$ already announced and shown to be very weak in this region. Let us remind the reader that the magic numbers are these proton or neutron numbers for which the nucleus becomes particularly stable and as such, spherical. The evidence of these numbers was confirmed from mass measurements, which thus played an important role in the establishing of the shell model [Els33]. At these numbers the nucleus shows an extra binding energy beyond what it is expected from the smooth systematics of the liquid-drop model[2].

[2]The first nuclear model established by Von Weizsäcker in 1935, which described the nucleus as having

The deformations play a key role in the nickel region and for our understanding of the $N = 40$ shell closure. Through these deformations and from the new mass surface, we tried to see how the internal structure of the nucleus is changing and what could be the impact in the collective behavior. We believe that studying deformations of exotic nuclei is an important key for understanding the nuclear interaction.

What was my work? I had a chance to work at the mother of all ISOL-facilities: ISOLDE, situated at the European Organization for Nuclear Research CERN, the world's largest scientific research center, where the web was born and home of the Large Hadron Collider, the most powerful and gigantic scientific instrument ever built by humans. At ISOLDE, I joined the mass spectrometer experiment ISOLTRAP–also the mother experiment of mass measurements using the Penning trap technique and one of the most powerful techniques in mass spectrometry. I participated in almost all beamtimes from 2007 up to now. I concentrated on the data analysis of the $^{64-66}$Mn and ^{96,97}Kr isotopes (masses measured for the first time), and made the mass evaluation of $^{55,58-66}$Mn, $^{61-63}$Fe and ^{96,97}Kr (the other Mn and Fe isotopes were measured in 2006).

ISOLTRAP has two Penning traps, one for beam preparation (called preparation trap) and the second for high precision mass measurement (called the precision trap). During the krypton beamtime and because of some technical difficulties (see section 4.6), for the first time the preparation trap had to be used as a measurement trap. The analysis of these data was a bit problematic without a new fit function. Dietrich Beck, who made his diploma thesis on the preparation trap in 1993 and his PhD thesis on mass measurements with ISOLTRAP in 1997, proposed a fit function for such data–an idea that he recycled from Georg Bollen (PhD thesis on ISOLTRAP 1989). With this proposed fit function, the preparation trap data was easier to analyze. The use of this trap in this emergency case raises many technical questions about the performance of this trap as a potential measurement trap. These questions will be addressed in section 4.6 as well as the outlook concerning this trap. The simulations presented in this section where performed by Marco Rosenbusch (PhD student since 2009 at ISOLTRAP) who, during his diploma thesis [Ros09] at ISOLTRAP, worked on a program to simulate the ion motion in the preparation trap. These simulations validate the shape of the proposed fit function.

In addition, I worked on the extension of ISOLTRAP for spectroscopy studies: the tape station project. This project consists of a movable tape-transport system (where the ions are implanted) surrounded by beta and gamma detectors. Placed behind the last trap, this system uses ISOLTRAP as a mass separator with a resolving power over 10^6. This resolving power is never reached in standard spectroscopy experiments, which usually use a standard mass separator with resolving power of $500 - 5000$. However, this idea of using a Penning trap as a mass separator was already used by the JYFLTRAP experiment at IGISOL (in Finland) and the SHIPTRAP experiment at GSI (in Germany). These two projects gave very promising results. Installing a similar setup at ISOLDE gives access to a large range of nuclei which cannot be produced with both facilities.

I was deeply involved in all steps of this project, from the simulations and the design to the preparation and the commissioning with exotic beam in 2009. During the commissioning beamtime the half-life of ^{80}Rb was correctly reproduced with this new

the characteristics and behavior of a liquid drop.

decay system as well as the observation of the γ-rays of this nucleus. This opens many opportunities for future measurements and decay studies with ISOLTRAP, and another beamtime is planned for November 2010 where the thallium isotopes will be studied. All the technical details and the result of the commissioning beamtime will be found in Appendix A.

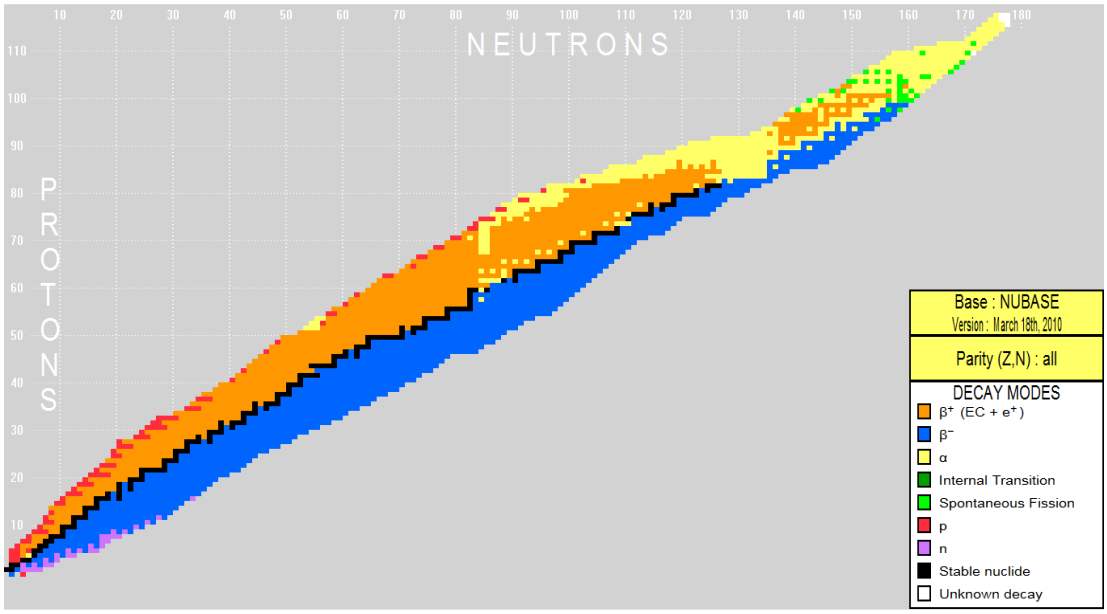

Figure 1.1.: The nuclear chart. Stable nuclei are shown in black and radioactive nuclei in color depending on their decay mode

2. Masses of exotic nuclei

2.1. Importance of masses in physics

In the first part of the last century, Aston discovered a "mass defect" in the nucleus. From mass measurements he found that the nucleus is lighter than the mass of its constituents (masses of all protons and neutrons). It was shown that the missing part of the mass is converted to energy to make this system bound. This missing mass is called the binding energy B. The mass of a nucleus is then defined as:

$$Mc^2 = Nm_nc^2 + Zm_pc^2 - B(N,Z) \tag{2.1}$$

where m_n and m_p are the masses of the neutron and the proton respectively and $B(N,Z)$ is the binding energy of a nucleus with N neutrons and Z protons. To describe this binding energy a simple model was proposed by von Weizsäcker in 1935: the famous *liquid drop model*. The nucleus has some characteristics of a liquid drop of incompressible nuclear matter. The refined version of this model could reproduce the gross features of nuclear binding energies. Comparing experimental masses to the liquid drop model masses, a large deviation was observed at some neutron or proton numbers as illustrated in Figure 2.1. The nucleus does not have only liquid drop characteristics. This deviation at these numbers, called also "*magic numbers*", shows that the nucleus is more bound at these numbers which suggests an internal structure coexisting with the liquid drop picture.

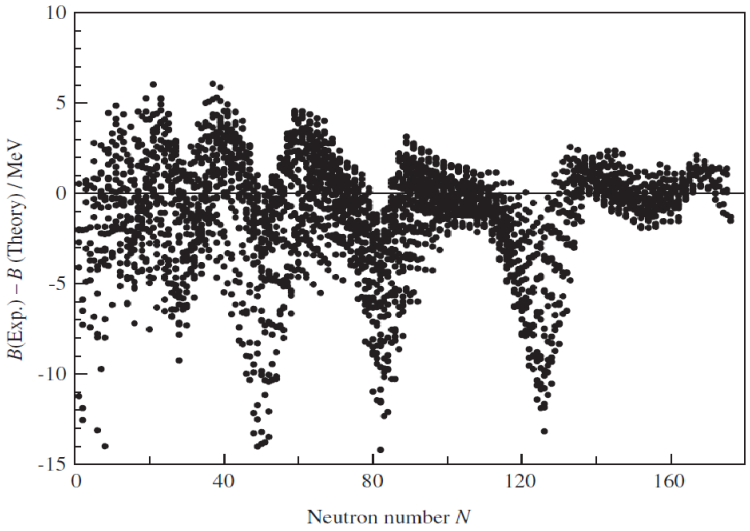

Figure 2.1.: Deviation between the liquid drop model and experimental binding energies as a function of the neutron number [Pea01].

2.1.1. Nuclear structure

Mass measurements played an important role in the establishing of the *shell model*. According to this model, the nucleons occupy certain shell levels or orbitals shown in Figure 2.2. The total number of nucleons in the shells, given in brackets [], indicate level closures. The numbers to the far right of the figure, given in bracketed parenthesis {}, represent shell closures which correspond remarkably well to the observed "*magic numbers*": 2, 8, 20, 28, 50, 82, 126.

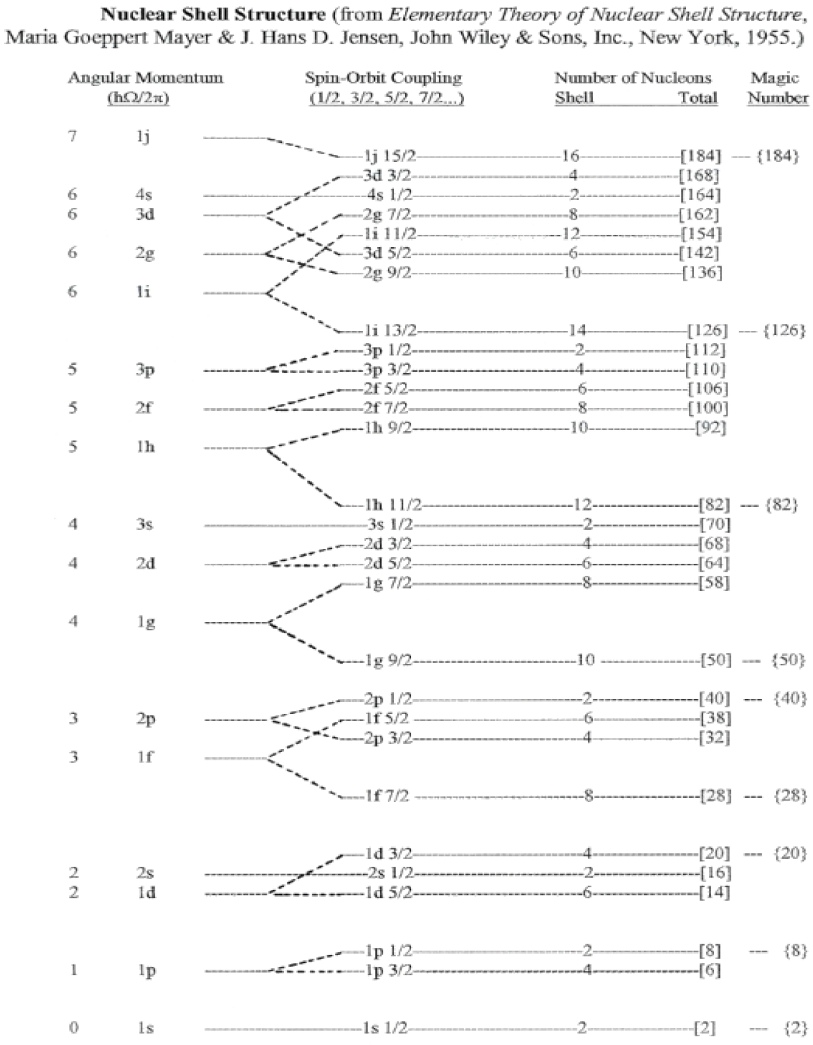

Figure 2.2.: Shell model.

These numbers appear also as discontinuity in the two nucleon separation energies defined as:

$$S_{2n}(N,Z) = B(N,Z) - B(N-2,Z) \qquad \text{for neutrons} \tag{2.2}$$

$$S_{2p}(N,Z) = B(N,Z) - B(N,Z-2) \qquad \text{for protons} \tag{2.3}$$

The general trend of the S_{2n} values is to fall smoothly while the neutron number N increases for a fixed Z. This reflects the proximity to the Fermi level or the neutron drip line where the nucleus is not bound, thus it costs less energy to remove two neutrons when N increases. However, a sudden drop of the S_{2n} values indicates the shell closure since it costs less energy to remove a pair of neutrons outside the closed shell. The behavior of the two-neutron separation energy is illustrated in Figure 2.3 with the S_{2n} values of all elements between indium ($Z = 49$) and hafnium ($Z = 72$) with neutron number from $N = 75$ to 100. The sudden drop at $N = 82$ is a signature of shell closure at this magic number.

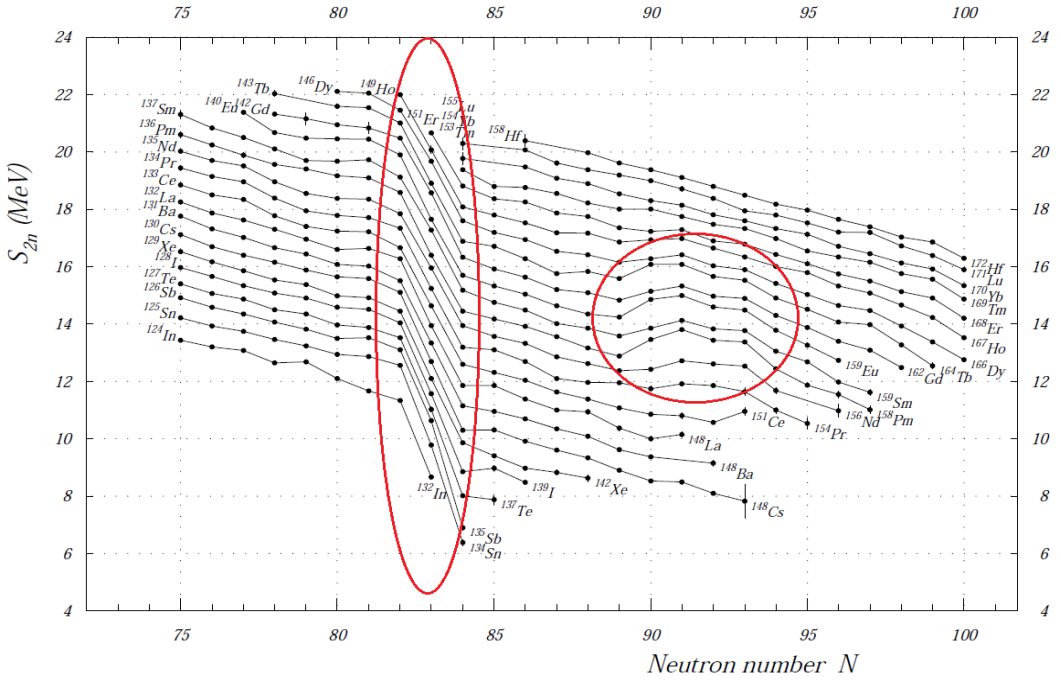

Figure 2.3.: experimental two-neutron separation energies (S_{2n}) plotted as a function of neutron number from $N = 75$ to 100. Each line represents an isotopic chain (same Z). In red is shown the striking signatures of nuclear structure: the shell closure at $N = 82$ and deformation in the rare earth region which appears as a sudden increase in the S_{2n} values (Figure from [AWT03]).

Another manifestation of nuclear structure in the two neutron separation energies can be also seen from abrupt changes. An example is shown in Figure 2.3, the sudden increase of the S_{2n} values in the rare earth region reveals a gain of binding energy which is a result of deformation. This was shown to be due to drastic change of structure when the nuclear shape changes suddenly from spherical to deformed (the deformation will be discussed in section 2.2).

The observation of the behavior of binding energies serves also to establish the pairing disposition of the nucleons. By arranging the protons or the neutrons in pairs, the nucleus gains energy and thus the nuclei with an even number of protons and neutrons are more bound than their even-odd or odd-odd neighbors. In $N = Z$ nuclei, a more delicate phenomenon is discerned through binding energies; the so-called "Wigner effect". These nuclei are more bound than their neighbors, since the protons and neutrons

occupy the same shell-model orbitals and large overlaps between their single-particle wave functions are expected to enhance the neutron-proton correlations.

2.1.2. Testing mass models

The difference between theory and model is the explanatory character of the former. While a theory can explain, describe and predict, a model can only describe and predict in a limited way. In nuclear physics, such a theory does not exist because of the lack of the nucleon-nucleon interaction and the complexity of the many-body nucleonic system. Therefore, one has to consider nuclear models and mass formulas to predict the binding energies. Many models and mass formulas, reviewed in [LPT03], were developed from the 1930s up to now. In general three types of approaches have been used: macroscopic, microscopic-macroscopic and microscopic. The first one describes the nucleus as one body influenced by the collective behavior of its constituent nucleons, the *liquid drop model* for example. In Figure 2.1, the deviation of this model from the experimental binding energies is shown. These deviation can reach up to $15MeV$ at the magic numbers. The *liquid drop model* ignored completely the quantification of the energy or the well-known shell aspect of the nucleus. This led to the second approach, the microscopic-macroscopic model; similar to the first one but with additional quantum-mechanical terms added for shell effects, pairing features, *Wigner* term, etc, [Mol+95].

The microscopic approach is considered as the most realistic. As its name implies it brings the view of the nucleus to the nucleonic perspective. By the treatment of each nucleon moving on a certain orbit and interacting with the other nucleons present in the nucleus, one should describe and predict the behavior of this system. Since the nucleon-nucleon interaction is missing, it is usually replaced by an effective interaction fitted to the experimental data which makes this approach not completely realistic (for HFB model see [RS80]). Many other global approaches and mass formulas tried to overcome this problem, such as the interacting boson model (IBM) [IA87], the Duflo-Zuker mass fomula [DZ95], the Liran-Zeldes mass formula [LZ76], etc. Like the macro, micro-macro and micro models, the other approaches have their weakness and some of them fail completely in certain regions of the nuclear chart. Some comparisons with the new measurements will be made in chapter 6.

2.1.3. Astrophysics

Since the binding energy determines the amount of energy available for reactions and decays, it is of capital importance for stellar nucleosynthesis. Up to nickel, where the binding energy reaches its maximum, the abundance and the production of the chemical elements is somewhat understood. In a very simplified picture, the lighter elements by fusion construct the heavier ones. But this process becomes energetically impossible above nickel since its binding energy is very high. Other processes are responsible for the production of heavier elements such as the r-process (rapid neutron capture). Under extreme conditions (explosion of supernovae or in the accreting neutron stars), the nuclei capture neutrons and then decay via β-decay to stable nuclides. On their way to the stability, the nuclei can capture more neutrons, which makes the process very

complex. The abundance of the elements depends very much on these processes and on their path. The model describing these processes should reproduce the abundance of the stable isotopes. These astrophysical models require nuclear masses of nuclides far from stability. Experimentally, it is not possible to produce these nuclei and a mass model with strong predictive power is crucial to understand these processes. Therefore, experimental data as far as possible from stability are highly needed, which will allow a decisive test of the mass models and provide an extended and reliable basis for the adjustment of their parameters.

2.1.4. Other applications

The weak interaction is the only one in which a quark can change into another type (flavor) of quark or a lepton into another type of lepton. In this transformation, a quark is allowed only to change charge by a unit amount corresponding to the charge of an electron. Since the quarks u, c, and t have a $+2/3e$ charge and d, s, and b have a $-1/3e$ charge, this results in nine possible pairings between the two type of charged quarks and can be represent by a matrix. In the Standard Model of particle physics, this quark mixing matrix is called the Cabibbo-Kobayashi-Maskawa matrix (CKM). This matrix is required to be unitary *e.g.* $|V_{ud}|^2 + |V_{us}|^2 + |V_{ub}|^2 = 1$ in the Standard Model, where V_{ud} is the matrix element which mixes the quark u and d. The proton is constituted of uud and the neutron of udd. The first term V_{ud} can then be related to the beta decay where a proton is converted to a neutron or *vice versa*. It is relevant in this case to look to the super-allowed transitions $0^+ \rightarrow 0^+$ where the orbitals in initial and final states are almost the same. This kind of decay depends uniquely on the vector part of the weak interaction and, according to the conserved vector current (CVC) hypothesis, its experimental ft value should be related (after some corrections) to the vector coupling constant, a fundamental constant that is the same for all such transitions. In order to obtain these ft values, one needs the half-life, the branching ratios and the transition energy between the mother and the daughter nuclei which depends on their masses (the Q values with $Q = \Delta m$). Thus, the binding energies needed to calculate the Q values bring an essential contribution in the Standard Model test (recent results of this application could be found in [HT09]).

Masses can also play an important role in other fields of physics such as testing quantum electrodynamics, definition of the kilogram and fundamental constants, etc. (see [Bla06]).

2.1.5. How precisely should masses be measured?

The mass precision needed depends on the physics and the effects being investigated. For example, in nuclear structure to probe the shell effects one needs a precision of few hundred keV, corresponding to a relative precision better than 10^{-5}. More subtle effects, such as pairing or sub-shell effects, require a relative precision around 10^{-6}.

For astrophysics and testing mass models, a precision of 10-100 keV is sufficient or in terms of relative precision 10^{-6} to 10^{-7}. The study of fundamental interactions and the Standard Model require the highest precision. For example in the study of the super allowed beta emitters, the masses of the mother and the daughter should be measured

with a precision of 1 keV or less, corresponding to relative precision between 10^{-8} and 10^{-9}. Even higher demand on the precision (more than 10^{-9}) could be required for QED tests or the variation of fundamental constants.

2.2. Deformations and phase transitions

"*Lors qu'il arrive quelque changement dans la Nature, la Quantité d'Action, nécessaire pour ce changement, est la plus petite qu'il soit possible.*"

Pierre Louis Moreau de Maupertuis
Histoire de l'Académie Royale des Sciences et des Belles Lettres (1746), p. 267-294

One of the fundamental principles in physics is *the principle of least action* which tells us that every system in nature tends to minimize its action. The system studied here, the nucleus, is very simple since it has only two components: protons and neutrons. As a function of the number of nucleons, this system can have different and unexpected configurations. Deformations are one of such state where the nucleus minimizes its internal energy. Depending on the proton and/or the neutron number, these deformations can occur either gradually or suddenly and manifest themselves through many observables. In this work, the focus will be only on sudden deformations due to their implication in the rapid change in structure and the shell evolution in general.

2.2.1. Observation of nuclear deformation

Like the magic numbers, the sudden deformations appear as discontinuities in some observables such as the two neutron separation energy. An example is shown in Figure 2.3 for the strong deformation in rare earth region. In Figure 2.4, the S_{2n} values in another deformation region at $N = 60$ and $A \approx 100$ are shown with another observable, the charge radii where also the sudden change of shape is seen from a the sudden jump of this observable for Rb to Zr isotopes.

The deformation does not appear only in the ground state but can be also seen from the excited states. Being deformed, the excited nucleus starts to rotate since it is not isotropic. It has a specific dexcitation via γ-ray depending on the type of the deformation or the so-called rotational band shown in Figure 2.5.

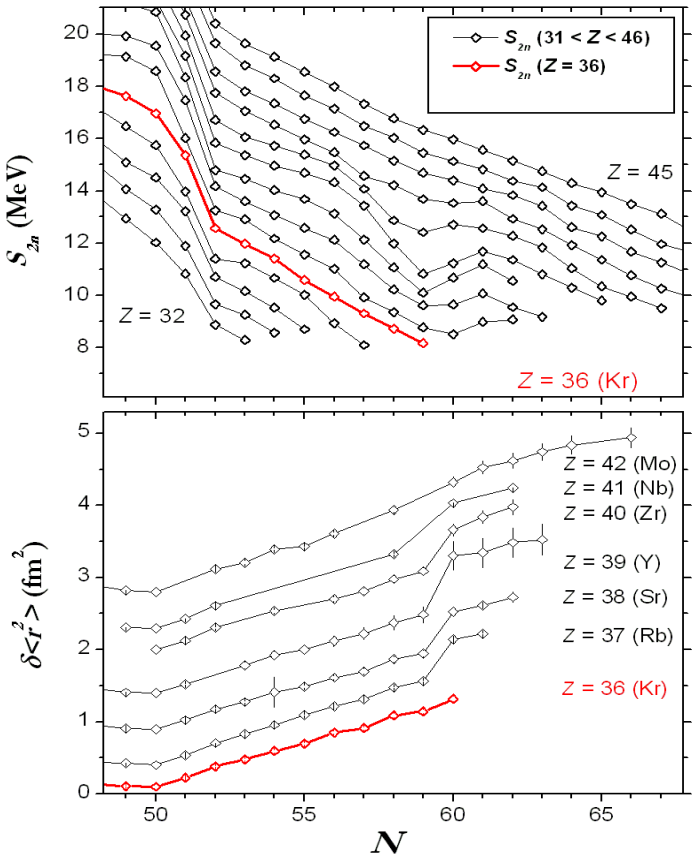

Figure 2.4.: S_{2n} values and charge radii in the $A \approx 100$ region plotted with the neutron number.

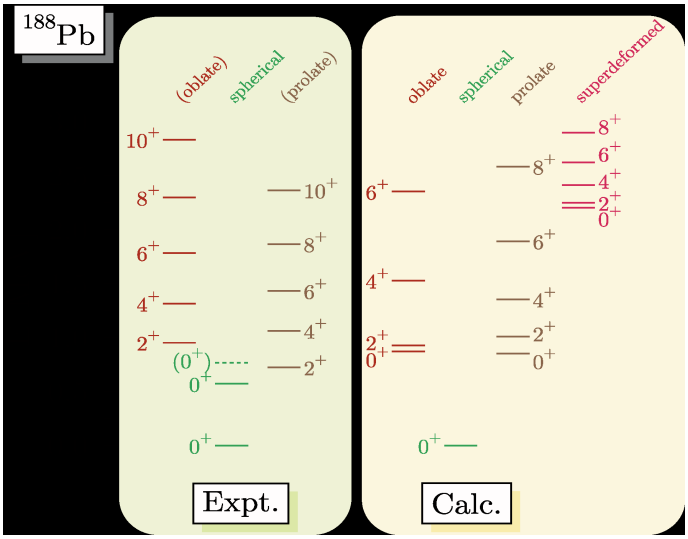

Figure 2.5.: Coexistence of different shapes in ^{188}Pb and the specific rotational bands for each kind of deformation (right: calculated spectra, left: experimental spectra).

2.2.2. Description of the nuclear deformation

The nuclear shape deformations are the result of the collective behavior of the nucleons inside the nucleus. Hence, they are well described by collective models or macroscopic and micro-macro models. However, these models ignore or neglect some important microscopic effects which are usually responsible of the shape that the nucleus takes. The Interaction Boson Model (IBM) is one of the models where the sudden changes in shape are nicely described. This model was proposed by Iachello and Arima [IA87] to reconcile the two most successful and complementary models used to describe the nuclei: the nuclear shell model and the collective model. This model is based on dynamical symmetries or the symmetry of the interactions which leads to a Hamiltonian invariant under a symmetry group. Thus, the Hamiltonian can be expressed in terms of invariant operators of the symmetry algebra (or the Casimir operators from group theory). The IBM describes collective modes in atomic nuclei at low energies, in terms of a finite number N of mutually interacting bosons, with N equals half the number of valence nucleons (particles or holes). Note that in the IBM-1 no distinction is made between neutron and proton bosons. When $N \to \infty$, the ground state is a boson condensate that can exhibit shape phase transitions between spherical, deformed prolate and deformed oblate forms when the interaction strengths are varied. The shape phase transitions, contrary to classical phase transitions, are not caused by pressure or temperature changes or by other external forces, but they are governed by the occupancy of single particle orbitals by protons and neutrons.

Thus, in the framework of this model the sudden deformation is seen as a quantum (shape) phase transition (QPT). In Figure 2.6 are shown the two orders of the phase transition expected for the two neutron separation energies. The value $\frac{\partial E}{\partial g}$ in the IBM is similar to the $S_{2n}(N)$ and parameter g or the so-called *control parameter* is similar to the neutron number N.

The evidence of the first order transition in the rare earth is shown in Figure 2.7 where the $S_{2n}(N)$ increases with N. The flattening at $N \sim 90$, for example, was shown to be a spherical-deformation transition due to the lowering of the proton orbit $h_{11/2}$ because of the neutron-proton interaction when neutrons start occupying the highly overlapping $h_{9/2}$ orbital [Cas+81].

The phase transition can also appear in other observables: the ratio between second (4^+) and first (2^+) exited states $R_{4/2}$, the transition probability from the first excited state (2^+) to the ground state (0^+) in even-even nuclei $B(E2)$ and also charge radii (see [Cas09]).

Looking to the deformation of the nucleus from this shape/phase transition perspective and with the help of the single particle orbitals one can answer two essential questions: how is the nucleus deformed?(the collective view) and why is it deformed?(single particle view).

In this work, the deformations in two different regions will be addressed in the term of quantum shape/phase transition. The first region is the famous $A \approx 100$ region which was extensively studied, here the results of the mass measurements of the Kr isotopes will be presented as well as their impact on the behavior of quantum shape/phase transition

even farther from stability.

The second region is also another famous region around $^{68}_{28}Ni_{40}$, where the question of the magicity of $N = 40$ will be studied. In this region the results of the mass measurements of the neutron-rich manganese isotopes far from stability will be shown as well as the role of collectivity in $N = 40$ magicity and its link to the quantum shape/phase transition.

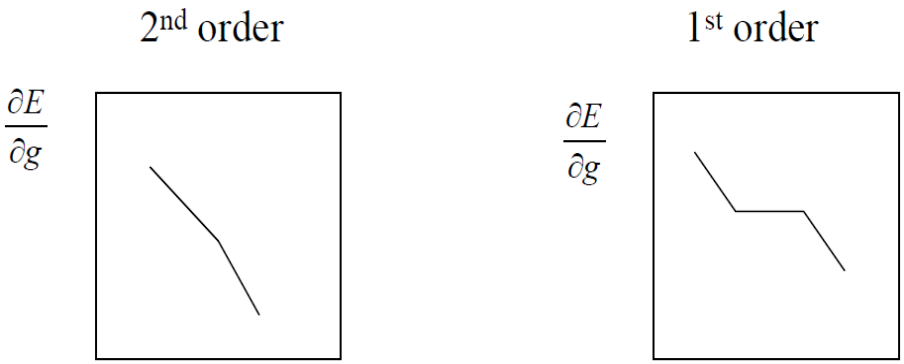

Figure 2.6.: Expected behavior of the $S_{2n}(N)$ values at phase transition in the IBM with $\frac{\partial E}{\partial g} \propto S_{2n}(N)$ and $g \propto N$.

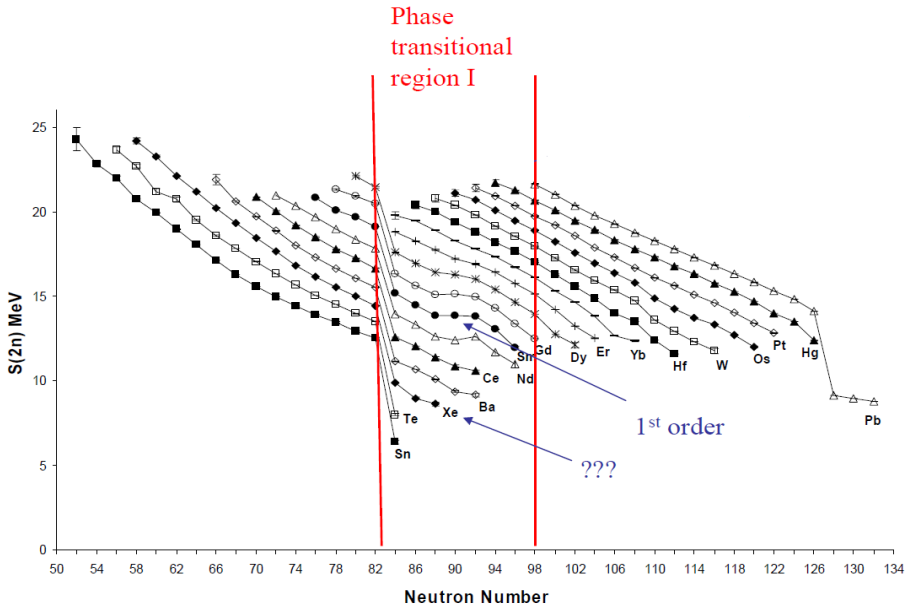

Figure 2.7.: The two neutron separation energy plotted with the neutron number. Here is shown the phase transitional region in the rare earth nuclei. Only $S_{2n}(N)$ values of the even-even nuclei are plotted since the IBM calculations are limited to even-even nuclei.

2.3. Exotic nuclei production

Radioactive Ion Beam (RIB) facilities played an important role in pushing the frontiers of our knowledge in nuclear physics and many other fields. The RIB facilities can be classified in two big families depending on the production techniques: the ISOL facilities and the 'In-flight' facilities. In the following the two kinds of facilities will be described. A detailed description of the ISOLDE facility, used to provide the nuclei studied in this work, will be given.

2.3.1. The Isotope Separator On Line technique

The ISOL-method requires a high-intensity primary beam of light particles from an accelerator (or a reactor), and a thick hot target, from which the exotic nuclei formed have to diffuse into an ion source, for ionization and extraction (Figure 2.8). In general, this method results in the formation of a whole host of nuclei, stable and non-stable, it is essential to use mass separators to select specific ions of interest. Since very high intensities of driver beams of high-energy protons (or reactor neutrons) are available, exotic nuclei with extremely low production cross sections can still be obtained in observable numbers. However, some isotopes having very short half-lives cannot survive in this 'time-consuming' thermal diffusion, characteristic of the ISOL-technique. Thus, the dependence on the chemical properties of the elements produced makes the extraction of some elements from the target very challenging. However, the beams of radioactive ions resulting from this technique have excellent optical properties, since these depend on thermal spread, and such high-quality beams are excellent for mass and isobar selection in mass spectrometers and collected or trapped beams.

Many facilities now exist for the production of exotic nuclei using the ISOL-technique: ISOLDE at CERN (Switzerland), ISAC at TRIUMF (Canada) and others, reviewed in [Lin04], IGISOL in Jyväskylä (Finland)[1].

2.3.2. In-flight technique

This method uses fragmentation of intense heavy-ion beams, in a thin target, in which the forward momentum of the primary beam fragments is exploited for mass separation or further reactions. These beams do not depend on the chemical properties (the release time for example) and very short-lived nuclei are produced. But as a result of the interaction in the target, they do not have good optical qualities, and need high-performance mass separators with high acceptance.

More recent then the ISOL facilities but with a great success, in-flight facilities were built around the world in the last 30 years such as GANIL in Caen (France), GSI Darmstadt (Germany), MSU in Michigan (USA) and RIKEN in Tokyo (Japan) (see [MS98]).

[1] IGISOL does not use thermal diffusion to extract radioactive species from the target which allows the production to refractory elements–not possible for other ISOL-facilities.

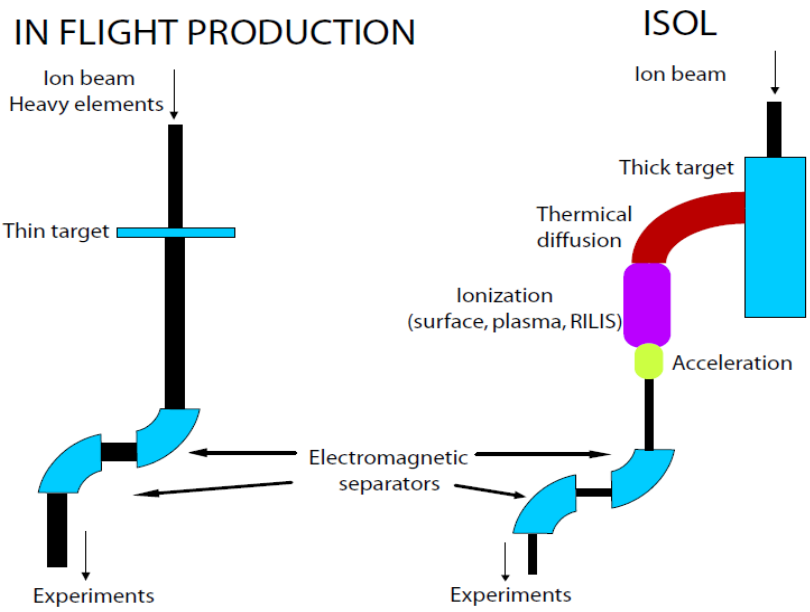

Figure 2.8.: The two main methods for the exotic beam production: (left) the in-flight technique and (right) the ISOL-technique.

2.3.3. ISOLDE Facility

ISOLDE, placed at the European Organization for Nuclear Research (CERN), is the mother of the ISOL-facilities and has been in use since the 70s [Kug00]. The primary beam used to bombard the thick target is a proton beam delivered from a linear accelerator (LINAC) and a Proton-Synchrotron-Booster (PSB) with an energy of 1-1.4 GeV. Proton pulses can reach up to 3×10^{13} protons per pulse (every 1.2 s) which corresponds to an average beam current of $\sim 2\mu$A. The radioactive nuclides are produced through fragmentation, spallation, and fission reactions within the target. Depending on the desired radioactive species, different target materials, such as calcium oxide or uranium carbide, are used. The reaction products evaporate and diffuse out of the target to an ion source. At ISOLDE three different types of ion sources can be used depending also on the desired species: Surface ionization, plasma ionization or resonant laser ionization. The choice is based on the physical and chemical properties of the different species to efficiently ionize the desired nuclide. As mentioned above, in the ISOL-technique all elements can be produced but not all can be delivered, for example the refractory elements due to their long release time.

When extracted from the ion source, which is nominally on a potential of 60 kV, the ions are usually singly-charged. They are then accelerated towards ground potential and transported to either the magnet of the General Purpose Separator (GPS) or the two magnets of the High Resolution Separator (HRS) with a resolving power of $m/\delta m \approx$ 1000 and 6000, respectively [Kug00]. After passing the magnet separator for the mass selection, the ion beam is then distributed to various experiments in the ISOLDE-hall via an electrostatic beam-line system (see Figure 2.9).

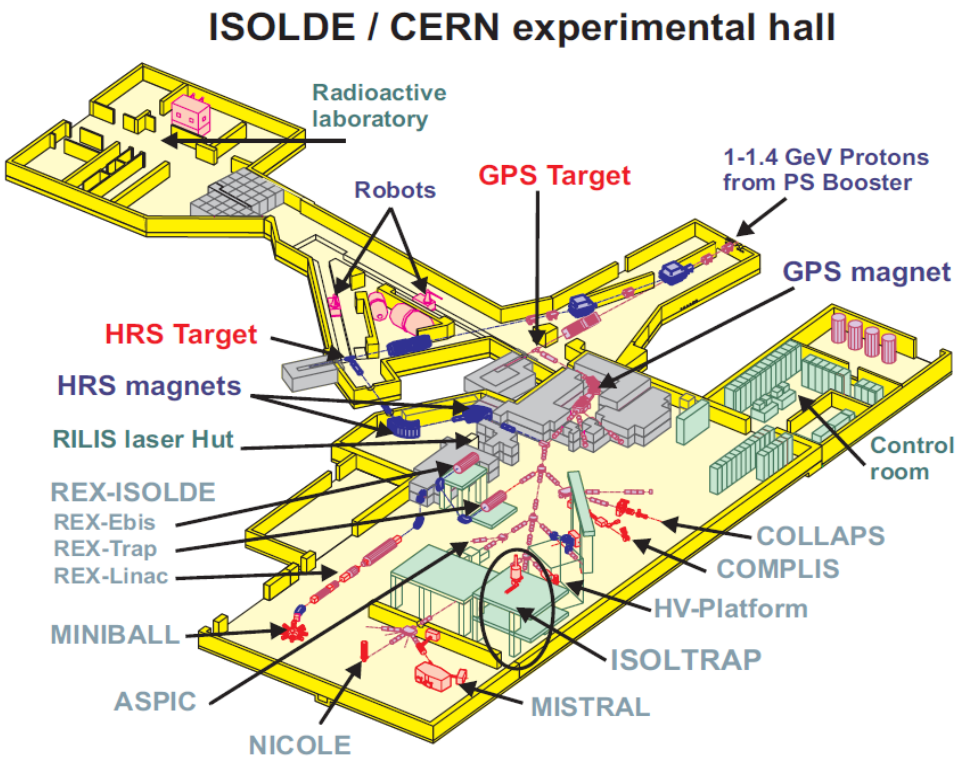

Figure 2.9.: Scheme of the ISOLDE facility at CERN in Geneva (Switzerland).

2.4. Mass measurement techniques

In the mass measurement techniques, two kinds can be distinguished: direct and indirect measurements, referring to inertial or energy measurements. These techniques are conditioned by the Radioactive Ion Beam production techniques. ISOL-facilities allow the use of high-precision methods, while in-flight facilities allow going father from stability (but with larger uncertainties).

"Indirect" mass measurement Masses can be deduced from the product of a nuclear reaction, for example the reaction $a(b,c)d$, by measuring the total reaction energy or Q value. The conservation of the total energy Q gives a relation between all masses involved in this reaction:

$$Q = M_a + M_b - M_c - M_d \tag{2.4}$$

The unknown mass can be determined from the measurement of Q if the three others are known.

Another kind of indirect mass measurement is from radioactive decay such as β-decay or electron capture. The measurement of the decay energy can provide relatively accurate mass differences between parent and daughter nuclides. These differences must be linked to known masses which can be sometimes far away, inducing cumulative errors.

"Direct" mass measurement The mass could be measured more directly from the ion time-of-flight needed to cover a certain distance or from cyclotron frequency.

An example of the time-of-flight method is the Experimental Storage Ring (ESR) at GSI where the mass can be deduced from measurements of the time-of-flight (or revolutions) of ions in storage rings [Lit+05]. This kind of installation is usually placed in the in-flight facilities: HIRFL-CSR Lanzhou (China) [Wan+09; Xu+09]. With this technique, one can reach a precision of 10^{-6} and can measure very short-lived nuclides ($\approx 1\mu s$). In [LPT03] is summarized all literature concerning this kind of technique.

The other direct mass measurement technique is based on the cyclotron frequency determination. Basically the charged particles (ions) are confined in electric or/and magnetic fields. From the conservation law of Lorentz forces, the mass can be related to the measured frequency $\nu_c = qB/2\pi m$ (q charge, B magnetic field and m the mass). Penning traps, based on this technique, have become the tool of choice for high-precision mass measurements since they can reach a relative precision of 10^{-11} for stable nuclei and 10^{-8} for radioactive ones. Many Penning traps, dedicated to mass measurement of radioactive nuclei, exist and are very active: ISOLTRAP at ISOLDE/CERN [Muk+08], SHIPTRAP at GSI [Rah+06], LEBIT at MSU [Rin+06], TITAN at TRIUMF [Del+06], CPT at Argonne [Sav+01], JYFLTRAP at Jyväskylä [Jok+06]. Since the measurement requires storing the ions for a given period, this technique is usually limited by the half-lives of the radioactive nuclides. However, due to the technical developments during the last few years, Penning traps allowed to go for shorter half-lives without decreasing the precision ($\approx 10 - 100ms$). In Figure 2.10 is shown the status of mass measurements in 2004 and 2008 using different techniques. One can see that Penning traps played an important role in the determination of new masses with high precision.

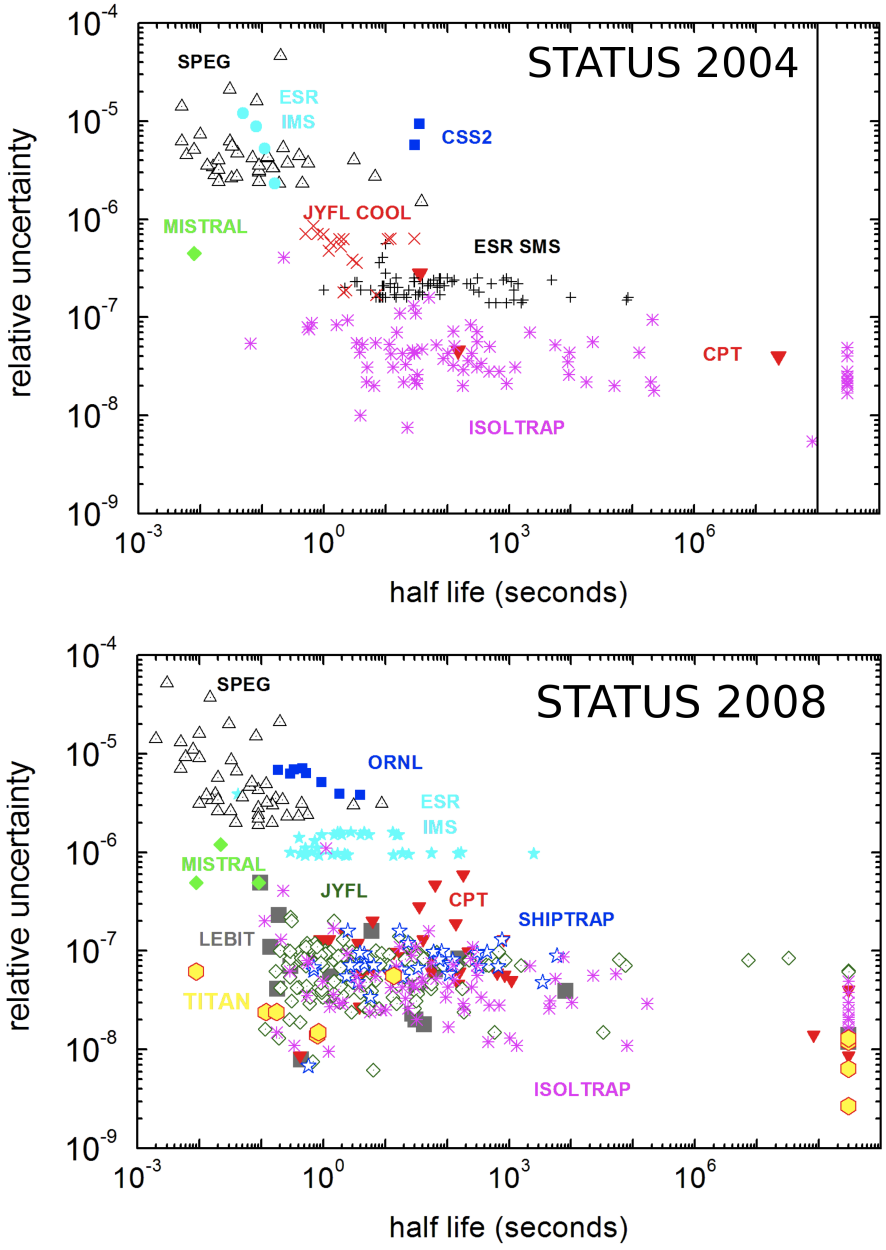

Figure 2.10.: The relative mass precision as a function of the half-life. The status in 2004 and 2008 of the mass measurements of radioactive nuclides is shown with the contribution of different techniques: TOF-techniques (ESR-IMS, ESR-SMS, SPEG) and Cyclotron-frequency determination techniques (MISTRAL, ISOLTRAP, CPT, SHIPTRAP, LEBIT, TITAN, JYFLTRAP) [Lun08].

3. The Penning trap

In this chapter, the trapping principle using the Penning traps is reviewed. The use of this technique for the high precision mass measurement purpose of the radioactive nuclides will be developed in the next chapter as well as the data analysis procedure.

The Penning trap was invented by H.G. Dehmelt (for which he received the Nobel Prize in Physics in 1989). It is based on a superposition of a strong homogeneous magnetic field to confine the ions in the radial direction and a weak quadrupolar electrostatic field to store them in the axial direction or the trap axis $\vec{e_z}$. The Penning traps can have several geometries according to their purpose. ISOLTRAP has two kinds of Penning traps, cylindrical and hyperbolic illustrated in Figure 3.1. The cylindrical one is used for the beam preparation and purification since it has a large beam acceptance (see section 4.1). The hyperbolic one is used for high precision mass measurement (see section 4.2).

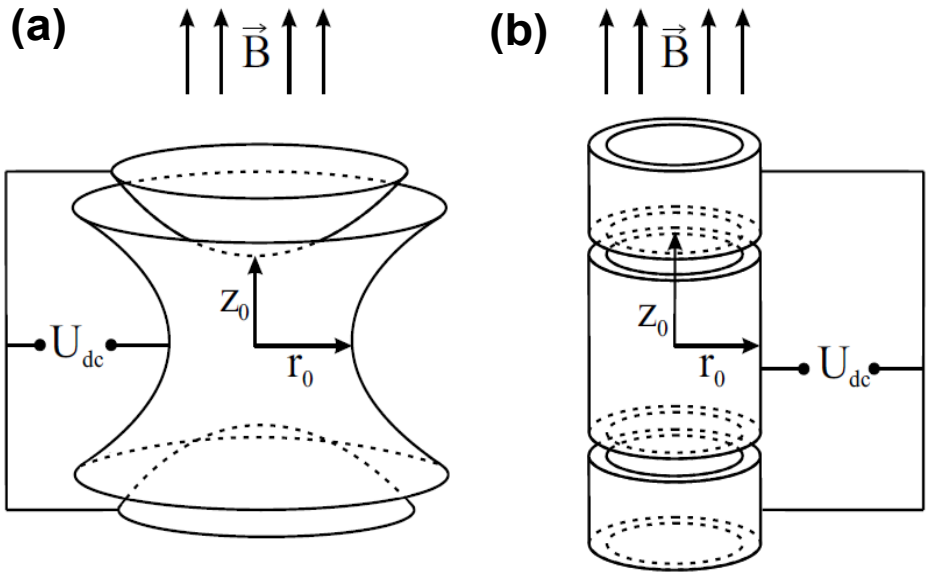

Figure 3.1.: Different geometries of the Penning trap; (a) hyperbolic Penning trap, (b) cylindrical Penning trap

3.1. Ion storage

To confine particles in 3D space, a potential minimum in each spatial direction is required. The confinement in electric fields would imply that the mean value of the electric field

with respect to time vanishes and the potential of the electrostatic field $\vec{E}(\vec{r}) \neq \vec{E}(\vec{r}, t)$ has to fulfill the Laplace equation $\Delta\phi(\vec{r}) = 0$. With a pure electrostatic potential a full three-dimensional confinement is impossible. In Penning traps, the radial confinement is assured by a strong homogeneous magnetic field.

The interaction of a particle with mass m and charge q with an electromagnetic field is described by the Lorentz force law:

$$\vec{F} = m\vec{a} = q(\vec{E} + \vec{v} \times \vec{B}) \tag{3.1}$$

with $\vec{B} = B.\vec{e_z}$ and $\vec{E} = -\vec{\nabla}.\phi$ created by the electrical field potential ϕ in the Penning trap which consists in the simplest way of two end-cap electrodes and one ring electrode. In the ideal case these electrodes are infinite hyperboloids of revolution (see Figure 3.1 (a)), which create a perfect axially symmetric electric quadrupole potential

$$\phi(\rho, z) = \frac{V_0}{4D^2}(2z^2 - r^2) \tag{3.2}$$

V_0 is the voltage difference between the ring electrode and the endcap during storage time and D is a geometrical parameter characterizing the Penning trap $D = \sqrt{\frac{1}{2}(z_0^2 + \frac{r_0^2}{2})}$ (z_0 and r_0 are the distances from the trap center to the endcaps and the ring electrode, see Figure 3.1).

From Equation 3.2, Equation 3.1 can be written as the following:

$$\begin{pmatrix} \ddot{x} \\ \ddot{y} \\ \ddot{z} \end{pmatrix} = \frac{qV_0}{2mD^2} \begin{pmatrix} x \\ y \\ -2z \end{pmatrix} + \frac{qB}{m} \begin{pmatrix} \dot{y} \\ -\dot{y} \\ 0 \end{pmatrix} \tag{3.3}$$

If the two frequencies $\omega_c = \frac{qB}{m}$ and $\omega_z = \sqrt{\frac{qV_0}{mD^2}}$ are introduced, the equations of motion become:

$$\ddot{x} = \omega_c\dot{y} + \frac{1}{2}\omega_z^2 x \tag{3.4}$$

$$\ddot{y} = -\omega_c\dot{x} + \frac{1}{2}\omega_z^2 y \tag{3.5}$$

$$\ddot{z} = -\omega_z z \tag{3.6}$$

ω_c being the cyclotron angular frequency of a charged particle in the magnetic field and ω_z its axial angular frequency. The axial motion is then decoupled from the magnetic field and the solution of the last equation is an harmonic oscillator:

$$z(t) = A_z(0)\cos(\omega_z.t + \theta(0)) \tag{3.7}$$

where the amplitude $A_z(0)$ and the phase $\theta(0)$ are determined by the initial conditions. So the axial motion depends only on the electric field.

To solve the equation of motion in the radial plane or in the xy-plane it is more

convenient to introduce the complex variable $u = x + iy$. The two first equations of motion Equation 3.4 and Equation 3.5 are reduced to one equation:

$$\ddot{u} + i\omega_c\dot{u} - \frac{1}{2}\omega_z^2 u = 0 \tag{3.8}$$

As a complex number u can be written $u(t) = u(0).e^{-i\omega t}$ and the Equation 3.8 becomes:

$$\omega^2 - \omega_c\omega + \frac{\omega_z^2}{2} = 0 \tag{3.9}$$

The radial eigenfrequencies are then:

$$\omega_\pm = \frac{1}{2}\left(\omega_c \pm \sqrt{\omega_c^2 - 2\omega_z^2}\right) \tag{3.10}$$

with the condition for real values and thus the trapping condition $\omega_c^2 - 2\omega_z^2 \geq 0$. The particle oscillates then with three eigenmotions which fulfill the following relations:

$$\omega_c = \omega_+ + \omega_- \tag{3.11}$$
$$\omega_c^2 = \omega_+^2 + \omega_-^2 + \omega_z^2 \tag{3.12}$$
$$\omega_z^2 = 2\omega_+\omega_- \tag{3.13}$$

The axial frequency ω_z is very small in comparison with the radial one ω_c (for $^{85}Rb^+$ in an hyperbolic Penning trap with $D = 10.2$ mm, $V_0 = 10$ V and $B = 6$ T: $\omega_z \approx 33\times10^4$ s^{-1} $<<$ $\omega_c \approx 680 \times 10^4$ s^{-1}). So the Taylor expansion of Equation 3.10 can be done and the two radial motions can be written:

$$\omega_+ = \omega_c - \frac{\omega_z^2}{2\omega_c} + O(\omega_z^4) \approx \frac{qB}{m} - \frac{V_0}{2D^2B} \tag{3.14}$$
$$\omega_- = \frac{\omega_z^2}{2\omega_c} + O(\omega_z^4) \approx \frac{V_0}{2D^2B} \tag{3.15}$$

Thus, in first order the so-called *magnetron* angular frequency ω_- is mass independent. The ω_+ is called the *reduced* or *modified cyclotron* frequency, because it is due to the effect of the crossed electric and magnetic fields that reduces the cyclotron angular frequency ω_c. In Figure 3.2, the three motions of the charged particle in a Penning trap are shown (note that this figure is not to scale).

3.2. Ion manipulation and excitation schemes

Once the ion confined and oscillating inside the Penning trap, one can use these oscillations to control the ion motion for different purposes. In this work two main objectives are important: the high precision mass measurement (ISOLTRAP's precision Penning trap) and the beam preparation (ISOLTRAP's preparation Penning trap).

To influence the ion motion inside the trap it is sufficient to apply an external radiofrequency field which leads to increase the energy of the system by increasing the

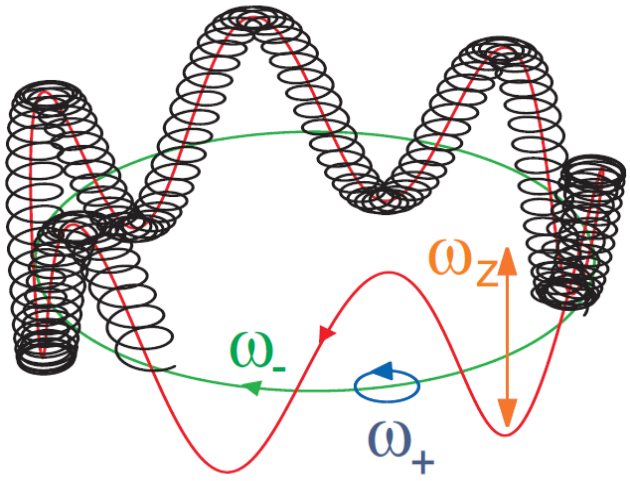

Figure 3.2.: Trajectory of a charged particle in a Penning trap (black) as a superposition of the magnetron motion with frequency ω_- (green), the cyclotron motion (blue) with modified frequency ω_+, and the axial motion ω_z (orange). The superposition of magnetron and axial motion is shown (red). This figure is a qualitative picture of the ion motion as the relative frequencies and amplitudes are not to scale.

quantum numbers:

$$E = \hbar\omega_+(n_+ + \frac{1}{2}) + \hbar\omega_z(n_z + \frac{1}{2}) - \hbar\omega_-(n_- + \frac{1}{2}) \tag{3.16}$$

From this equation, the magnetron motion contributes negatively to the total energy. This feature is very important for the ion manipulation. Applying a dipole electric field results in ion energy loss. The additional azimuthal quadrupole driving field with a frequency that equals to the combination of the frequencies of the fundamental motion modes (sum or difference), leads to a periodic conversion of the participating modes into each other.

In the following section, these two kinds of excitations (dipole and quadrupole) will be described. More details on the ion motion in a Penning trap in a classic and quantum mechanical frame work are given in [Kre99; Kre92].

In order to apply an external field to influence the ion motions inside the Penning trap, the ring electrode of the trap is split into four segments. For a dipolar field only two segment are needed while for the quadrupole field four segments are needed (see section below).

3.2.1. Dipolar excitation

An electrical dipolar field is applied to two segments of the ring electrodes, as is shown in Figure 3.3 (left).The electrical field due to this dipolar field:

$$\vec{E}_D = -A_D \cos(\omega_D t + \varphi_D).(d_x\vec{e}_x + d_y\vec{e}_y) \tag{3.17}$$

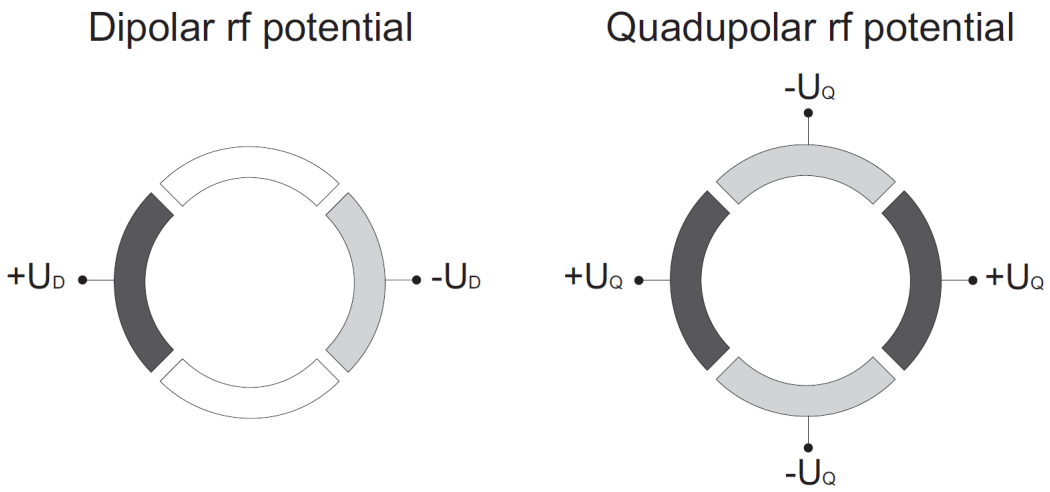

Figure 3.3.: Radial segmented ring electrode (top view) of a Penning trap to apply an electromagnetic radiofrequency field. (left) Dipolar radiofrequency field between two opposite ring segments in phase with the ion motion. (right) A quadrupolar field can be generated by applying a radiofrequency field between each opposite pairs of the four-fold segmented ring electrode.

where the amplitude $A_D \propto U_D/\rho_0$. The important parameters for the ion manipulation are the amplitude and the phase difference between the radiofrequency driving field and the ion motion $\Delta\varphi_\pm = \varphi_D - \varphi_\pm$. The latter has a strong effect on the magnetron radius ρ_- and the cyclotron radius ρ_+. For the isolation of specific ions from an ensemble of several species, the unwanted ions are radially ejected by an excitation field covering the appropriate frequency ω_+. Applying the appropriate magnetron frequency ω_- leads to change simultaneously the magnetron radius of all trapped ions, since this motion is mass independent.

3.2.2. Quadrupolar excitation

The most direct approach for mass spectrometry is the measurement of the sum frequency $\nu_c = \nu_+ + \nu_-$ which corresponds to a coupling of the modified cyclotron and magnetron oscillation. As it will be explained in section 3.3 this is also important in buffer gas cooling in Penning traps. The coupling of the two radial motions can be achieved by an azimuthal quadrupolar radiofrequency (rf) field with the frequency ω_{rf} applied with 180° phase shifts on sets of ring-electrode segments perpendicular to each other (see Figure 3.3).

$$\vec{E_x} = C_q.\cos(\omega_{rf}.t + \varphi_{rf}).y\vec{e_x} \tag{3.18}$$

$$\vec{E_y} = C_q.\cos(\omega_{rf}.t + \varphi_{rf}).x\vec{e_y} \tag{3.19}$$

where C_q is a constant depending on the quadrupolar amplitude U_Q and the trap geometry parameters. If the applied frequency reaches the cyclotron frequency, in resonance $\omega_{rf} = \omega_c$, a full periodic conversion between the two motional radii ρ_+ and ρ_- is obtained (the magnetron motion has vanished while the amplitude of the

cyclotron motion is equal to the initial magnetron motion amplitude). For a non-resonant excitation ($\omega_{rf} \neq \omega_c$) the conversion is not complete.

It is important at this stage to say few words about the radial kinetic energy since it is a crucial feature for the ion detection, see section 4.2. The radial kinetic energy is proportional to the frequencies of the trapped ion:

$$E_r = \omega_+^2 \rho_+^2(t) + \omega_-^2 \rho_-^2(t) \approx \omega_+^2 \rho_+^2(0) \tag{3.20}$$

In resonance case, since $\omega_+ \gg \omega_-$, the coupling of the magnetron and cyclotron modes increases the radial kinetic energy as well as the associated magnetic moment. Out of resonance, the conversion is not complete, so the radial energy is lower. The importance of the radial energy for the ion detection will be detailed in section 4.2.

3.3. Damping the ion motion in the Penning trap

An ideal Penning trap does not exist, unless it has to have infinite electrodes. Therefore, Penning traps used for experiments have electric and magnetic imperfections. To avoid these imperfections, the ions should be trapped in a smaller volume. To achieve that, the motional amplitude should be decreased by cooling techniques. The mass resolving power is directly proportional to the relative velocity spread. Ion cooling is then very important for high-accuracy mass spectrometry with stored ions. The other purpose of the ion cooling is the beam transport of a cooled ion bunch which is much more efficient due to the reduction of the transverse and longitudinal emittance. The most common cooling techniques are: buffer-gas cooling, resistive cooling, electron cooling and laser cooling. In this section only the buffer-gas cooling technique will be developed since it is the one used in this work.

The presence of a buffer-gas in the Penning trap leads to the loss of the kinetic energy by collision with the gas atoms. The damping force depends then on the ions velocity and the viscous drag force can be written:

$$\vec{F} = -2m\gamma\vec{v} \tag{3.21}$$

where m and $\vec{v}$ are respectively the mass and the velocity of the trapped ion. The damping coefficient γ describes the effects of the buffer-gas with respect to the ion mobility. Usually, noble gases are used as a buffer gas due to their high ionization potential which leads to minimize the charge exchange ion loss in the trap. The damping force decreases the cyclotron motion and increases the magnetron motion (due to negative potential, see Equation 3.16). To avoid loosing the trapped ion by increasing its magnetron radius, coupling of the two motions is performed via the quadrupolar field. Since $\omega_+ \gg \omega_-$, the reduced motion is dumped much faster than the magnetron motion. The coupling by the quadrupolar driving field with appropriate excitation amplitude and adjusted gas pressure leads to a reduction of all amplitudes of the ion motion. If the excitation with the quadrupolar frequency ω_{rf} is in resonance with the cyclotron frequency $\omega_c = qB/m$ of the ion of interest, a mass selective centering of one specific ion species will occur [Sav+91].

This method is used in the ISOLTRAP preparation Penning trap in the purpose of

delivering a cooled and purified beam for high-precision mass measurement in the second Penning trap (see section 4.2). It can also be used as a mass measurement technique. For more detail see section 4.6.

4. Isoltrap experimental setup

The measurements presented in this work were performed using the mass spectrometer ISOLTRAP [Muk+08] installed at the isotope separator ISOLDE at CERN [Kug00]. ISOLTRAP consists of three main parts : a Paul trap or Radio-Frequency Quadrupole RFQ and two Penning traps (cylindrical and hyperbolic). The RFQ and the first Penning trap are used to cool and prepare the beam while the second Penning trap is used for high precision mass measurements. A schematic view of the setup is shown in Figure 4.1 In this section the adventure of the ions from the RFQ to the precision trap (their cooling and preparation to the mass measurement) is described. Also, the data analysis procedure is detailed; from the raw data to the extraction of the atomic masses.

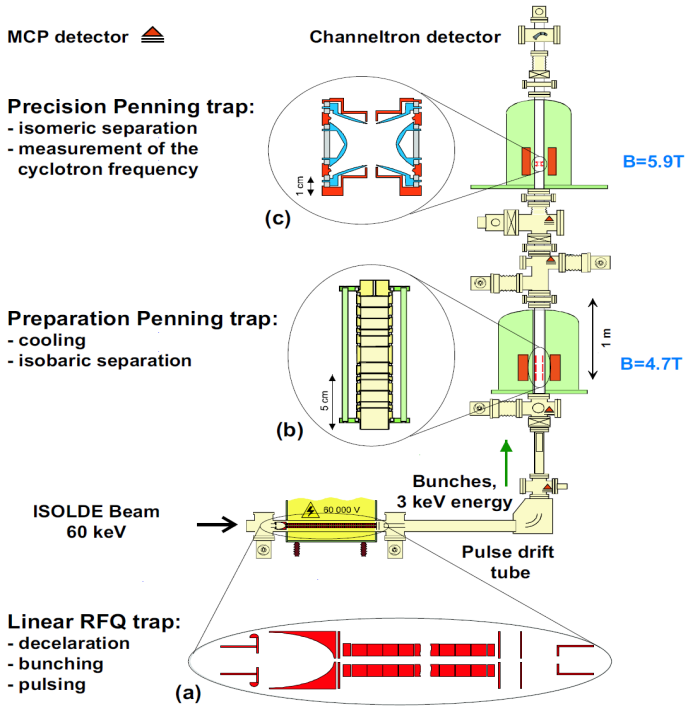

Figure 4.1.: ISOLTRAP experimental setup. The ISOLDE beam is stopped and cooled in the RFQ buncher (a), transported to the cylindrical preparation Penning trap for isobaric purification and further cooling (b), then to the hyperbolic precision Penning trap to perform the mass measurement (c).

4.1. Beam preparation

To trap the ions produced at ISOLDE the beam should be decelerated from the nominal 60 kV to few volt, which leads to increased emittance. So the beam should be cooled before the mass measurement. Two devices serve this purpose: an RFQ Buncher and a gas-filled Penning trap (called the preparation trap). As explained in section 2.3, the ISOLDE beam is usually accompanied by isobaric or/and molecular contaminations. Since mass measurements must be performed using only few trapped ions (to avoid ion-ion interaction), this beam must be first purified. Therefore, the gas-filled Penning trap is used as an isobaric separator with high resolving power ($m/\Delta m \sim 10^5$).

4.1.1. The RFQ cooler-buncher

The RFQ buncher is a linear gas-filled Paul trap which is composed of four longitudinally segmented rods in order to axially and radially store the ions [Her+01], as shown in Figure 4.2. When the ions arrive to the RFQ with an energy of 60 keV, they are decelerated and focused by the first egg-shaped electrode [Kel+01] and their kinetic energy decreases to a few hundred eV. They enter the RFQ where they are trapped radially by a radio-frequency field and axially by a potential applied to the longitudinally segmented rods. Because of the collisions with the buffer gas atoms, the ions lose kinetic energy. Therefore, the beam is cooled and its emittance is reduced. After an accumulation time of few milliseconds the last electrodes of the segmented rods are switched down in order to release the ion bunch so that it can be transported to the preparation trap. Two pulsed drift tubes are placed one behind the cooler-buncher and the second in front of the preparation trap. The former gives a kinetic energy of about 3 keV for the beam transport. The latter decreases this energy to few hundred eV in order to trap the ions in the preparation trap.

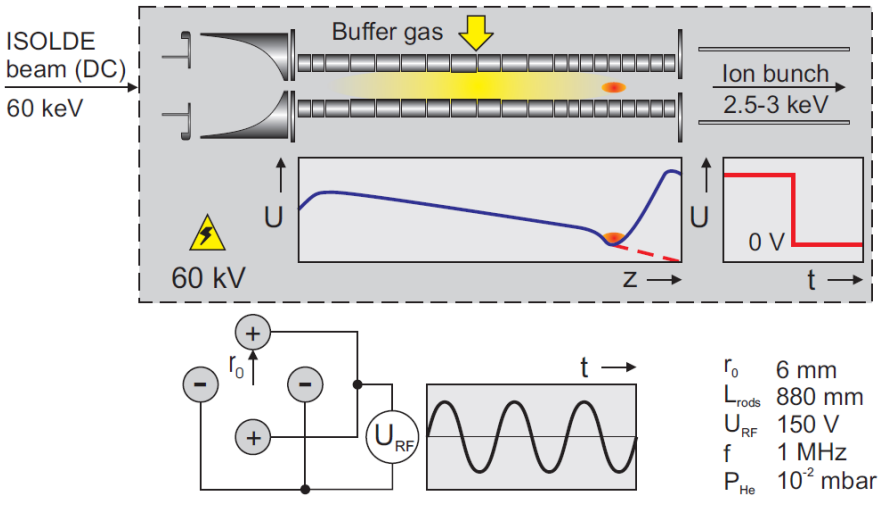

Figure 4.2.: The ISOLTRAP RFQ cooler-buncher

4.1.2. The preparation Penning trap

This gas-filled cylindrical Penning trap is placed in a strong magnetic field of 4.7 Tesla. It is used for isobaric mass separation and further cooling using the buffer-gas cooling technique [Sav+91]. This trap is considered as a nested trap since it has two parts: the harmonic part (the ring electrode) where the excitations can be applied for the isobaric separation and the outer part (the correction and end caps electrodes) where the ions are trapped, cooled and sometimes accumulated until they fall to the harmonic part and are trapped. The presence of the buffer gas is important for the cooling and the damping of the ion motion in the harmonic part (see section 3.3). The cooling with the buffer gas is also crucial for the ion-transfer to the precision Penning trap.

The ions coming from the RFQ buncher are captured and trapped axially by a potential applied by the several end caps as shown in Figure 4.3 on the left. When the ions are cooled and trapped in the harmonic part, the ion manipulation can start in order to perform isobaric separation. First, a dipolar magnetron excitation is applied, which increases the ion magnetron radius of all trapped species present in the beam, since to first order, the magnetron motion is mass independent (Equation 3.15). The amplitude of this excitation is chosen in such a way that after the dipolar excitation, none of the ions initially stored in the trap can be ejected (the magnetron radius is larger than the 3 mm aperture in the last endcap, shown in Figure 4.3). In order to eject only the ions of interest, they have to be centered to the trap axis using a quadrupolar excitation at the cyclotron frequency ν_c of the ion of interest (this frequency is mass dependent $\nu_c = qB/2\pi m$). This radio-frequency excitation converts the magnetron motion into cyclotron motion. Because of the buffer gas present in this trap, the cyclotron motion is damped and the ions are centered (see section 3.3). With sufficient duration, the excitation leads to an isobaric selection with a resolving power of up to $R \sim 10^5$. If the resolving power is not sufficient to suppress all contaminants, a dipolar excitation at the modified cyclotron frequency ν_+ of the contaminant can be applied for further purification.

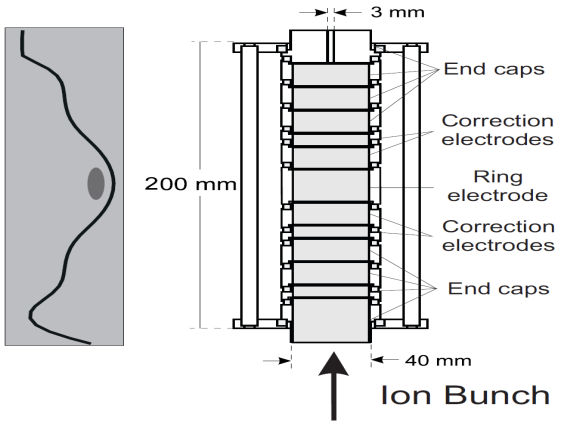

Figure 4.3.: Schematic view of the preparation Penning trap (right), and the axial potential (left). The ion bunch is shown trapped in the harmonic part of this potential.

4.2. The cyclotron-frequency determination

The high-precision mass measurement is based on the cyclotron frequency determination $\nu_c = qB/2\pi m$ measured in the precision trap which is a hyperbolic Penning trap placed in ultra-high vacuum and an homogeneous magnetic field of 5.9 Tesla. The purified ion bunch arrives in the precision trap with a very low energy spread and is stored just by applying a very low potential to the end cap electrode. The stored ions have initially almost no cyclotron radius and a very small magnetron radius. Some excitations have to be applied then for the cyclotron frequency determination. First the magnetron radius is increased by applying a dipolar excitation at ν_-. The magnetron radius is very small (about 0.7 mm) so that the ions probe less the imperfections of the trap. A larger magnetron radius is not needed here since this trap is not used for purification like in the preparation trap. However, this trap can be used for further cleaning by applying a dipolar excitation at the cyclotron frequency ν_+ of the contaminants which leads to an increase of their radius. These unwanted ions are ejected radially and hit the trap walls (so they are lost). This fine purification typically reaches a resolving power of 10^6.

Finally, a radio-frequency quadrupolar excitation is applied with the frequency ν_{rf}. Given the correct amplitude, if $\nu_{rf} = \nu_c$ (the resonant case) a full conversion from pure magnetron to cyclotron motion is achieved (see subsection 3.2.2) and the kinetic radial energy E_r (Equation 3.20) is maximum. In the off-resonance case, $\nu_{rf} \neq \nu_c$, the conversion is not complete and the radial kinetic energy then is lower.

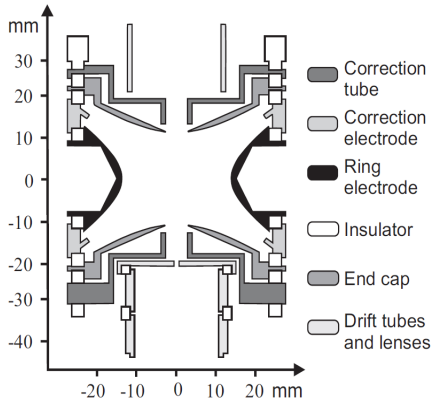

Figure 4.4.: The ISOLTRAP precision Penning trap.

After the excitation, the ions are extracted from the Penning trap (5.9 Tesla) and transported to the detector area (few mTesla) as illustrated in Figure 4.5. On their way to the detector, the ions therefore see a strong magnetic field gradient. They are accelerated due to this gradient force and thus their axial velocity increases:

$$\vec{F} = -\vec{\mu}.\vec{\nabla}\vec{B} = -\frac{E_r}{B}.\frac{\partial B}{\partial z}.\vec{e_z} \tag{4.1}$$

For the resonant case, the radial kinetic energy is maximal which leads to the highest axial velocity, thus the ions in resonance reach the detector faster than the ions off-

resonance. The cyclotron frequency determination is based then on the detection of the ions time of flight as a function of the radio-frequency excitation, which can be written [Kön+95]:

$$TOF(\nu_{rf}) = \int_0^{Z_{detector}} \sqrt{\frac{m}{2(E_0 - qV(z) - E_r(\nu_{rf})B(z)/B_0)}} dz \tag{4.2}$$

where E_0 is the initial axial energy of the ion, $V(z)$ the electric potential created by the drift electrodes (between the trap and the detector), $B(z)$ the strength of the magnetic field along the z-axis, and B_0 the magnetic field value in the trap region.

Figure 4.6 displays an example of a TOF resonance with the corresponding time-of-flight spectrum. It should be noted that on the left the frequency ν_{rf} is plotted with the *mean* time-of-flight while on the right is the time-of-flight spectrum. For each ν_{rf} value a bunch of ions is detected with small spread around a time-of-flight value (this spread is due to the ions energy spread while they are flying from the trap to the detector). So for each ν_{rf} value the ions have a *mean* time-of-flight, the vertical error bars include the statistical uncertainty and the ion energy spread. This point is important for the discussion of the comparison with the new mass measurement procedure (see section 4.6).

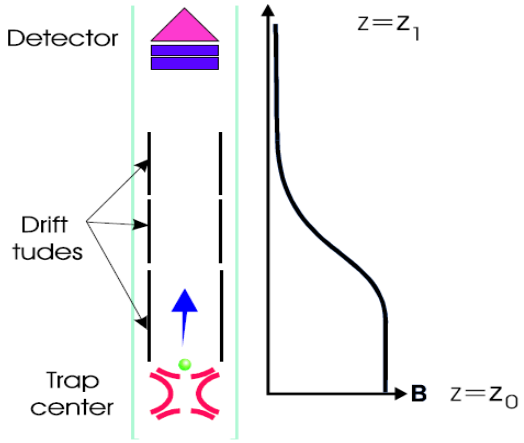

Figure 4.5.: Principle of the time-of-flight cyclotron resonance detection technique

4.3. Excitation time and resolving power

A long observation time is needed to reach a decent precision in order to probe nuclear structure information. Experimentally, this observation time is the duration of the different excitations (dipolar and/or quadrupolar), the *excitation time*. Thus, the mass precision depends strongly on the resolving power which can be written [Bol+96]:

$$R = \frac{m}{\Delta m} = \frac{\nu_c}{\Delta \nu_c} \approx \nu_c . T_{rf} \tag{4.3}$$

So, for the same excitation time the precision of the lighter ions (high frequency) is higher than heavier ones (low frequency). The excitation time is therefore an important

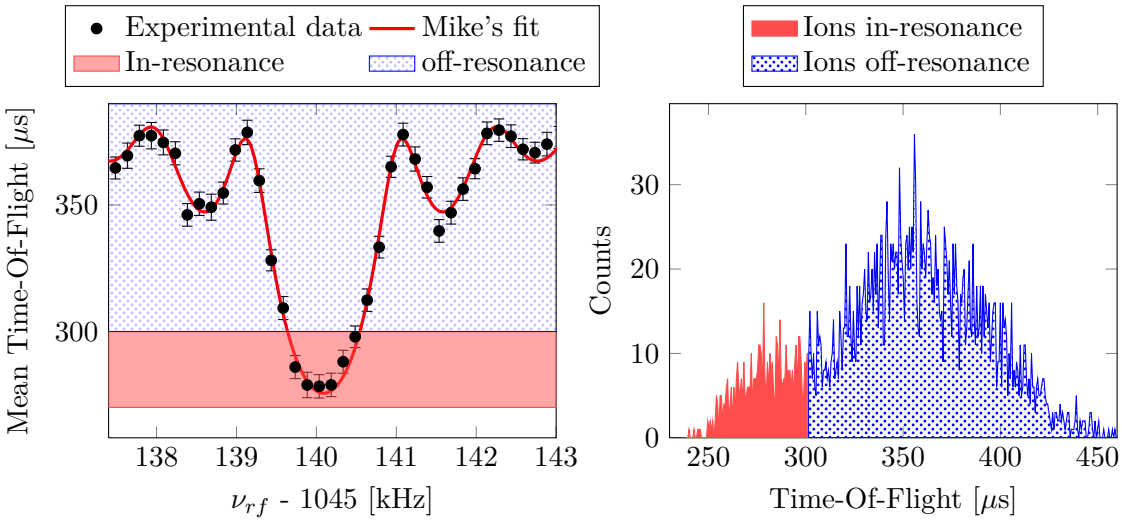

Figure 4.6.: (left): The typical Time-Of-Flight resonance behind the precision trap (here $^{87}Rb^{+}$ with $T_{rf} = 600ms$), the mean TOF is plotted versus the radio-frequency excitation ν_{rf}. The data are fitted with the so-called Mike fit [Kön+95][a] which will be described in subsection 4.5.1. (right): the corresponding integrated TOF spectrum shown with the ions in-resonance (faster) and the ions off-resonance (slower). The so-called in-resonance ions (shown in the pink area) have an excitation frequency ν_{rf} very close to ν_c, very few of them are really in-resonance $\nu_{rf} = \nu_c$ ($\sim$ 140 Hz). Here the *appellation* in/off-resonance is just to illustrate the relation between the TOF and the excitation frequency ν_{rf}.

[a] Named after Michael König, first author of [Kön+95].

parameter for the mass determination and its precision of short-lived nuclides and also for the isobaric separation or the purification process in the cylindrical preparation trap.

4.4. How much time do ions spend in the experimental setup?

For short-lived nuclides, the preparation and measurement time should be long enough compared to the half-lives $t_{1/2}$ since mass precision depends on the excitation time (Equation 4.3). Therefore, in on-line experiments with very short-lived nuclides, the compromise between precision and short time spent in the preparation and measurement must be found. Contaminated beams need some time for the purification. If the contaminated ions have a mass close to the ions of interest, the purification process has to be longer to increase the resolving power ($R \sim T_{rf}$). In Figure 4.7, two experimental cycles are shown (short and long) with different timing for each step. In the right side are shown in red different timings when very short-lived nuclei are measured. The cleaning for example (step 15) could be skipped and by then limiting the purification process in the precision trap. The ISOLTRAP record for the shortest-lived nuclide will be presented in this work: ^{66}Mn with $t_{1/2} \approx 64$ ms (see section 5.2).

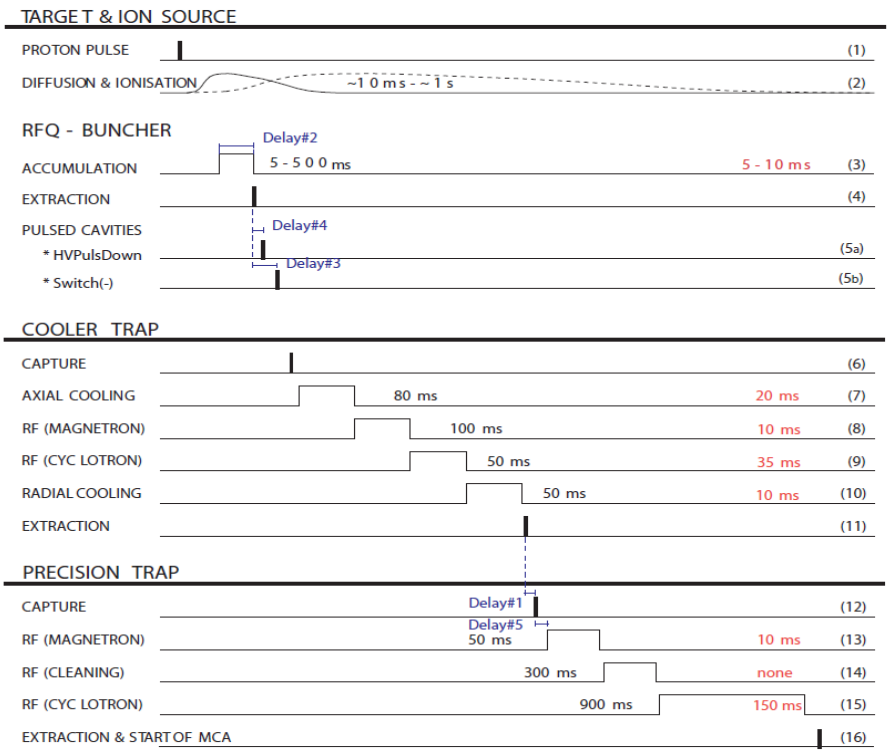

Figure 4.7.: Excitation scheme or the ISOLTRAP cycle. Numbers given are corresponding to the excitation time applied for long cycles (black), e.g. for stable $^{85}Rb^{+}$, and short cycles (red) used for very short lived nuclides (^{96}Kr for example).

4.5. From frequencies to masses

The ion counts and frequencies are the raw data provided by the measurements. In this section, the data analysis procedure will be described. The steps followed from the raw frequencies to the final masses and the estimation of their uncertainties will be detailed.

4.5.1. TOF resonance fit

The theoretically expected line shape for a TOF resonance is mainly determined by the Fourier transformation of the rectangular time excitation profile since the quadrupole excitation is applied at constant amplitude only during the interval T_{rf}. This function is similar to the absolute value of the $\mathrm{sinc}(x) = \sin(ax)/ax$ function. The width of such a signal, and therefore the resolving power, is Fourier limited by the duration of the quadrupolar excitation.

In order to fit the TOF resonances, a data analysis software[1] is used and the relevant parameters are used to fit the experimental data (see Table 4.1). An example of this fit (the Mike fit) is shown also in Figure 4.6.

[1] EVA software was developed for ISOLTRAP and is needed by Penning trap experiments using the TOF ion cyclotron resonance technique. This software is maintained by S. Schwarz.

Parameter	Typical values for $^{66}Mn^{+}$	Description
ν_c	1377072.2(7) Hz	Cyclotron resonance frequency
ρ_-	0.37(5)	Magnetron radius before the quadrupolar excitation
ρ_+	0	Cyclotron radius before the quadrupolar excitation
Conv	0.99(15)	Number of conversions of the two radial motions
A_{Damp}	0.5 s^{-1}	Damping due to collision with rest gas
T_{rf}	50 ms	Excitation time
TofOff	106(5) μs	Time-of-flight offset

Table 4.1.: Parameters used to fit the theoretical line shape to the experimental data. Most of them are fixed experimentally and only ν_c, ρ_-, *Conv* and *TofOff* are varied.

4.5.2. Contaminations

The weak point of the ISOL technique is the production of an impure beam. These contaminations could be isobars or molecular impurities that are created in the target or in the ion source. The contaminations could also be produced in ISOLTRAP through charge exchange reactions with the buffer/rest gas, or ionization of rest gas from energetic electrons emitted in beta decay.

Sometimes it is not possible to separate all contaminations from the ions of interest. During the measurements several species could be then present in the same trap. The effect of the presence of a contaminant ion in the precision Penning trap has been extensively studied [Kön+95; Bol+92]. For a low number of ions in the precision trap, two separate resonance curves appear (assuming sufficient resolving power). As the ion number in the trap increases, these two resonance peaks successively approach each other. At the same time, the centroids are shifted to lower frequencies. This can strongly affect the determination of the frequencies of new masses. In order to check for contamination and correct the resulting shift, the frequency is determined for different count rate classes, which means for different numbers of ions that were present in the precision trap for one cycle. The centroid frequencies are plotted as a function of the center of gravity of the count rate distribution in that class. A linear least-squares fit is then applied to the data points. The 1σ confidence interval of the fit is plotted and the frequency and its uncertainty are then deduced from the extrapolation to 0.3 ions (the detector efficiency is 30%). This is called ion-count-class analysis for the frequency determination [Kel+02]. The same software used for the TOF resonance fit is also used to perform this ion-count-class analysis.

4.5.3. The frequency ratio

As it was introduced in the previous chapter (see section 3.1) the mass is related to the cyclotron frequency as the following:

$$\nu_c = \frac{qB}{2\pi m} \tag{4.4}$$

where q and m are the charge and the mass of the ion respectively. Since the magnetic field B is not measured simultaneously with the frequency ν_c, it has to be calibrated

with a known mass. For this purpose, a stable alkali ion source is installed in front of the RFQ-buncher. The stable $^{133}Cs^{+}$, $^{85,87}Rb^{+}$ or $^{40,41}K^{+}$ can be used as reference to estimate the magnetic field at the measurement time. The reference frequency is calculated as:

$$\nu_{ref} = \frac{(\nu_{ref,a} - \nu_{ref,b}).(t_{meas} - t_b)}{t_a - t_b} - \nu_{ref,b} \tag{4.5}$$

where $\nu_{ref,a}$ is the reference frequency measured after the measurement of the frequency of ν_c (of the unknown mass), $\nu_{ref,b}$ the reference frequency measured before, t_{meas} the measurement time of ν_c, t_a and t_b are the measurement times of the reference frequencies $\nu_{ref,a}$ and $\nu_{ref,b}$ respectively. The most important quantity for the mass determination is the ratio between the cyclotron frequency of the reference ion $\nu_{c,ref}$ and that of the ion of interest ν_c. This ratio stays constant while the frequencies shift in time because of the magnetic field drift (see Equation 4.4). The atomic mass is then calculated from this ratio as the following:

$$m = \bar{r}.(m_{ref} - m_e) + m_e \tag{4.6}$$

where m, m_{ref} are the atomic masses of the nuclide of interest and the reference one respectively and m_e is the electron mass. The mean ratio of the frequency ratios of N measurements is given by:

$$\bar{r} = \frac{\sum \frac{r}{\sigma^2_{r,corr}}}{\sum \frac{1}{\sigma^2_{r,corr}}} \tag{4.7}$$

where $r = \frac{\nu_{c,ref}}{\nu_c}$ is the frequency ratio of a single sandwich measurement $\nu_{ref,a}$ / ν_c / $\nu_{ref,b}$ at time a and time b.

The uncertainty of each measurement is calculated as the following :

$$\sigma_{r,corr} = \sqrt{(\sigma_r)^2 + ((t_a - t_b) \times \frac{dB}{dT} \times r)^2} \tag{4.8}$$

where the uncertainty without magnetic drift correction is :

$$\sigma_r = r \times \sqrt{\left(\frac{\Delta\nu_{c,ref}}{\nu_{c,ref}}\right)^2 + \left(\frac{\Delta\nu_c}{\nu_c}\right)^2} \tag{4.9}$$

$(t_a - t_b)$ is the time difference of the reference measurement before and after the ν_c measurement. The magnetic drift or decay for the ISOLTRAP magnet is $\frac{dB}{dT} = 6.35 \times 10^{-10} min^{-1}$ [Kel+02].

As an input to the mass database only a ratio and its uncertainty are needed. Before including these two values one step should be done. The mean ratio (Equation 4.7) should be corrected for the mass-dependent shift [Kel+02] as the following :

$$\bar{r}_{corr} = \bar{r} + \bar{r} \times \Delta_{mass-shift} \tag{4.10}$$

where the absolute mass-dependent shift uncertainty is:

$$\Delta_{mass-shift} = |\delta_{mass-shift} \times (A_{ref} - A)| = |1.6 \times 10^{-10} \times (A_{ref} - A)| \tag{4.11}$$

To lower this uncertainty, the reference mass number A_{ref} should be chosen to be very close to the mass number of the ion of interest A.

The final uncertainty is given by :

$$\Delta(r) = \sqrt{\Delta^2_{stat} + \Delta^2_{mass-shift} + \Delta^2_{res-syst}} \tag{4.12}$$

where the absolute residual systematic uncertainty $\Delta_{res-syst} = \bar{r} \times \delta_{syst}$ with $\delta_{syst} = 8 \times 10^{-9}$ for the ISOLTRAP precision Penning trap [Kel+02] and the absolute statistical uncertainty is given from Equation 4.8 $\Delta_{stat} = \sqrt{\frac{1}{\sum \frac{1}{\sigma^2_{r,corr}}}}$.

To calculate the final mass, the corrected ratio (Equation 4.10) and its uncertainty (Equation 4.12) are included in the matrix of the atomic mass evaluation as described in section 5.1.

4.6. New scheme for mass measurement with the preparation trap

The ISOLTRAP preparation Penning trap is usually used for isobaric purification. In an emergency case (detailed in section 5.4), this trap has to be used as a measurement trap during the neutron-rich krypton isotopes measurements. For this reason, simulations were performed to model the detected ion distribution in order to define a fit function that reproduces the data and test measurements are presented to validate the proposed function[2].

4.6.1. Simulations and fit function

The observable result of the preparation Penning trap is the number N of centered ions which reaches the ion detector behind the trap as a function of the excitation frequency, assuming that only centered ions are detected. The critical condition for the ion detection is thus: $\rho_- < \rho_D$, where ρ_- is the final magnetron radius after the quadrupolar excitation procedure and cooling of the remaining cyclotron motion and $\rho_D = 1.5\,\text{mm}$ is the radius of the trap endcap diaphragm.

The mass resolving power of the preparation Penning trap is $R = \nu_c/\Delta\nu = 10^4 - 10^5$, where $\Delta\nu$ is the full width at half maximum (FWHM) of the ion-count peak versus frequency. Mass measurements require an accurate determination of the center frequency. In standard mass measurements with the TOF-ICR method a fit function determines the center of the measured resonance curve more precisely than obtained by the FWHM of the curve [Kön+95]. Therefore, to achieve similar improvement for cooling resonances, an adequate fit function is needed.

[2] This section was a subject of conference proceeding, Trapped Charged Particles 2010 conference (Finland).

4.6.1.1. Simulation of the cooling resonance shapes

In order to find a suitable fit function for resonance shapes, we first present simulations of the number of detected ions as a function of the quadrupolar excitation frequency obtained in the preparation trap. In this simplified simulation the electric and magnetic fields are assumed to be ideal. Furthermore the Coulomb interaction between the ions is neglected.

Four calculated resonances are shown in Figure 4.8. In each example the ions are created

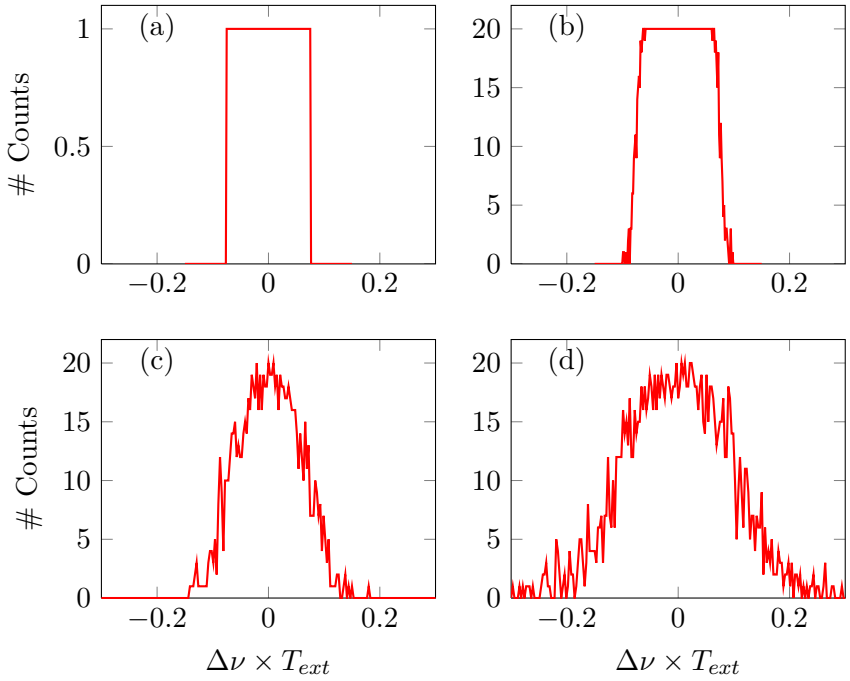

Figure 4.8.: Ion counts as a function of the normalized frequency detuning $\Delta\nu \times T_{ext}$ for different initial-ion configurations in the Penning trap with a diaphragm radius of $\rho_D = 1.5$ mm: (a) single ion, $\rho_0 = 10$ mm, no buffer gas; (b) 20 ions with Gaussian distribution of $\sigma = 1$ mm and $\rho_0 = 10$ mm, no buffer gas; (c) 20 ions, $\sigma = 1$ mm and $\rho_0 = 10$ mm, buffer gas; (d) 20 ions, $\sigma = 2$ mm and $\rho_0 = 7$ mm, buffer gas.

with an initial magnetron radius $\rho_-(0) > \rho_D$. The initial state is a pure magnetron motion, as this is assumed to be the case experimentally after cooling the axial motion and the cyclotron motion. The initial phases of the magnetron motion can be chosen arbitrary, since the conversion of the eigenmotions in a quadrupolar excitation scheme is phase independent if one of the initial radial eigenmotions is zero [Rin+07]. Theoretical count-rate resonances with no buffer gas are shown in Figure 4.8 (a) and (b). In this case, the remaining cyclotron amplitude after the conversion is disregarded since ejection of the ions could not be performed experimentally under these conditions. The amplitude is adjusted to perform one full conversion of magnetron into cyclotron motion. Directly after the conversion, the remaining magnetron radius $\rho_-(T_{ext})$ is considered with the condition that $\rho_-(T_{ext}) < \rho_D$ means that the ion is detected. In Figure 4.8 (a), a rectangular distribution is obtained for a single ion, since the final magnetron radius

after the conversion can only be larger or smaller than the radius of the diaphragm. The result for 20 ions with a Gaussian distribution (with initial magnetron radii having $\rho_0 = 10$ mm for the center and $\sigma = 1$ mm for the standard deviation) is shown in Figure 4.8 (b). In this case the flat top of the resonance as in Figure 4.8 (a) is also obtained, but smooth shoulders appear.

For the conversion of the eigenmotions in the cooling process, a damping force is introduced. Since this is only a qualitative study of resonance shapes, an existing simulation code implementing collisions of $^{133}Cs^+$ ions in ^{4}He buffer gas atoms has been used [Ros09]. The pressure has been adjusted to obtain an average of 20 collisions per ion during the excitation time. The results for the resonance shapes are shown in Figure 4.8 (c) and (d). If the trajectories are disturbed by collisions with atoms, the conversions are incomplete and statistical fluctuations of the ion counts are visible. Depending on the initial ion distribution, this leads to a decrease of ion counts at the center frequency as in Figure 4.8 (c), where the ions are initialized as in Figure 4.8 (b). The flat top as obtained in the theoretical case is not visible for this example. Figure 4.8 (d) shows a resonance obtained using a larger distribution of ions ($\sigma = 2$ mm) and a smaller initial distance to the trap center ($\rho_0 = 7$ mm). This results in a broader resonance shape where a clearly flattened top is visible. Furthermore, background fluctuations of the ion counts are obtained since the condition for the detection can already be obtained after the initialization.

Based on these results, a fit function is needed which takes a flattened top of the resonances into account. Thus, to first approximation, a smooth step function fulfills this condition.

In this simulations only two phenomena were studied (the real ion bunch and its behavior in a gas) to evaluate the deviation from the ideal case of one ion in the trap and in vacuum. Many other phenomena can modify the shape of the resonance not only the smoothness of the shoulders but even introduce asymmetry, here are some examples:

- If a large amplitude is applied to the ring electrodes to center the bunch of ions, then beating between cyclotron motion and magnetron motion develops. This may lead to a phase dependent behavior in the shoulders.
- The cyclotron cooling[3] after centering is very important before the ion package ejection. If this process is not done properly, an asymmetry can appear in the cooling resonance. This is because part of the ion bunch is still on cyclotron orbit and when ejecting them this part is lost and don't reach the detector.
- When the ions are ejected from the trap they follow the magnetic fields lines: $\frac{r(z)}{r(z=0)} = \sqrt{\frac{B(Z=0)}{B(z)}}$. So if the magnetic field drops to 1% of the original value, the radius of the ion cloud will increase by a factor of 10. Thus, the diameter of the ion beam can reach easily few centimeters. So, the transmission to the detector depends on the position of the ion when they are ejected (trap hole is about 4 mm).

[3] Called also radial cooling (see Figure 4.7).

- The imperfection of the ion's detector, especially if the efficiency depends on the position of the ion's impact on the detector will induce some asymmetry. The detector can be also saturated if a lot of ions are send and the signal could be cut, mainly around the resonance frequency where the count rate is higher.

These phenomena should be studied in order to evaluate their effect on the cooling resonance's shape.

4.6.1.2. Smooth step-function fit

According to simulations, the smooth step-function fit parameters are: the background, the amplitude, the width, the smoothness of the shoulders and the center frequency. When viewed upside down, the rounded step function resembles the well-known Woods-Saxon radial nuclear potential [WS54]. The defining feature of this potential are the so-called shoulders. To fit the full shape of the resonance, we expand the form over both quadrants to obtain a 'Double Woods-Saxon' (DWS) function:

$$DWS(\nu) = b + \frac{a}{1 + exp\left(\frac{\nu-\nu_c-\Delta}{s}\right) + exp\left(-\frac{\nu-\nu_c+\Delta}{s}\right)} \tag{4.13}$$

where a is the amplitude, b the background, ν_c the center frequency (here, the cyclotron frequency), Δ the semi-width at half maximum and s the smoothness of the shoulders. The DWS fit is shown for measured resonances of $^{94}Kr^+$ and $^{133}Cs^+$ in Figure 4.9.

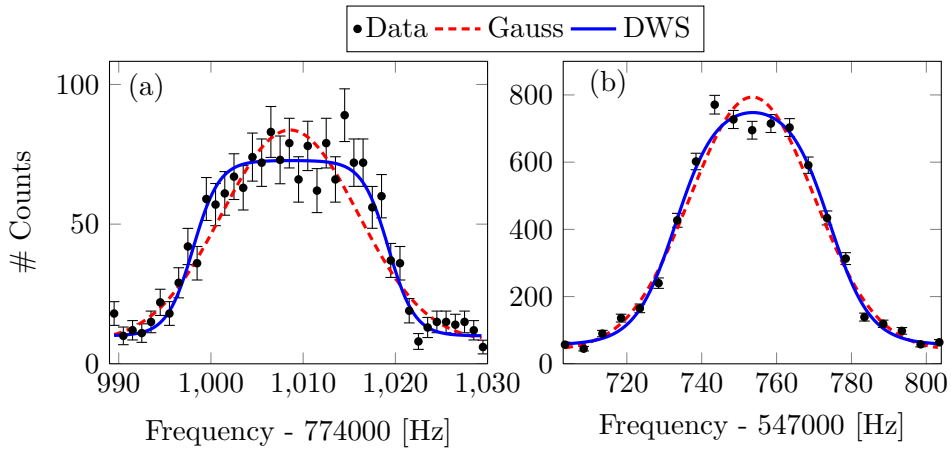

Figure 4.9.: Preparation trap data: (a) $^{94}Kr^+$ and (b) $^{133}Cs^+$, fitted with Gaussian (dashed line) and the Double Woods-Saxon function (solid line). See Table 4.2 for details of the fits.

4.6.1.3. Other approaches

The data were analyzed using two other approaches in order to check the coherence with the Double Woods-Saxon function results.

Gaussian fit Often cooling resonances of the form shown in Figure 4.8 (c) are obtained experimentally. Until now, cooling resonances from the preparation trap have always been fitted by a Gaussian distribution [Kol+04; Rah+06; Kow+09]. Such fits are also shown in Figure 4.9 for comparison with the proposed DWS function.

Center of gravity and standard deviation of a peak The peak of the cooling resonance can be considered as a probability density function with a random variable $n_i - b_i$ (where b_i is the background). The first moment which identifies the frequency mean, is then:

$$\bar{\nu} = \frac{\sum_i \nu_i.(n_i - b_i)}{\sum_i (n_i - b_i)} \tag{4.14}$$

where ν_i is the frequency and n_i is the number of observed counts at this frequency i. The background is determined as: $b_i = (n_r + n_l)/2 = b$, where n_r and n_l are the background on the right and the left sides. This background is considered constant for each resonance. This assumption is sometimes not valid for resonances which have an asymmetric background distribution. The uncertainty of the frequency is obtained as described in [Eph+79] by:

$$\delta\nu = \frac{1}{\sqrt{\sum_i (n_i - b_i)}} \sqrt{\frac{\sum_i \nu_i^2.(n_i - b_i)}{\sum_i (n_i - b_i)} - \left[\frac{(\sum_i \nu_i.(n_i - b_i))}{\sum_i (n_i - b_i)}\right]^2} \tag{4.15}$$

This method is unstable because it depends on the choice of the background, which is not the same for all resonances since the frequency range can change from one resonance to another. It depends also on the quality of the data, for example low statistics makes the choice of the background crucial for the determination of the center frequency. However, this method gives very good results for symmetric resonances with high statistics.

4.6.2. Results

From Table 4.2, we see that the three different methods give the same center frequencies within their uncertainties. The frequencies given by the Gaussian fit and the center-of-gravity method are influenced by the fluctuations of ion counts in the flattened top of the cooling resonance. The advantage of the DWS fit is the small impact of such fluctuations or asymmetry on the center frequency. This can be seen from the reduced χ^2 achieved by the fit compared to the Gaussian fit in Table 4.2. Many measurements of different known masses (^{86}Kr and ^{85}Rb) were performed in this trap and the DWS function gives a better fit.

In Figure 4.10, we show resonances from the precision and preparation trap of $^{94}Kr^+$ with the same excitation time $t_{rf} = 100$ ms and the same number of ions (~ 1800). The frequencies given by the fit functions have almost the same statistical uncertainty: $\delta\nu/\nu \approx 2.5 \times 10^{-7}$ for the precision trap and 2.3×10^{-7} for the preparation trap. Detailed investigation of systematic effects on cooling resonances would have to be performed before comparing the accuracies of the two mass measurement methods. The proposed DWS function would seem at least to offer a good fit of the cooling resonances and gives a reasonable result for this preliminary mass measurements. In addition, the

Table 4.2.: Comparison of the results of the three methods used to analyze the cooling resonance data. **DWS**: the smooth step function or Double Woods-Saxon fit, **GAUSS**: the Gaussian fit and **Moment**: Center of gravity and standard deviation of a peak. The frequencies of $^{94}Kr^{+}$ and $^{133}Cs^{+}$ are shown with their uncertainties. The third column shows the reduced χ^2 of the fits (see also Figure 4.9).

Method	^{94}**Kr**$^{+}$			^{133}**Cs**$^{+}$		
	Frequency ν_c (Hz)	$\Delta\nu$	χ^2/n	Frequency ν_c(Hz)	$\Delta\nu$	χ^2/n
DWS	775008.66	0.18	1.2	547753.64	0.23	3.7
GAUSS	775008.58	0.25	2.4	547753.51	0.24	6.1
Moment	775008.97	0.20	-	547753.63	0.20	-

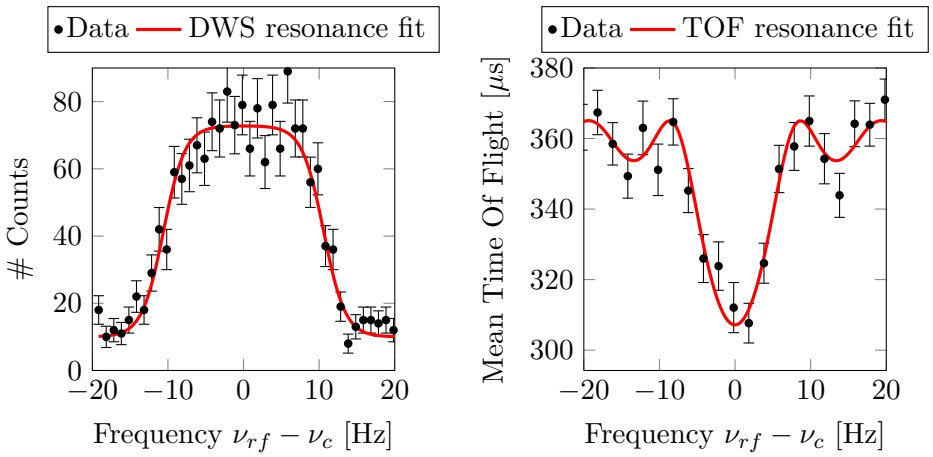

Figure 4.10.: $^{94}Kr^{+}$ TOF (right) and cooling resonances (left) taken in the precision and the preparation traps, respectively. The two resonances are taken with the same excitation time t_{rf} = 100 ms and correspond to the same number of ions and frequency range.

DWS fit offers a good tool for the identification of various contaminations. Moreover, the amplitude of the DWS fit could be used to compare predictions for the relative production of different species (see discussion in [Rah+06]).

5. Mass measurement results and evaluation

Results of mass measurements, mainly frequency ratios, from ISOLTRAP are included in the atomic mass evaluation to check their consistency. In this chapter a brief description of the atomic mass evaluation is given as an introduction to the detailed discussion of the measurements and the resulting masses.

5.1. The atomic mass evaluation AME

The atomic mass evaluation or "mass table" is more than a simple compilation of several experimental data. The key of understanding the atomic mass evaluation is to keep in mind the paradox that the masses themselves are not measured; only the link between them. There is only one absolute mass which is the Carbon-12 mass for the simple reason that the mass unit is defined as $1u = M(^{12}C)/12$. The ^{12}C atomic mass is then 12 and its mass excess [1] is zero. The atomic masses can be seen as a surface in 2D plane (N,Z) with one fixed point (^{12}C mass). The links between nuclides are described by linear equations with the atomic masses as variables. Each link or equation represent a measurement from: nuclear reactions, β-decay, Penning trap, etc. Due to the experimental technical developments in the last few decades many measurements were performed and many masses are multiply determined. Thus, the ensemble of these links generates a highly entangled network which is represented by a huge matrix. To take into account these correlations, a least-square method is used weighed with the precision of the measurements. This method allows the determination of adjusted masses. For each new series of measurements the whole mass surface is adjusted and all masses could be influenced by the new links depending on their weight. Masses already measured with high precision[2] are less influenced due to their high weight in the matrix. Very short-lived nuclides are more influenced in the mass evaluation since they usually have lower precision. For this reason the atomic mass evaluation is very important for the determination of new masses of short-lived nuclides, not only for the ones measured but also for the short-lived nuclides masses in the close network area (see Figure 5.1). The details of the atomic mass evaluation can be found in [AWT03].

5.2. Mn isotopes

The manganese isotopes were created using a Uranium Carbide UC_x target on the General Purpose Separator GPS and ionized by a Resonance Ionization Laser Ion Source

[1] Defined as the difference between the atomic mass (in mass unit) and the mass number.
[2] Usually masses of stable or close to the stability nuclides are measured with high precision.

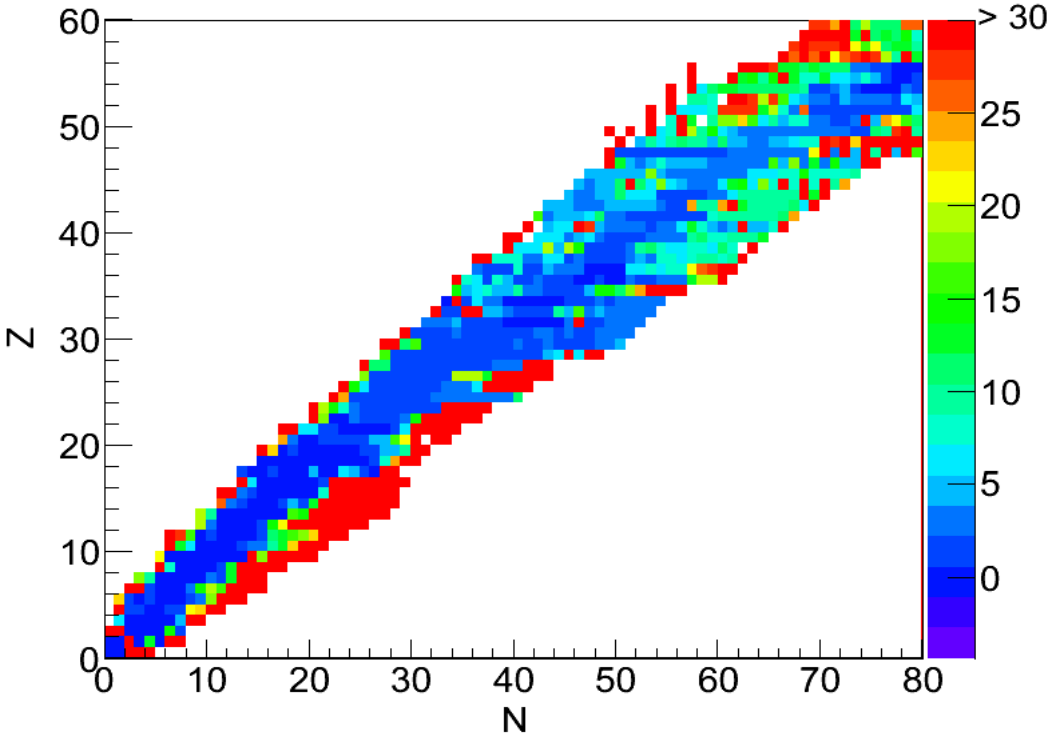

Figure 5.1.: The mass surface shown as the precision on the mass excess in the light region of the nuclear chart. The masses measured with high precision have more weight and are close to zero (it is then very difficult to influence them with new measurements). The values shown in this plot are the results of the updated AME2010 [Aud10].

RILIS which employed the solid state laser [Kos02].

The masses measured here are the result of two beamtimes: summer 2006 ($^{57-63}$Mn,$^{61-63}$Fe) and summer 2009 ($^{55,64-66}$Mn, ^{48}Ti) as shown in Figure 5.2. The iron isotopes were not produced with ISOLDE but in the ISOLTRAP setup by the decay of the manganese isotopes inside the preparation trap: the in-trap decay method [Her+05].

In the first beamtime ^{39}K was used as a reference for the cyclotron frequency measurement while for the second beamtime ^{85}Rb and ^{64}TiO were used as references and for cross checks.

For the first beamtime, no contaminants were observed. In the second beamtime, two contaminant were observed: ^{66}Ga and the stable molecules $^{64-66}$TiO. With the resolving power of the preparation trap the titanium oxide molecules were easily removed from the beam (see Figure 5.3). The ^{66}Ga was more difficult to resolve due to high abundance and a second dipole excitation frequency was applied at ν_+ of the contaminant in the preparation trap. This frequency was applied during the whole cooling process in order to disturb the ^{66}Ga ion motion and avoid the re-centering of this unwanted ion (see section 4.1).

^{58}*Mn*

We measured the frequency ratio between the exited isomeric state of ^{58}Mn and ^{39}K.

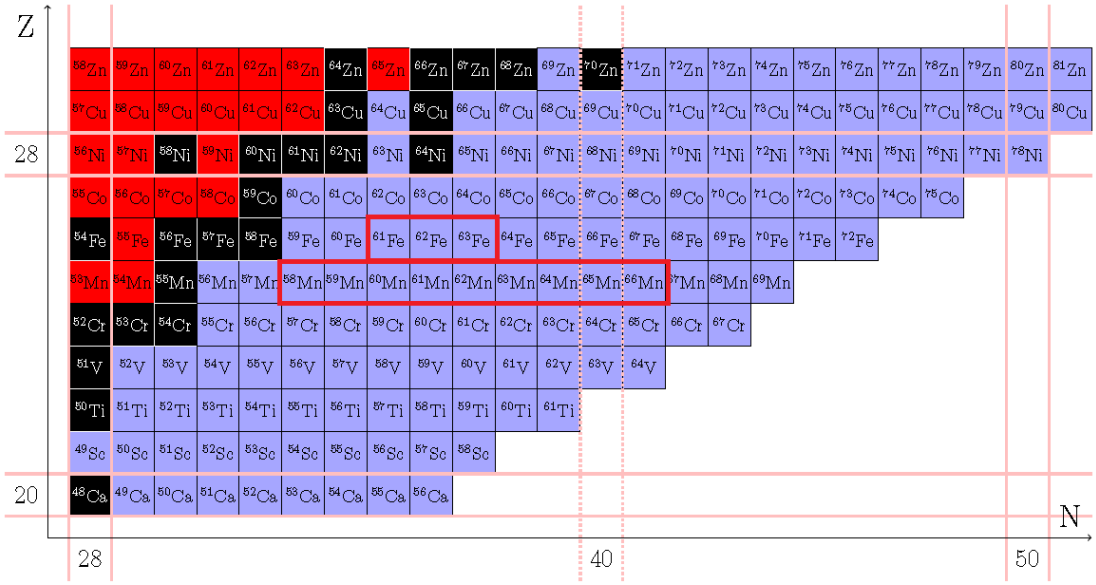

Figure 5.2.: Part of the nuclear chart where the measurements of Mn and Fe isotopes were performed. In black boxes are the stable nuclides, blue and red are unstable nuclides and decay via β^- and β^+ respectively.

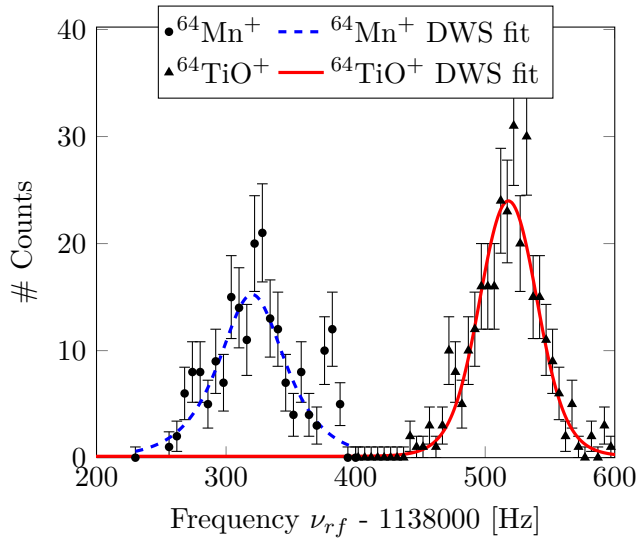

Figure 5.3.: A = 64 cooling resonances in the preparation trap. The contamination titanium oxide $^{64}TiO^+$ was 200 Hz away from the $^{64}Mn^+$ frequency and easily removed.

The frequency used for the mass evaluation is the frequency of this excited isomer which was more abundant than the ground state. Since the excitation energy is well known (71.78 ± 0.05)keV we used this measurement to derive the mass of the ground state, $M_{gs} = M_{measured} - 71.78$ keV.

The decay of ^{58}Mn has been studied by Flynn *et al.* [FSA77] using the reaction ^{58}Fe$(t,^3 He)^{58}$Mn. From the spectra of ^{3}He they observed 16 states (or groups). Because

of the width of the 0^+ peak (larger than the other states) they assumed that the group 0 Q = -6318±15 keV is a mixture of the ground state and an exited isomeric state that they supposed to be located at E_x = 30±10keV. The Q value measured in their experiment was corrected to Q = -6300± 30 keV and they gave a mass excess of -55832±30 keV. Later, Schmidt-Ott *et al.* [Sch+92] discovered the exited isomeric state at 71.78±0.05 keV with 68±9 s half-life. The mass of ^{58}Mn was then erroneously corrected in AME1993 and AME2003 as being Q = -6300± 30 keV from the isomer ^{58}Mn^m, the mass excess was thus -55907±30 keV in the AME2003. Re-examining the paper of Flynn *et al.* [FSA77] under the light of the most recent Evaluated Nuclear Structure Data File (ENSDF) [Tul10] evaluation, we found that the first excited state, group 1, at 77±8 keV identified by Flynn *et al.* is precisely the exited isomeric state in ENSDF at 71.78±0.05 keV. This means that the group 0 in [FSA77] was not a mixture but a pure ground state. Their original Q value should not be corrected and the mass excess should thus be -55817±15 keV which agrees with the ISOLTRAP value -55827.4±2.7 keV within quoted errors. Earlier, two more results could determine the mass of ^{58}Mn from β-decay [WPK69] and [DH71] with total a Q_β of respectively 5890±100 keV and 5958±100 keV. Our measurement combined with the ^{58}Fe mass results in Q_β 6326.8±2.8 keV and is in strong disagreement with both Q_β data. The new adjusted $(t,^3He)$ energy -6308.1±2.8 keV is in very good agreement with the original Flynn's result.

^{59}*Mn*

The mass of ^{59}Mn was measured by Kashy *et al.* [Kas+76] using the reaction ^{64}Ni(^{3}He,^{8}B)^{59}Mn and by [Par+77] at Argonne National Lab from β-decay. The latter carrying no weight (Q = 5200±100 keV), only the former was used previously, resulting in AME2003, a mass of -55480±30 keV. The figure of the energy spectra (fig 1 in this paper) shows that the peaks have 270 keV width. The error of 30 keV is maybe too optimistic and we can estimate (from their figure) an error of 50 keV.

The ISOLTRAP value -55525.1±2.3 keV agrees with the Kashy *et al.* [Kas+76] value, but now carries all the weight for the determination of the ^{59}Mn mass.

^{60}*Mn*

We measured the frequency ratio between the excited isomeric state of ^{60}Mn and ^{39}K. The excited isomeric state is known to be at 271.90±0.10 keV. With the resolving power of our Penning trap the ground state and the excited isomeric state were resolved.

The decay of ^{60}Mn has been studied by Norman *et al.* [Nor+78]. Its half-life was reported to be 1.79±0.1 s and 3^+ was proposed to be the ground state's spin and parity. The Q_β value was measured to be 8510±100 keV which correspond to a mass excess of -52890±100keV. Later [Run+85], this 3^+ level was shown to be an excited isomeric state. The first measurement of the presumed 0^+ ground state's half-life was achieved by Bosch *et al.* [Bos+88]. A half-life of 51±6 s was deduced from multiscaled β singles counting rate. Recently [Lid+06], the half-life of the ^{60}Mn ground state has been measured to be 0.28±0.02 s and a new spin parity of 1^+ and 4^+ were assigned to the ground and excited isomeric state, respectively. The Q_β value was corrected and the mass excess was -53178±90 keV. Our measurements give a Q_β of 8445±4 keV and a mass excess of -52967.7±2.3 keV. According to this value and the new spin parity state of ^{60}Mn and

$^{60}Mn^{m}$, we propose a transition from the excited isomeric state 4^{+} to the 4_2^{+} of ^{60}Fe at 3072 keV γ-ray and not to 4_1^{+} at 2792 keV γ-ray. This change of the transition can explain the missing 211 keV.

^{61}*Mn*

The mass of ^{61}Mn was measured before in three TOF experiments by the same TOFI group at Los Alamos [Tu+90; Sei+94; Bai+98], the average gave the excess mass value of -51556±228 keV. The ISOLTRAP measurement gives a value of -51741.9±2.3, in agreement with the previous value. Our value is chosen to carry all the weight due to the higher precision of our measurement.

^{62}*Mn*

For this nuclide we took only the resonances with 1.2 s excitation time. Thus, only the mass of the long lived high spin isomer [Han+99] was measured because the short lived isomer has a half-life of 92±13 ms. Until now it is not known which one of these two isomers is the ground state. In AME2003 the high spin one has been previously labeled *gs*, as in ENSDF2000.

Previously, the ^{62}Mn mass was given from the average of three TOF experiments by the same group (Los Alamos)[Tu+90; Sei+94; Bai+98] and the value reported in AME2003 is -48040±220 keV. Our mass excess value is -48180.7±2.6 keV and agrees with the previous measurements but again carries all the weight.

^{63}*Mn*

The mass of ^{63}Mn was measured before in the TOF experiments [Tu+90; Sei+94; Bai+98]. Recently, it was measured by [Knö08] and its mass excess was -47347±95 keV. This value deviates from the ISOLTRAP measurement with 4.8σ. Dues to its small uncertainty, the ISOLTRAP mass excess -46886.9±3.7 keV is taken to carry all the weight.

^{64}*Mn*

Again the mass of ^{64}Mn was given by the average of three TOF measurements [Tu+90; Sei+94; Bai+98], the mass excess given was -42620±270 keV. The ISOLTRAP measurement gives a value of -42989.0±3.5 keV. The [Tu+90] and [Bai+98] values are 1.5 σ and 1.2 σ respectively away from our measurement, the value reported in [Sei+94] is only 0.4 σ away. These deviations are still reasonable, so the ISOLTRAP value is kept and carries all the weight.

The excited isomer is not present here because of its short half-life of 500 ± 50 μs [Gau05].

^{65}*Mn*

The mass of ^{65}Mn was given in AME2003 from the average of two TOF measurements, and the mass excess was reported to be -40670±540 keV [Sei+94; Bai+98]. The ISOLTRAP measurement gives -40967.3±3.7 keV for the mass excess. This value is in a good agreement with the previous measurements. Due to the large error bars on the previous measurements, ISOLTRAP is kept and the two other values were not used in the calculation (out weighted).

^{66}*Mn*

The mass of ^{66}Mn is measured at ISOLTRAP for the first time. Its half-life is 64.4±1.8 ms which is a new record for our Penning trap. The ISOLTRAP measurement gives a mass excess of -36750.4±11.2 keV.

The excited isomeric state measured recently by Gaudefroy *et al.* [Gau05] with a half-life of 750±250 μs is not present during our measurement.

5.3. Fe isotopes from in-trap decay of the Mn isotopes

As mentioned above, the iron isotopes were not produced by ISOLDE but in the ISOLTRAP setup via the in-trap decay method [Her+05]. To get the Fe isotopes, the storage time in the preparation trap has to be increased to allow the Mn isotopes decay to Fe. The axial cooling[3] was increased therefore to 1 s. The preparation trap electrical potential is very important here to trap ion with the recoil kinetic energy. In the case of β-decay, the mass of the daughter is several orders of magnitude larger than the mass of the emitted particle, *e.g.* an electron or a positron. Thus, the fraction of the decay energy transferred to the recoil ion is not more than a few 100 eV (the depth of the preparation trap is 100 V). The presence of the buffer gas in the preparation trap is an important feature for the in-trap decay process since the decay 'heat' (energy of the recoiling Fe) must be cooled. Once the recoiling iron isotopes were created and trapped in the trap potential they were cooled by collisions with the buffer gas, the selection and different excitations were applied and the clean iron beam was transported to the precision trap where the mass measurement was performed. More technical details of the following measurement using the in-trap decay method will be given in a future publication by Herlert *et al.*.

^{61}*Fe*

The mass of ^{61}Fe was deduced from the ^{64}Ni(α,^{7}Be)^{61}Fe reaction [CTK77]. Their mass excess is -58920±20 keV, with a good agreement with our value -58920.30±2.6 keV. Our mass excess is taken to carry all the weight.

The excited isomeric state of ^{61}Fe has a half-life of 250±10 ns, too short to be present in our trap.

^{62}*Fe*

The mass of ^{62}Fe was measured in several heavy ion reaction experiments on ^{64}Ni but only four of them were used to calculate the average of the mass excess given in the AME2003 is -58901±14 keV [Ber+81; Hic+76; Bha+77; Hau+84]. The ISOLTRAP value of -58877.8±2.8 keV agrees with all these except with [Bha+77], which is 2 σ away. Because of their low uncertainties, ISOLTRAP has 100 % influence.

[3] This time is necessary to cool the axial ion motion since they come with kinetic energy of few hundred eV from the cooler-buncher. The ions are trapped in the trap potential and lose their energy by collision with the buffer gas present in the preparation trap (see section 4.1). The axial cooling is applied before the magnetron excitation and the cooling/selection process.

^{63}Fe

The mass of ^{63}Fe was measured in three TOF experiments [Tu+90; Sei+94; Bai+98] whose average gave a value of -55550±170 keV. The ISOLTRAP measurement gives a mass excess of -55636.6±5.7 keV which is in a good agreement with the TOF experiments. The ISOLTRAP mass excess -55636.6±5.7 keV is also in good agreement with the recent LEBIT value [Blo+08] -55630.7±9.6 keV. The final mass is then the average of both trap measurements -55635±4.9 keV with a normalized χ_n of 0.52.

5.4. Kr isotopes

Two krypton isotopes were measured with ISOLTRAP for the first time, ^{96}Kr and ^{97}Kr. The Kr nuclides were produced by irradiating a $50 g/cm^2$ uranium-carbide UC_x target combined with a water-cooled transfer line and a new versatile arc-discharge ion source (VADIS) [Pen+08]. The singly-charged ions were transported at 30 keV through the two-stage high-resolution mass separator (HRS) into ISOLTRAP. These measurements suffered a lot from charge exchange of the noble gases with the residual gas in the RFQ-Buncher and the preparation trap. Because of the loss due to the charge exchange and the short half-life (63±4 ms), the mass of ^{97}Kr was measured in the preparation trap as described in section 4.6. The measurement of ^{97}Kr was done using as a reference ^{86}Kr while for ^{96}Kr, ^{85}Rb was used as a reference. Several known masses were remeasured during the same run in the precision and preparation trap for the cross check of the system (^{133}Cs, ^{85}Rb, ^{80}Kr, ^{86}Kr, ^{87}Kr, ^{94}Kr). All noble gases measurements performed in the preparation trap show a shift in the frequency probably due to the presence of decay products and charge exchange products. To compensate this effect an error of 1×10^{-6} was added to the final error on the frequency ratio for all the Kr isotopes measurements performed in the preparation trap. This trap was used for the first time to measure masses. Since no studies were done before to determine the systematic error of this trap, we estimate an error of 4×10^{-7}, which was added to each measurement.

^{96}Kr

Five resonances of the ^{96}Kr were taken during the run (Appendix B), one with an excitation time $t_{rf} = 50$ ms, three with $t_{rf} = 100$ ms and one with $t_{rf} = 200$ ms (see Figure 5.4).

In the case of ^{96}Kr the lighter dominating contamination is due to charge exchange and decay products as seen from the time-of-flight spectrum in Figure 5.5.

Because of the low statistics of three Kr resonances, the count-rate-class analysis was not possible. The error on the frequency of these resonances were multiplied by a factor deduced from the count-rate-class analysis of the two other resonances of the same isotope (with higher statistics). It is assumed that for the same element and the same mass number, the behavior of the count rate classes is similar. So the errors of the frequencies of the three resonances were all multiplied by a factor of two.

The results of the atomic mass of ^{96}Kr in the precision trap are given in Table 5.2 as mass excess.

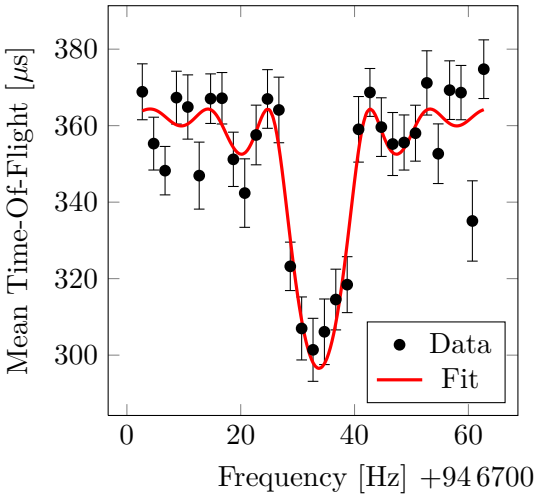

Figure 5.4.: One of the Time-Of-Flight resonance of ^{96}Kr with $t_{rf} = 100$ ms, taken from the precision Penning trap.

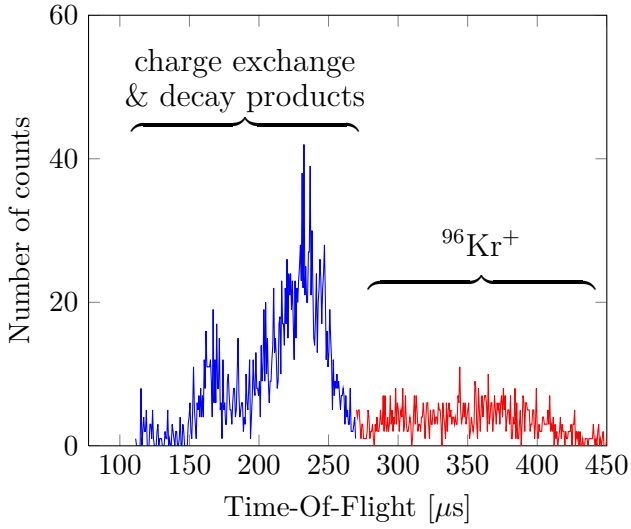

Figure 5.5.: Time of flight spectrum of ^{96}Kr from the precision trap to the ion detector.

^{97}*Kr*

The ^{97}Kr beam was produced at ISOLDE with a relatively low yield. The short half-life (63 ms) and the noble gas chemical properties, which lead to rapid neutralization, generate a huge loss of the ^{97}Kr beam. Because of the low yield, the short half-life and the loss due to charge exchange, it was not possible to transport this beam to the precision trap. In Figure 5.6 the loss due to charge exchange is shown with storage time in the preparation trap. The loss of the ^{80}Kr beam is decreasing with the storage time, while the resulting H_2O (charge exchange product) is increasing. Transporting the beam to the precision trap requires a very good cooling in the preparation trap which means an increase of the storage time. Therefore and for the first time, the ISOLTRAP's

preparation trap was used to measure masses which allowed the measurement of the ^{97}Kr mass for the first time.

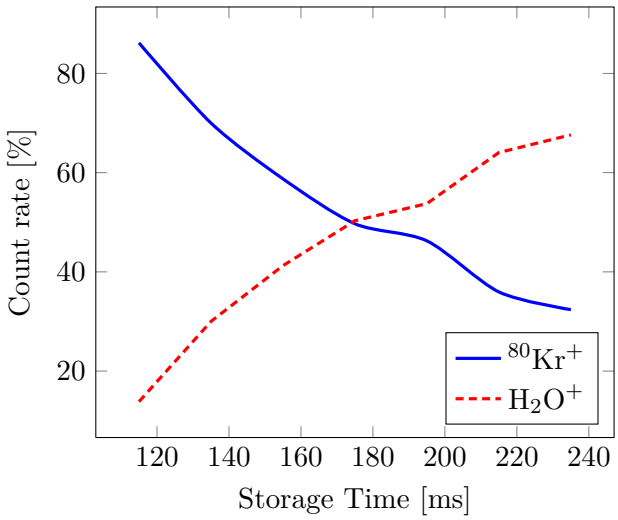

Figure 5.6.: The charge exchange loss behind the preparation trap for $^{80}Kr^+$. The storage time plotted is the sum of all the timings needed for the cooling process: the axial cooling of 60 ms, the magnetron excitation of 10 ms, the cyclotron excitation of 35 ms and the cyclotron cooling which was changed for each point of the figure from 10 ms to 130 ms

Four cooling resonances were taking during the run (see Appendix B), two with excitation time $t_{rf} = 50ms$ and two with $t_{rf} = 100ms$. Because of some technical problems with the ISOLTRAP's alkali reference ion source, the stable ^{86}Kr was used as a reference instead of the ^{85}Rb. Later on, many cross checks were done measuring different known masses (^{133}Cs, ^{86}Kr, ^{94}Kr using as reference ^{85}Rb or ^{86}Kr). The Double Wood-Saxon fit function (DWS) was used to fit the cooling resonance as described in section 4.6.

Uncertainties treatment For noble gases, a shift in frequency was observed probably due to space charge effects [Stu+09][4]. The time-of-flight spectra show many contaminations present in the preparation trap. Four examples are shown in Figure 5.7, the first and second show the TOF spectra of the stable ions ^{86}Kr & ^{85}Rb, the third and the fourth show the TOF spectra of the unstable isotopes ^{97}Kr & ^{64}Mn. A big difference can be seen between TOF spectra of stable ions and radioactive ones. The stable TOF spectra are much cleaner than the unstable TOF spectra. One can attribute the presence of the contamination to the ionization of the buffer gas and the impurities present in the trap with the highly energetic β particles emitted during the decay process. However, some contamination (mainly H_2O^+) is present in the stable ^{86}Kr TOF spectrum. This can be explained by the charge exchange property of the noble gases and the presence of H_2O inside the trap. From these observations, it is not easy to predict quantitatively this shift in the frequency. For this reason more studies should be done, to understand

[4]This frequency shift was also observed in other Penning trap experiments such as REX-ISOLDE. This phenomena is still not fully understood but many studies are under investigation.

the shift due to space charge effect and to understand the ionization of the buffer gas. Such studies are being investigated with ISOLTRAP and other Penning traps [Her+10]. The results of these studies will be a big help first for the ISOLTRAP experiment and also for all experiment using the gas-filled Penning trap technique.

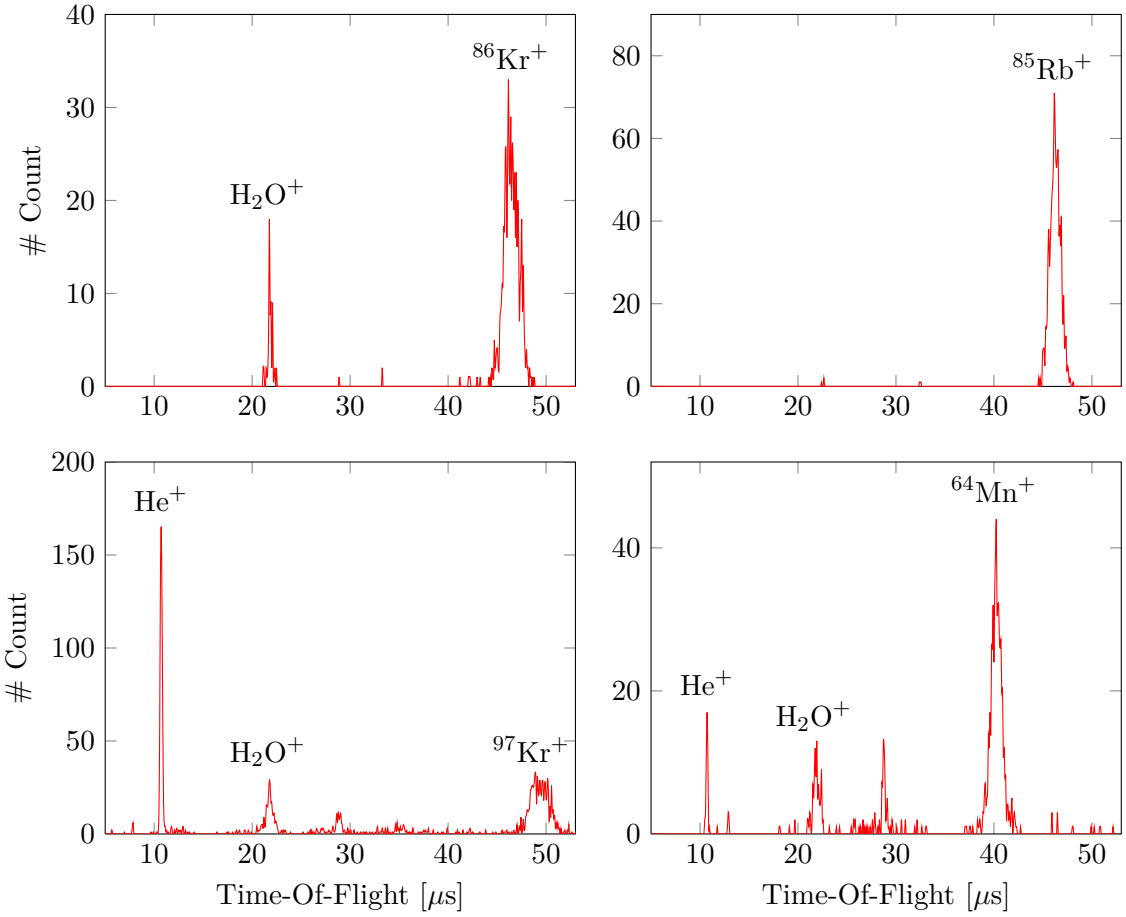

Figure 5.7.: Time-Of-Flight spectra from the preparation trap to the detector placed behind for different injected beams (^{86}Kr, ^{85}Rb, ^{97}Kr & ^{64}Mn.)

Because of this problem, an additional systematic error was added only to the noble gas data and the final uncertainty (Equation 4.12) became :

$$\Delta(r) = \sqrt{\Delta^2_{sys} + \Delta^2_{mass-shift} + \Delta^2_{charge-exchange}} \tag{5.1}$$

with $\Delta_{charge-exchange} = \bar{r} \times \delta_{charge-exchange}$ where the relative charge exchange error is estimated to be $\delta_{charge-exchange} = 1 \times 10^{-6}$. This error is added to the final uncertainty in such a way that the calculated mass excess of the known Kr isotopes (^{86}Kr & ^{94}Kr) agree with the tabulated mass excesses within the error bars. This method is nothing else than inflating the final uncertainties to hide the shift problem. A cleaner method would be an estimation of this shift from a thorough study of the noble gases behavior in such conditions.

Note from Equation 5.1 and in comparison to Equation 4.12, the so-called absolute residual systematic uncertainty $\Delta_{res-syst}$ and the statistical uncertainty are not present in this equation. Unlike the precision trap, the preparation trap was used for the first time to measure masses, so no systematic studies were performed before to estimate the systematic uncertainty related to the operating system. A large dispersion of the data points has to be expected without adding any residual systematic error. Indeed, for each known isotope (^{133}Cs, ^{86}Kr & ^{94}Kr) a large reduced χ^2 is observed, see Table 5.1. One has to add an error to compensate this lack of information. The more intuitive way to add this error is to look to the dispersion of the data and try to reduce it until getting a normal distribution around 1 of the χ^2_{red}, see last column of Table 5.1.

This error is not added quadratically to the final uncertainty as it is the case for the precision trap (Equation 4.12), but it is added to each data point and the Equation 4.8 became:

$$\sigma_{r,corr} = \sqrt{(\sigma_r)^2 + ((t_a - t_b) \times \frac{dB}{dT} \times r)^2 + \delta_{res-syst}} \tag{5.2}$$

with $\delta_{res-syst} = 4 \times 10^{-7}$ deduced from the behavior of the χ^2_{red}. The error is added to the final uncertainty via what is called Δ_{sys} in Equation 5.1 as the following:

$$\Delta_{sys} = \sqrt{\frac{1}{\sum \frac{1}{\sigma^2_{r,corr}}}} \tag{5.3}$$

Table 5.1.: Reduced χ^2 calculated for each nuclide before and after adding the relative residual systematic error $\delta_{res-sys}$. The second column shows the nuclide used as a reference for each measurement. The third column shows the number of resonances (or data points) taken for each nuclide.

Nuclide	Reference Nuclide	Number of Resonances	χ^2	χ^2 after adding systematic error
^{86}Kr	^{85}Rb	5	3.5	1.1
^{94}Kr	^{85}Rb	4	3.8	1.8
^{94}Kr	^{86}Kr	2	0.1	0.1
^{133}Cs	^{85}Rb	3	1.1	0.9
^{97}Kr	^{86}Kr	4	0.3	0.3

The results of the ^{97}Kr mass measurement performed in the preparation trap are given in Table 5.2.

5.5. Mass values

The final masses obtained in this work are summarized in Table 5.2. After the Mn and Fe isotope mass measurements, some ^{48}Ti^{16}O resonances were taken with ^{85}Rb as

reference in order to check the system. The resulting mass of this cross check showed that the ISOLTRAP measurement contributes to the mass determination of ^{48}Ti with 16.7 % in the updated AME [Aud10] (see Table 5.2). Other cross checks were performed using the stable ^{55}Mn using as a reference the ^{48}Ti^{16}O and ^{85}Rb and here again the ISOLTRAP measurement contributes to the updated AME with 56.1 %. Also for ^{57}Mn with ^{39}K as reference, the ISOLTRAP measurement contributes to the updated AME with 33.3 %.

Concerning the Kr isotopes, the contribution to the updated AME is 100% for both ^{96}Kr and ^{97}Kr since they were measured for the first time.

Table 5.2.: Mass excesses of all nuclides to which the ISOLTRAP measurements contribute. The contribution is shown in the last column as a percentage.

Nuclide	Half-life	ISOLTRAP ME [keV]	AME2003 ME [keV]	Influence on AME2010
^{48}Ti	Stable	-48491.7(0.4)	-48487.7(0.8)	16.7 %
^{55}Mn	Stable	-57711.6(0.5)	-57710.6(0.7)	56.1 %
^{57}Mn	85.4(1.8) s	-57486.1(1.5)	-57486.8(1.9)	33.3 %
^{58}Mn	3.0(0.1) s	-55827.4(2.7)	-55907(30)	100%
^{59}Mn	4.59(0.05) s	-55525.2(2.3)	-55479(30)	100%
^{60}Mn	0.28(0.02) s	-52967.8(2.3)	-53178(80)	100%
^{61}Mn	0.67(0.04) s	-51742.0(2.3)	-51556(228)	100%
^{61}Fe	5.98(0.06) m	-58920.3(2.6)	-58920(20)	100%
^{62}Mn	0.671(0.005) s	-48180.8(2.6)	-48039(223)	100%
^{62}Fe	68(2) s	-58877.9(2.8)	-58901(14)	100%
^{63}Mn	0.275(0.004) s	-46886.9(3.7)	-47347(95)	100%
^{63}Fe	6.1(0.6) s	-55635.5(4.3)	-55546(168)	57.3%[a]
^{64}Mn	88.8(2.5) ms	-42989.0(3.5)	-42617(267)	100%
^{65}Mn	0.092(0.001) s	-40967.3(3.7)	-40673(537)	100%
^{66}Mn	0.064(0.002) s	-36750.4(11.2)		100%
^{96}Kr	0.080(0.007) s	-53079.7(20.5)		100%
^{97}Kr	0.064(0.004) s	-47423(130)		100%

[a] The other contribution is from the LEBIT Penning trap [Blo+08].

The impact of these new results is discussed in the next chapter.

6. The new mass surface: hints for nuclear structure

Nuclei, like other systems, minimize their internal energy. Sometimes this leads to deformed ground state which can have large consequences on how the nucleons arrange themselves inside the nucleus. Studying nuclei with such properties can bring an important contribution to the puzzle of understanding the nuclear force.

The total binding energy is the result of the minimization of all interactions acting inside the nucleus. Mass derivatives can therefore be used to filter and probe some specific effects. In this work, mass derivatives in two different mass regions will be studied in order to probe effects responsible for sudden changes in nuclear structure.

6.1. N = 40 shell closure

When moving towards more exotic nuclei, even the well established nuclear models (like the shell model) start to have a rather limited predictive power and the evolution of the shell structure is less understood. Experimentally, the signature of magic numbers appears as discontinuities in some observables for certain numbers of protons or neutrons. However, every discontinuity cannot be interpreted as a signature of magic numbers and its absence does not always mean that the shell is not closed. As shown for the two neutron separation energy (mass derivative), the absence of the signature may be caused by the collective correlations[1] [BBH08]: *Looking at the shell closures where the S_{2q} values exhibit discontinuities, static mean-field deformations and dynamical correlations decrease systematically the amplitude of these gaps, and reduce them far from stability. Both effects are not related to a reduction of the spherical shell structure, rather both underline the importance of fluctuations around single mean-field configurations for a high-precision description of nuclear masses.*

If there are no collective correlations then the shell closure could be directly seen from the mass surface or from the two neutron separation energies. In the opposite case, and since the binding energy contains all information including shell effects, one needs other observables to have a complete picture of the evolution of spherical shell structure. In the latter case, it is difficult to extract the shell effects from the mass filters but one can extract valuable informations about these collective effects such as deformations and/or more subtle effect as the pairing.

Thus, one should be careful in the interpretation of the mass filters in term of shell structure since these include other effects which can coat the single particle shell.

[1] Energies that the system can gain via the collective behavior of its nucleons, for example via deformations.

Some of the shell closures established from studies on stable nuclides seem to weaken or even disappear as one goes away from stability. A paramount example is $N = 20$ [Thi+75; Dét+79] and the famous 'island of inversion', where it was noted that ^{31}Na and ^{32}Na were considerably more bound than predicted for a closed $N = 20$ shell. It was suggested that this might be due to deformation, which was supported by Hartree-Fock calculations [Cam+75] which could reproduce ^{31,32}Na binding energies only when promotion of neutrons from the $d_{3/2}$ to the $f_{7/2}$ intruder orbit was allowed, leading to large deformations. The occupation of intruder orbits was very surprising, since $N = 20$ was believed to be a magic number and no excitations across the shell gap should be present at low excitation energies. Later, mass measurements were extended to Mg isotopes and it was found that both ^{31}Mg and ^{32}Mg were also more bound than expected. At the same time 'new' magic numbers appear as $N = 16$ [Oza+00] and $N = 32$ [Lid+04].

In this work, the case of $N = 40$, thought to be a new magic number, will be studied from the most exotic nuclides in this region, the Mn isotopes.

6.1.1. What do we know about N = 40 around Z = 28?

The region around $N = 40$ and $Z = 28$ has being extensively studied during the last two decades. Several experimental and theoretical studies around $Z \approx 28$ showed that $N = 40$ may be a closed shell and ^{68}Ni to be doubly magic. In the following, some of the key observables and the most important experimental results will be discussed in the light of $N = 40$ magicity.

Energies of the excited states 2^+, 4^+ and the reduced transition probability $B(E2)$
The energies of the first excited state 2^+ and the corresponding $B(E2)$ values in even-even nuclei are considered as indirect measurements of the magicity. Magic spherical nuclides have the first excited state 2^+ at high energy since they are difficult to excite and their reduced transition probabilities $B(E2; 2^+ \rightarrow 0^+)$ are very small.

The first suggestion of the shell closure at $N = 40$ was proposed by Bernas *et al.* [Ber+82] from the measurement of the ^{68}Ni first excited state. It was followed by another measurement [Bro+95] where the authors confirm the sub-shell closure at $N = 40$ from the high-lying 2^+ in ^{68}Ni. Later the reduced transition probability of the same nuclide was measured by Sorlin *et al.* [Sor+02], $B(E2; 2^+ \rightarrow 0^+) = 3.2(7)$ Wu. This value is the smallest $B(E2)$ values of all semi-magic nuclides. As shown in Figure 6.1, the energies of the first excited state 2^+ show an increase at $N = 40$ for the Ni isotopes but a drastic decrease for Fe and Cr isotopes. The $B(E2)$ values are the smallest for Ni at $N = 40$ isotopes but show no decrease while approaching $N = 40$ for other nuclei around Ni.

However, from these two observables it is not straightforward to argue for the shell closure at $N = 40$. Langanke *et al.* [Lan+03] suggested that the observed $B(E2)$ values of ^{68}Ni is smaller than in ^{56}Ni because it is more favorable in ^{68}Ni to excite the pair of neutrons into the $g_{9/2}$ orbital than to excite a single proton across the magic $Z = 28$ gap. Thus, a small $B(E2)$ value is not an argument for shell closure at $N = 40$. It only proves that the 2^+ state is dominated by neutron excitations.

It is also interesting to look at the energies of the second excited state 4^+. The ratio between the energies of the second and the first excited states can give an indication

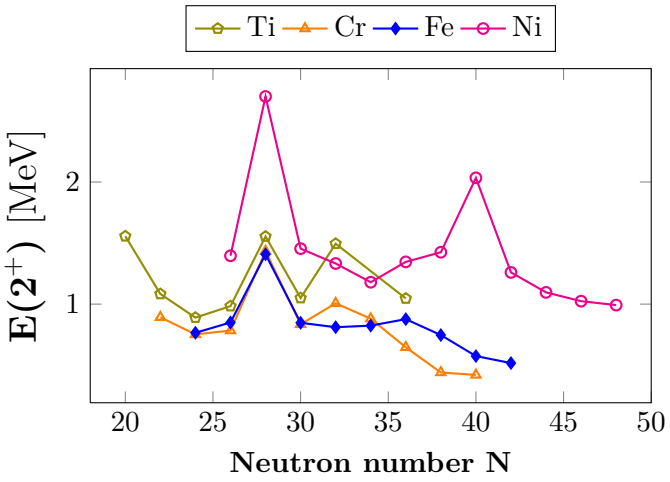

Figure 6.1.: Energies of the first excited 2^+ states for the even-even nuclei in the region around $N = 40$ and $Z = 28$, versus neutron number (Data from [Tul10]).

on the nucleus shape excitation modes ($E(4^+)/E(2^+) \leq 2$ spherical-vibrational, ~ 2.5 transitional, ~ 3.3 rigid-rotor). The ratios of experimental values in this region are plotted in Figure 6.2. At $N = 28$ for all nuclei, the ratio drops to very low values–clear signature of sphericity of these nuclei, which can be also interpreted as a shell closure. However, at $N = 40$ only the Ni ratio goes down, in contrast to the behavior of Fe and Cr isotopes. It has been shown that the behavior of the latter isotopes is evidence of the increase of collectivity and significant structural change [Adr+08; Gad+10], explained by the presence of a neutron intruder orbital ($g_{9/2}$). This onset of collectivity below ^{68}Ni was even compared [Lju+10] to the behavior in the region of the 'island of inversion' around ^{32}Mg.

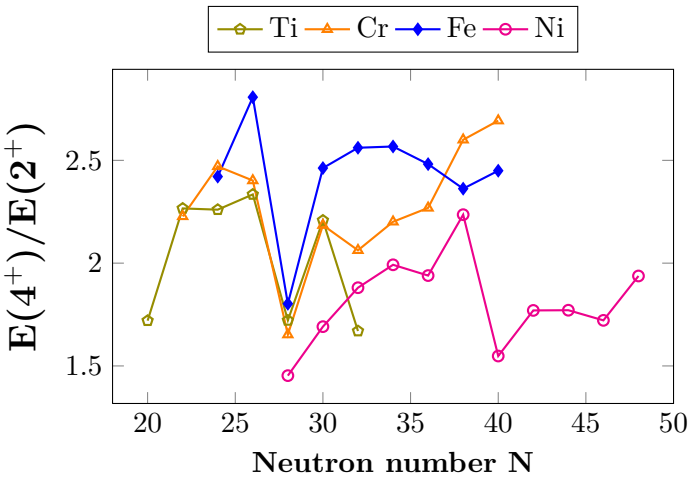

Figure 6.2.: The ratio of the first 4^+ and the first 2^+ excited states E(4^+)/E(2^+) with the neutron number for the even-even nuclei in the region around $N = 40$ and $Z = 28$ (Data from [Tul10]).

β-decay and half-lives The decay mode of radioactive nuclei is an important piece of information and plays a key role in definition of their half-lives. It is also directly related to the transition between daughter and mother and can provide crucial information about the shell structure. Below ^{68}Ni the β-decay is dominated by the allowed $\nu f_{5/2} \rightarrow \pi f_{7/2}$ Gamow-Teller transition[2], whose strength (lifetime) depends on the occupation of these orbitals in the mother and daughter nuclei (see Figure 6.3).

The β-decay of the neutron-rich Mn isotopes were studied by Hannawald *et al.* [Han+99] and from the $2^+ \rightarrow 0^+$ transition in ^{66}Fe, it was shown that these nuclei are deformed. This was explained by strong attraction between protons in the orbital $f_{7/2}$ and the neutrons in the orbital $g_{5/2}$ which leads to a lowering of the latter.

Later, Gaudefroy *et al.* [Gau+05] studied the β-decay of a large range of isotopes in the $N = 40$ region: ^{57,58}Sc, $^{58-60}$Ti, $^{60-62}$V, $^{62-66}$Cr, $^{64-68}$Mn, $^{67-70}$Fe and $^{69-71}$Co. The experimental half-lives were found to be much longer than the calculated ones when approaching $N = 40$. The interpretation of these results is that the pairing effect shifts neutrons from the $\nu f_{5/2}$ up to the $\nu g_{9/2}$ shell already before reaching $N = 40$ which reduces (increases) the Gamow-Teller strength (life-time). The occupation of the $\nu g_{9/2}$ shell by pair scattering depends strongly on the energy difference between the single particle $\nu f_{5/2}$ and $\nu g_{9/2}$ orbitals. This spacing is very sensitive to the proton-neutron interaction ($\pi f_{7/2}$-$\nu f_{5/2}$) which decreases the $\nu f_{5/2}$ orbital by some MeV when going from the $N = 40$ Ca to the Ni isotones. Gaudefroy *et al.* conclude that the studies of the proton-neutron interaction and the occupation of the $\nu g_{9/2}$ were not possible because of the lack of the binding energies data in this region.

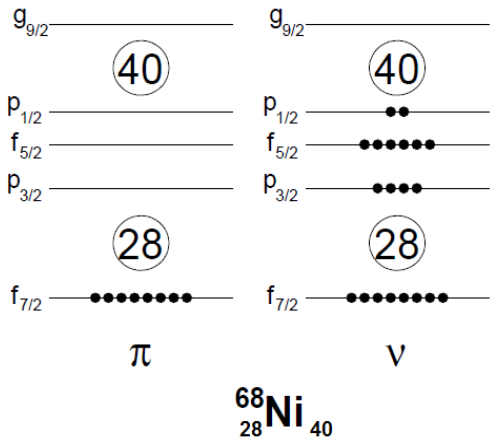

Figure 6.3.: The occupation of proton π and neutron ν shell model orbitals in the ^{68}Ni ground state.

Isomerism The appearance of long-lived exited states in the vicinity of closed shells is one of the features very well explained by the shell model. The "island of isomers" around $N \approx 50, 40 < Z < 50$ is a very good example to illustrate this feature. Two types

[2] In β-decay, the frequently observed transitions which populate the daughter states are the Gamow-Teller type. These transitions are called 'allowed' if there is no parity change and the daughter spin changes by ± 1.

of isomers are present in this region: the *seniority isomers* (coupling several nucleons to different spin values for the same occupied orbits) and the *single particle isomers* (excitation of one nucleon).

The *seniority isomers* are due to the coupling of the protons in the $g_{9/2}$ orbital: the configurations $\pi g_{9/2}^n$, n being the seniority, *i.e* the number of nucleons not coupled to spin 0 which leads to an 8^+ isomer in ^{92}Mo, ^{94}Ru, ^{96}Pd and ^{98}Cd [Grz+95] and also in ^{68}Ni [Ish+02], ^{70}Ni [Grz+98] and ^{78}Zn [Dau+00]. The 8^+ isomer with the configuration $\nu g_{9/2}^{-2}$ in ^{78}Zn confirms the shell closure at $N = 50$ and suggests an 8^+ isomer in ^{76}Ni [GL01].

The *single particle isomers* are due to the difference between the spin of the isomeric state and the state to which it decays. In the region around $N = 50$ these isomers are due to large spin difference with the neighboring $\pi p_{1/2}$ orbital.

Since the neutron-rich region $Z \approx 28, 40 < N < 50$ is the "valence mirror" region[3] of the $N \approx 50, 40 < Z < 50$ region, the same arguments could be used and the same behavior is expected with the role of protons and neutrons outside the closed shell exchanged.

Indeed, many isomers were observed in this region: ^{67}Zn, ^{67}Ni, ^{69}Cu and many others listed in Grzywacz *et al.* [Grz+98]. Also Gaudefroy *et al.* [Gau05] discovered many isomers very close to $N = 40$: ^{67}Fe and ^{64,66}Mn, due to the presence of the $g_{9/2}$ orbital and its proximity to the fp shell. Recently a discovery of a single low-energy proton-isomer (caused by a proton intruder state) in ^{67}Co was reported for the first time by Pauwels *et al.* [Pau+08]. Regarding the question of the $N = 40$ shell closure, they conclude: *This newly established isomer has been interpreted as a prolate* $(1/2^-)$ *proton intruder state coexisting with a spherical* $(7/2^-)$ *ground state. Taking away only one proton from* ^{68}*Ni already induces the obliteration of the* $N = 40$ *sub-shell gap and sets in a region of deformation below* $Z = 28$. A summary of some isomers around $N = 40$ is shown in Figure 6.4.

Atomic masses It is known that the mass derivative, the two neutron separation energy, drops considerably at closed shell for example at $N = 28$ and $N = 50$. This drop defines the shell gap at these magic numbers. The mass surface shows a rather smooth behavior in the $N = 40$ region from mass measurements of Ni, Cu and Ga isotopes [Gu07] and also from the recent measurements of the Fe isotopes [Fer+10]. This is in contrast with other observables suggesting the ^{68}Ni magicity. However, it confirms the collective behavior of other $N = 40$ isotones. These unexpected and conflicting experimental results are very interesting and call for further experimental and theoretical studies to converge to a better understanding of the shell evolution in this region.

In summary, the (sub)shell closure at $N = 40$ is believed to be very weak due to the deformations, shapes coexistence and behavior of some orbitals when going away from $Z = 28$. The proton-neutron interaction plays an important role in this region but the details of its role are still not completely understood.

[3] Valence nucleons are the free nucleons or "active nucleons" which determine the properties of the nucleus

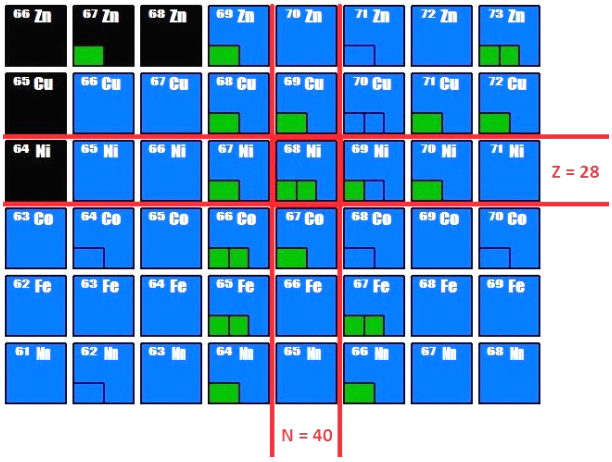

Figure 6.4.: $N = 40$ region: (in black) stable nuclides, (in blue) nuclides decaying by β^-. The isomers are represented by small green (internal transition) or blue (β^- decay) boxes inside the nuclides where these isomers are present. Picture from [Aud03] based on the updated version of [Aud10] where most of the new isomers are included.

The masses of $^{58-66}$Mn, presented in this work, provide valuable input to the studies of the region around $N = 40$ and $Z = 28$ since these are the most exotic masses yet measured.

6.1.2. The new mass surface

6.1.2.1. The two neutron separation energy S_{2n}

The two neutron separation energy or the first mass derivative is the most remarkable way in which shell structure manifests itself:

$$S_{2n}(N, Z) = B(N, Z) - B(N - 2, Z) \tag{6.1}$$

where $B(N, Z)$ is the binding energy of the nucleus with proton number Z and neutron number N. The two neutron separation energy generally decreases with increasing N, reflecting the shell filling (a linear behavior is observed between closed shells). In Figure 6.5, the new S_{2n} values are plotted between the two well-known closed shells $N = 28$ and $N = 50$. No drop is seen from these values at $N = 40$ for the Mn isotope chain which means that there is no hint of shell closure directly from masses. In the isotopic chains $Z = 32 - 36$ (Ge-Kr), the expected linear trend is observed. The linear fit, shown in the top figure as dashed lines, fails when going for lighter (and more exotic) masses starting from the Ga isotopic chain. Recent nuclear spins and magnetic moments measurements of Cu and Ga isotopes [Fla+09; Che+10] reveal a sudden change in structure in this region. The quadratic fit seems to be more appropriate for this mass region (Figure 6.5 bottom). This quadratic behavior is more pronounced for lighter masses below nickel. A closer look at the Mn isotope chain shows that at $N = 37$ the S_{2n} values are increasing slowly with N.

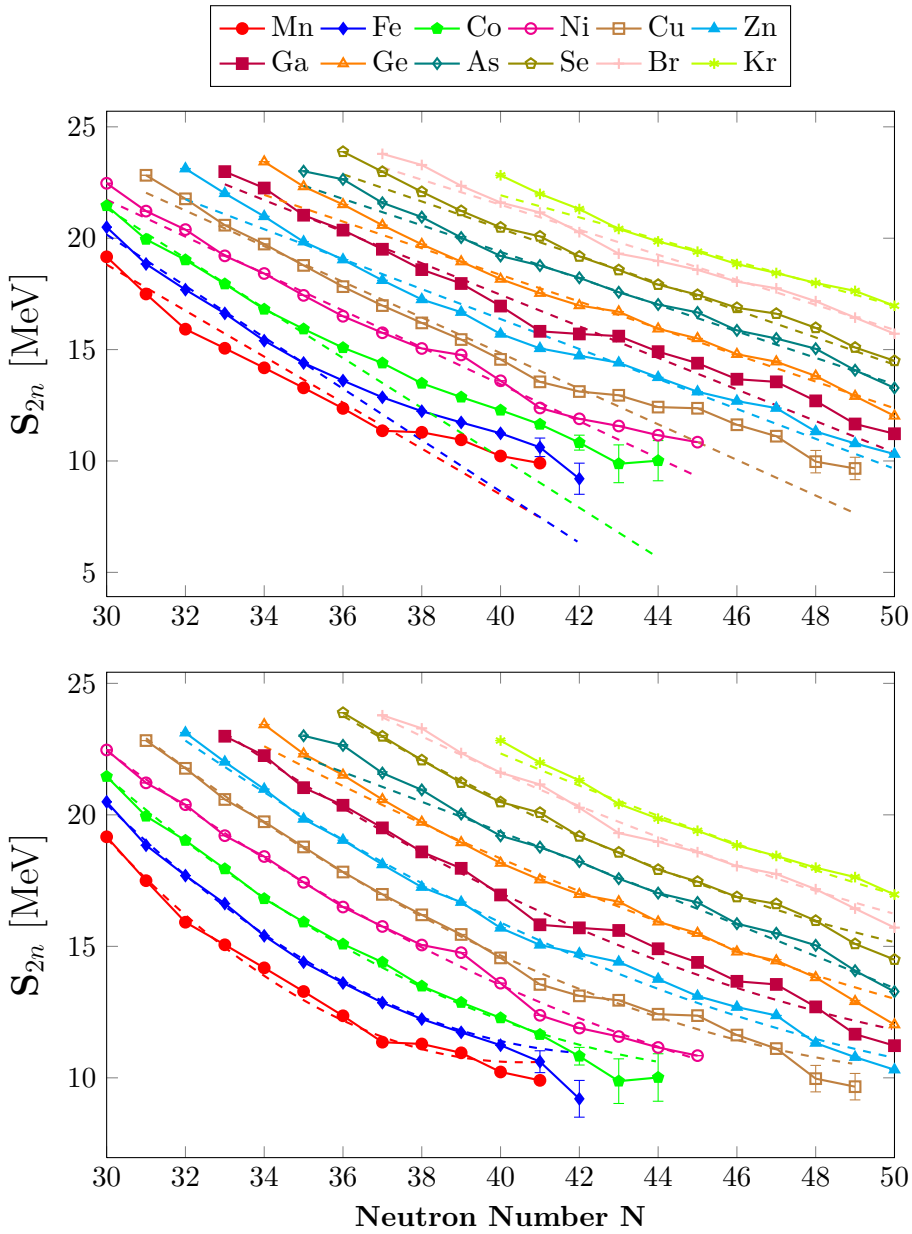

Figure 6.5.: Two neutron separation energy plotted with neutron number. (Top) two neutron separation energy fitted with a linear fit shown as dashed lines. (Bottom) two neutron separation energy fitted with a quadratic fit shown as dashed lines.

Some mass model predictions First the measured binding energies are compared to the prediction of the existing models. By the diversity of all models available nowadays, it would be extremely time-consuming to compare the data with all of them. Therefore, only a few models are chosen for their capability of ground state masses prediction: microscopic model Hartree-Fock-Bogolioubov using Skyrme force HFB-14 [GSP07], microscopic-macroscopic finite-range droplet model (FRDM) [Mol+95] and finally a more fundamental approach than the microscopic-macroscopic method: the Duflo-Zuker

mass formula [DZ95]. Usually, the root-mean-square deviation method is used when testing the prediction power of the model:

$$\sigma_{rms} = \sqrt{\frac{1}{N}\sum_{i=1}^{N}(m_{exp}^{i} - m_{th}^{i})^2} \tag{6.2}$$

where N is the number of masses compared and m_{exp}, m_{th} are the experimental and theoretical mass excesses (or binding energies) respectively. In Table 6.1, the σ_{rms} is calculated for each model between $N = 28$ and $N = 50$ for Ni, Co, Fe and Mn isotopes. The theoretical predictions are compared to the published mass excesses in AME2003 and to the new mass table AME2010 after including the new data on the Mn and Fe isotopes from ISOLTRAP (Table 5.2 shows the ISOLTRAP contribution to AME2010 in this region). In AME2010 other recent data are included for Fe, Co, Ni, Cu, Zn, Ga isotopic chains: ISOLTRAP [Gu07; Bar+08], Oak Ridge [Hau+06], JYFLTRAP [Rah+07; Hak+08], LEBIT [Blo+08; Fer+10].

From a general view one can see that the Dulfo-Zuker mass formula gives the best prediction. While comparing the σ_{rms} between AME2003 and AME2010, the HFB-14 improved almost by a factor of two compared to Duflo-Zuker (last line in Table 6.1). The improvement and prediction of the finite-range droplet model is intermediate between the two latter models. One can observe that the improvement is larger for more microscopic models (HFB-14 is a microscopic model and FRDM has some microscopic corrections) but the prediction is worse. It is very difficult to compare the three models since they don't have the same number of parameters: 41 for FRDM, 28 for Duflo-Zuker and 14 for HFB-14. One has to expect the best prediction with the model which has the largest number of parameters. It is interesting to note that this is not the case, the Duflo-Zuker formula gives better predictions than FRDM even with less parameters. However, the microscopic models such as the HFB-14 model gives more informations (*e.g.* wave function, half-lives, deformation parameters) while the Duflo-Zuker mass formula gives only the binding energies.

The difference between the experimental binding energies and the models prediction can give a valuable information about the missing information in the models (see chapter 2) but this require a deep understanding of the models. These differences are plotted for each model in Figure 6.6. The difference shown in these plots is the difference between absolute binding energies. Thus, if the difference $(m_{exp} - m_{th})$ is positive then the model predicts the nucleus to be less bound and *vice versa*.

Near the closed shell $N = 28$, in FRDM and the Duflo Zuker model the masses are well predicted. When going to neutron-rich nuclei the FRDM model starts to diverge from the experimental data while Duflo Zuker gives better predictions. Only the predicted mass of $^{66}Mn_{41}$ diverges. The same nuclide is also expected to be more bound than all heavier isotopes (Fe, Co, Ni isotopes) in the FRDM model. This odd behavior of the Mn isotopes could be attributed to a sudden change of the binding energies at lighter masses which is not taken into account in both models. Unfortunately, no Cr masses are available with sufficient precision to confirm if this behavior is specific to the Mn isotopes or persists for even lighter masses. It is important to note here that Mn isotopes are the most exotic in this region. In the HFB-14 model, in contradiction to FRDM and

DZ models, the Mn isotopes are expected to be less bound but they show also a different behavior compared to heavier masses. In this model, the deviation from experimental data is very large compared to the other models. However, the Mn isotope masses are the best prediction of this model compared to Fe, Co and Ni masses.

Regardless of the expectation of the binding energies in different approaches, the new Mn masses show in general a different trend compared to heavier isotopic chains which could be attributed to a sudden structural change for lighter masses, not taken into account in any of the presented models. A closer look to these models and more measurements on the neutron-rich Chromium isotopes are necessary to confirm this observation.

Table 6.1.: The standard deviation σ_{rms} in MeV for different mass models. The models are compared to the mass table AME2010 and AME2003 for the region $Z = 25 - 28$ and $N > 28$. The last line is the mean difference between AME2003 and AME2010 for each model for the whole region.

Mass table	**Nuclide**	**FRDM**	**HFB-14**	**DZ**
AME2003	Mn	0.452	0.939	0.403
AME2010	Mn	0.348	0.867	0.423
AME2003	Fe	1.008	1.146	0.438
AME2010	Fe	0.899	1.113	0.366
AME2003	Co	0.877	1.778	0.419
AME2010	Co	0.807	1.743	0.310
AME2003	Ni	0.649	1.422	0.289
AME2010	Ni	0.560	1.158	0.269
Improvement	Mn,Fe,Co,Ni	0.071	0.101	0.055

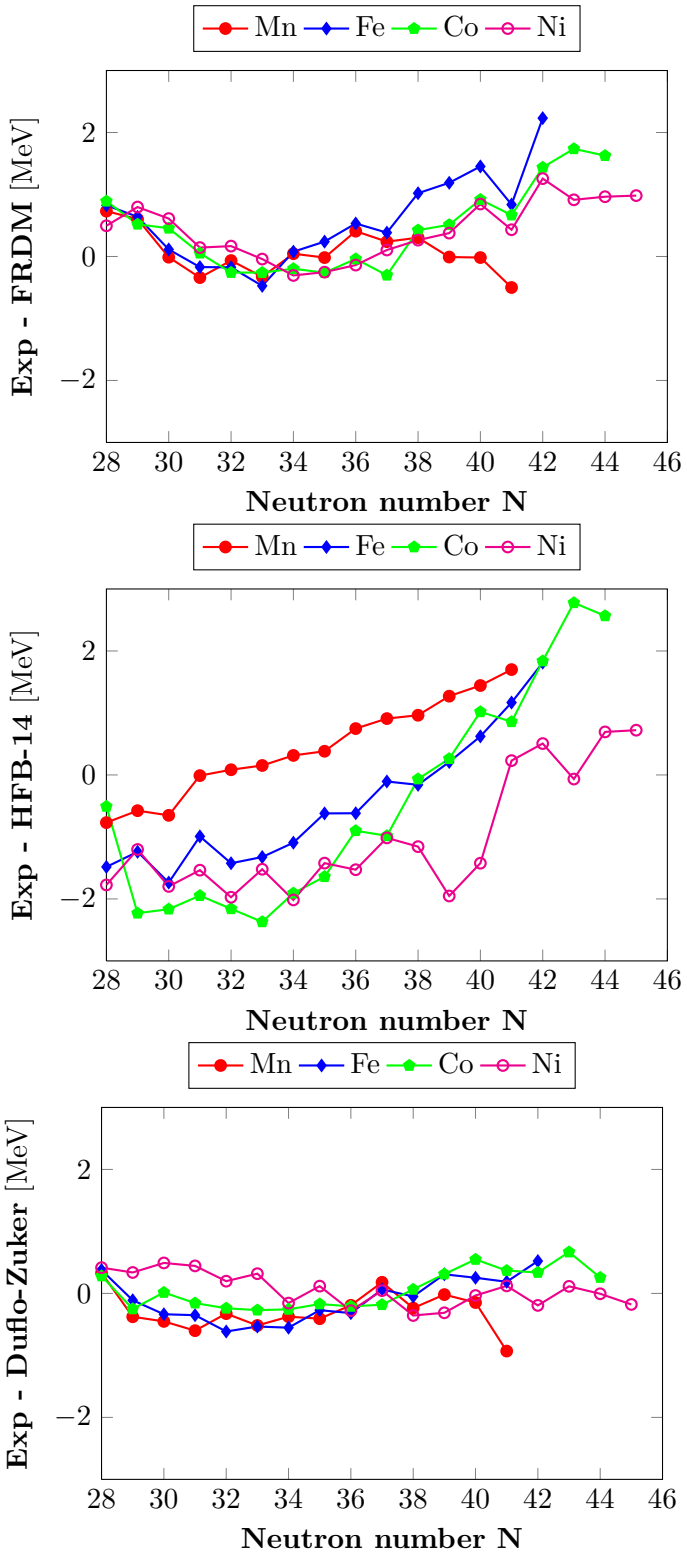

Figure 6.6.: Difference between binding energies calculated in the FRDM, HFB-14 and Duflo-Zuker models and measured binding energies.

Figure 6.7, Figure 6.8 and Figure 6.9 plot the experimental two neutron separation energies in comparison with the three models (FRDM, HFB-14 and Duflo-Zuker). The predicted S_{2n} values in the Duflo-Zuker model show a small drop at $N = 40$, only the $^{66}Mn_{41}$ deviates strongly from the general smooth trend. The two other models do not predict any shell closure at $N = 40$. However, the predicted mass surface is straggling notably for the HFB-14 model.

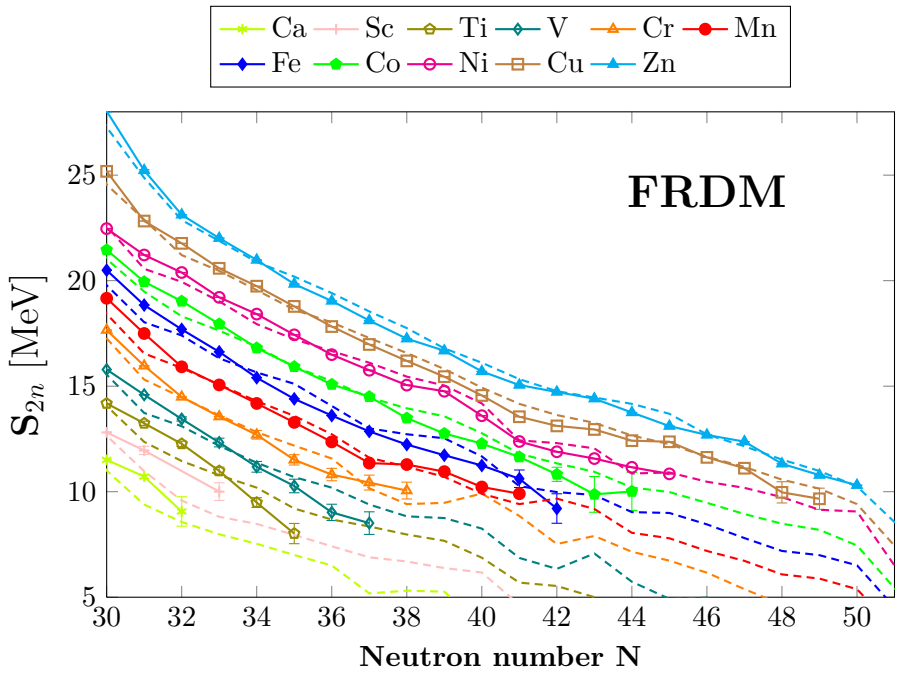

Figure 6.7.: Two neutron separation energy calculated from mass measurements (solid lines) compared to the two neutron separation energy calculated in the FRDM model (dashed lines) in the region from Ca to Zn.

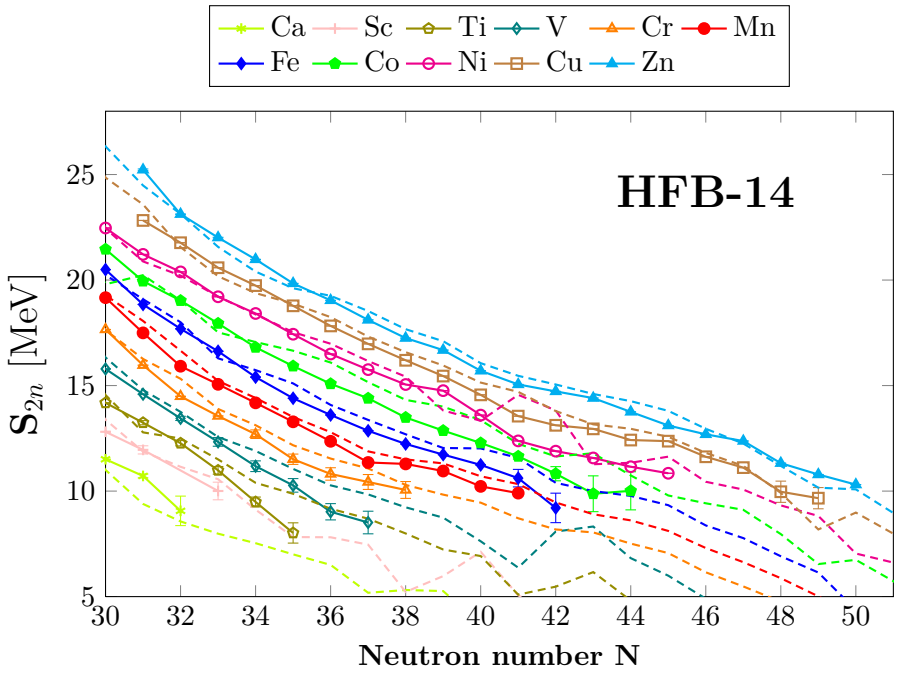

Figure 6.8.: Two neutron separation energy calculated from mass measurements (solid lines) compared to the two neutron separation energy calculated in the HFB-14 model (dashed lines) in the region from Ca to Zn.

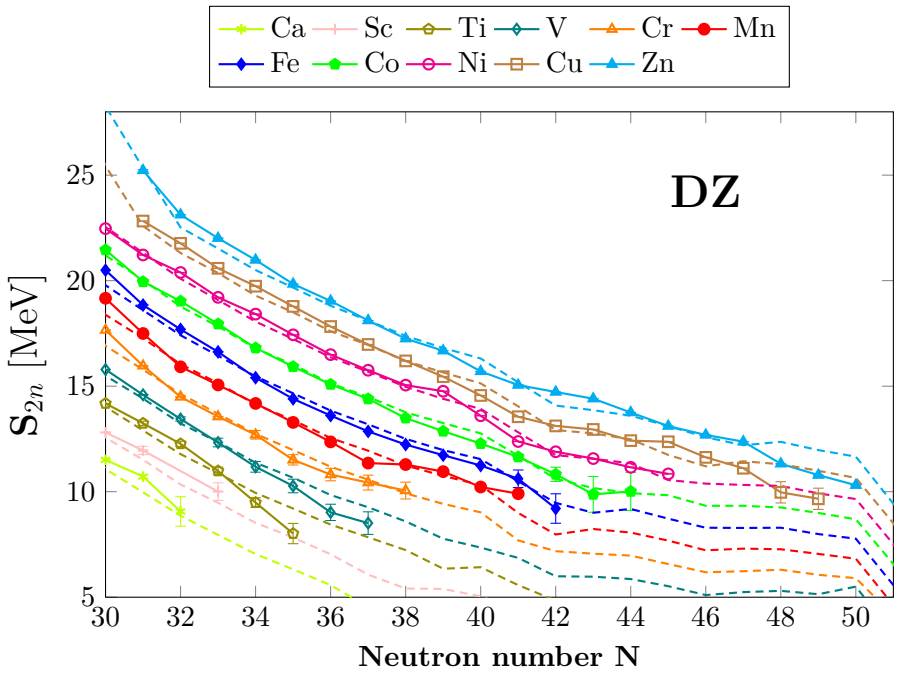

Figure 6.9.: Two neutron separation energy calculated from mass measurements (solid lines) compared to the two neutron separation energy calculated in the Duflo-Zuker model (dashed lines) in the region from Ca to Zn.

Beyond the mean-field One of the most promising models for the ground states description beyond the mean-field is the Generator Coordinate Method (GCM). This method is used to correct the symmetry breaking induced by non-spherical HFB and correct the value of the binding energy by taking into account correlation terms due to rotation and vibration which is not estimated with pure HFB calculation. Recently, the systematics of the ground-state quadrupole correlations of binding energies were discussed by Bender *et al.* [BBH06]. The authors calculated the correlated $J = 0$ ground state by means of the angular-moment and particle-number projected generator coordinate method (GCM), using the axial, parity and time-reversal symmetries. This calculation was performed within the framework of a non-relativistic self-consistent mean-field model by using the Skyrme interaction and a density-dependent pairing force to generate the mean-field configurations and to mix them. By using this method and from the calculation of the ground state masses, the authors successfully show how the shell closures are affected by these correlations [BBH08].

In Figure 6.10, are shown the spherical mean-field predictions as described in [BBH08](top) and the angular-momentum projected generator coordinate method ($J = 0$ GCM) (bottom). Unfortunately, these calculations could be done only for even-even nuclei and no more calculations are available for neutron-rich lighter masses apart from what is shown in the figure. In the spherical mean-field, $N = 40$ behaves like a closed shell (seen from the sudden drop in S_{2n} values), but introducing the rotational and vibrational correlations makes this effect vanish and a smooth behavior is observed for this region, which is in a good agreement with the experimental data. It is interesting to note here the reduction of the mass surface (lower S_{2n} values) by introducing these correlations which means that these nuclei are less bound because of the onset of collectivity in this region. By using the $J = 0$ GCM method, the Fe S_{2n} values are reduced while the Cr S_{2n} values stay the same. The behavior of lighter and heavier masses is different as well when comparing the experimental data and the model predictions. It will be interesting to see what are the predictions of this realistic model for more neutron-rich nuclei and its extension to even-odd and odd-odd masses.

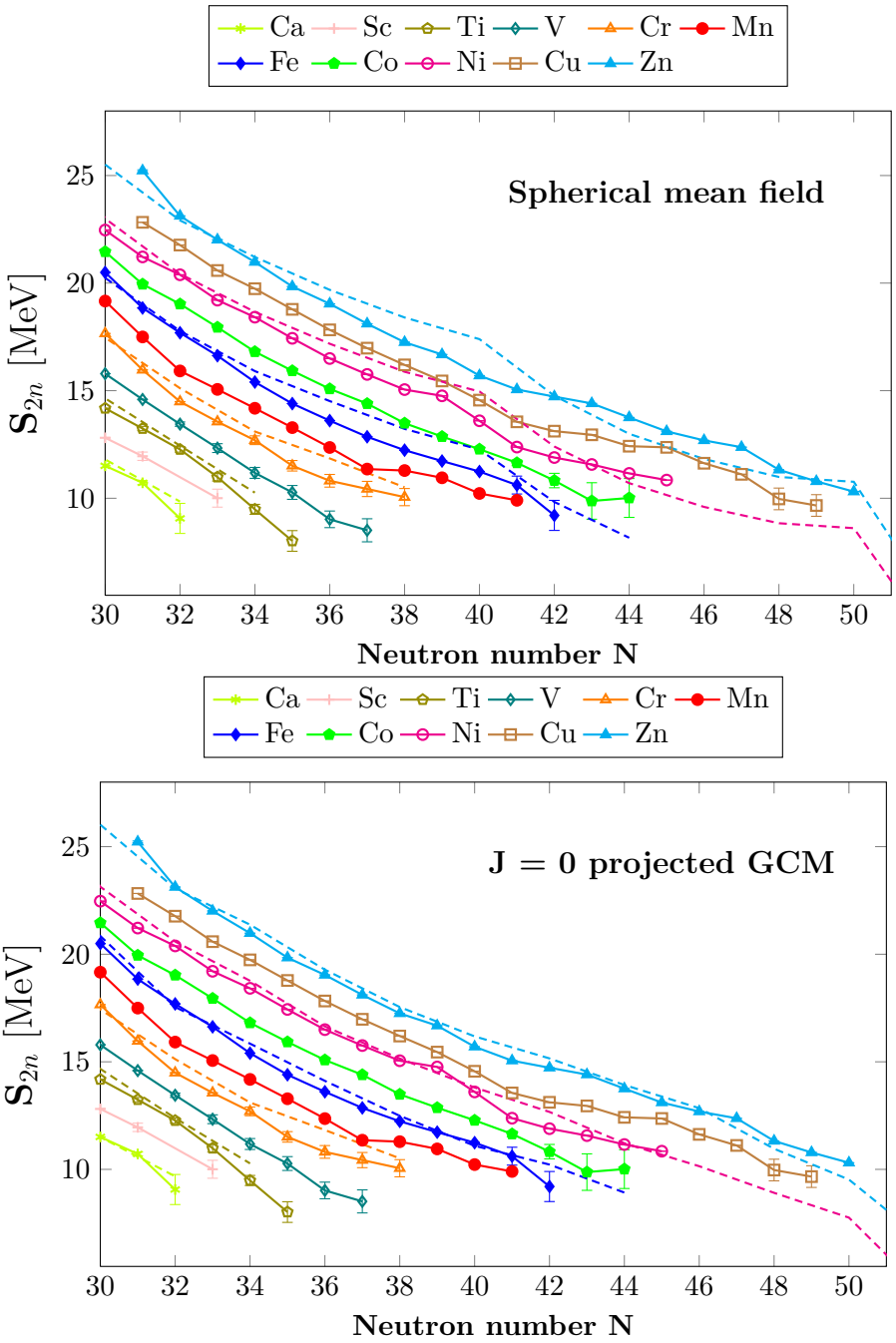

Figure 6.10.: Two neutron separation energy calculated from mass measurement (solid lines) compared to the two neutron separation energy calculated in the spherical mean field in the top plot (dashed lines calculated only for even-even nuclides). In the bottom is plotted the two neutron separation energy calculated from ground state masses obtained after configuration mixing by the generator coordinate method of $J = 0$ projected axial quadrupole ($J = 0$ GCM) [BBH08].

6.1.2.2. The "empirical" shell gap

The shell gap is defined as the distance between shells in the single particle model. In the case of $N = 40$ this would be the distance between pf shell and g shell (see Figure 6.3). The "empirical" shell gap, in addition to this single particle shell gap, includes many-body effects since it is calculated from the experimental binding energies:

$$\Delta_N(N,Z) = S_{2n}(N,Z) - S_{2n}(N+2,Z) \tag{6.3}$$

With this second mass derivative, one can quantify the strength of the shell closure. In the case of the well established magic numbers, the "empirical" shell gap is around 4 MeV as shown in Figure 6.11. For semi-magic nuclei this gap is around 5.5 MeV and for $N = Z$ nuclei this gap can reach 9 MeV (for example at $N, Z = 16$ or at $N, Z = 28$)

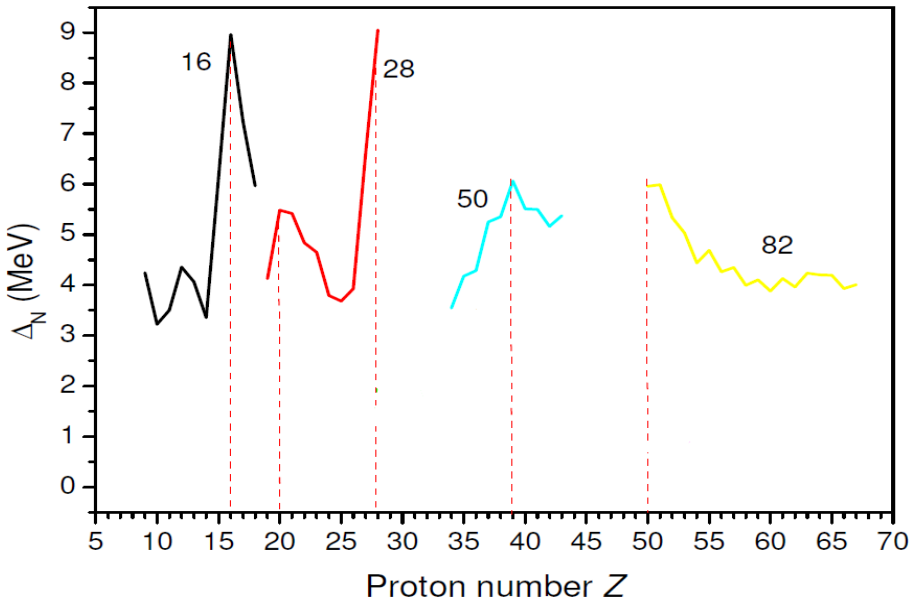

Figure 6.11.: Empirical shell gap as a function of the proton number Z for different neutron magic numbers.

Figure 6.12 plots this "empirical" shell gap for $N = 40$ as a function of proton number. One can see that the shell gap in the isotonic chain varies between 1 and 2 MeV which is very small to consider $N = 40$ as magic number. Following a similar argument used by Bender *et al.* [BBH08], the shell gap could be also seen by subtracting the linear trend from the S_{2n} and plotting the two isotonic chains N and $N+2$. Figure 6.13 shows $S_{2n} - F(Z)$ where the $F(Z)$ is a linear function representing the linear trend of the S_{2n} with Z. The distance between $N = 40$ and $N = 42$ is increasing when approaching $Z = 40$ and $Z = 28$ and is very small in between. This spacing has a maximum values around 0.5 MeV which is still very small compared to the spacing between $N = 50$ and $N = 52$ ($\sim 2MeV$) shown in Figure 2 of [BBH08]. Thus, $N = 40$ cannot be considered as magic due to this small values of the shell gap at this neutron number. In the same figure are shown the theoretical predictions of the spherical mean field and the deformed one with $J = 0$ GCM. One can see that the spherical shell gap is reduced when there is

collective behavior which is in relatively good agreement of the experimental data. Also this model reproduced the opening of the gap when approaching $Z = 40$.

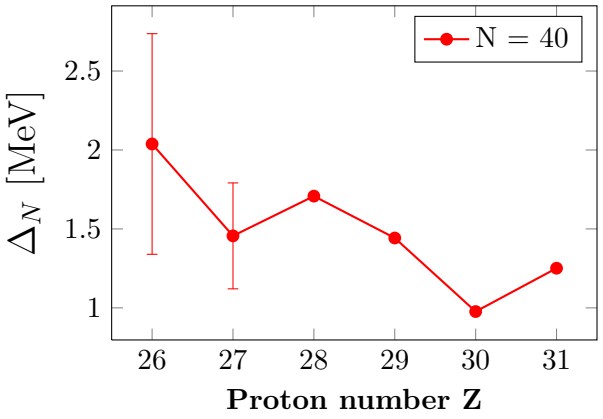

Figure 6.12.: The "empirical" shell gap at $N = 40$ plotted as a function of the proton number.

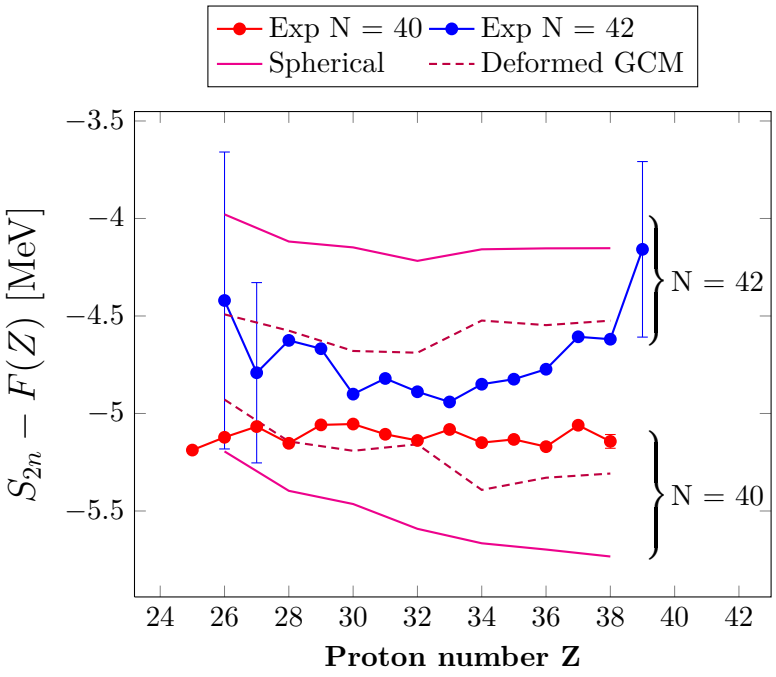

Figure 6.13.: The two neutron separation energy with subtraction of the linear trend plotted as a function of the proton number and for two chains of isotones with $N = 40$ and $N = 42$. Solid lines correspond to shell gaps calculated from spherical mean field and the dashed ones are calculated from the general coordinate method of $J = 0$ projected axial quadrupole ($J = 0$ GCM) [BBH08] (only for even-even nuclei).

6.1.2.3. Pairing energy

From mass derivatives, another important indicator of shell effects can be extracted; the pairing energy which is defined as:

$$\Delta_4(N,Z) = \Delta_{nn}(N,Z) - \left(\frac{1-(-1)^Z}{2}\right)\Delta_{np}(N,Z) \tag{6.4}$$

$$= \frac{(-1)^{N+1}}{4}\left[S_n(N+1,Z) - 2S_n(N,Z) + S_n(N-1,Z)\right] \tag{6.5}$$

where S_n is the neutron separation energy and Δ_{nn}, Δ_{np} are the pairing gap energies:

$$\Delta_{nn}(N,Z) = S_{2n}(N,Z) - S_{2n}(N-2,Z) \tag{6.6}$$

$$\Delta_{np}(N,Z) = S_{2n}(N,Z) - S_{2n}(N,Z-2) \tag{6.7}$$

These energies are represented in Figure 6.14, where a hypothetical energy zero represents a nuclide with no pairing among the last nucleons. One can see it also as the internal energies that the nucleus gains by pairing its nucleons in different ways. At a closed shell

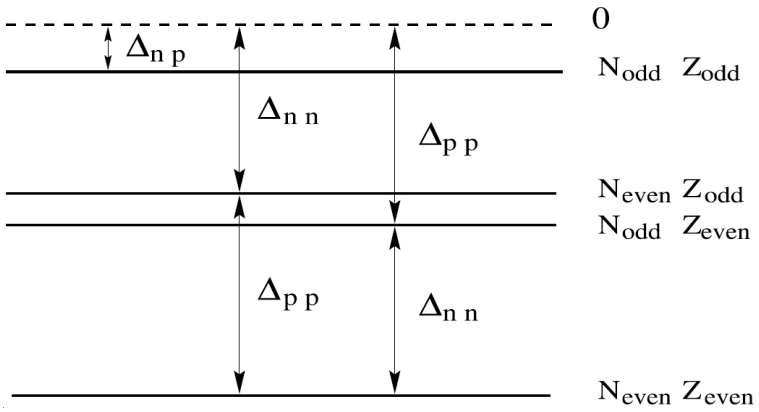

Figure 6.14.: Scheme representing the pairing energies for the four type of nuclei (even-even, even-odd, odd-even, odd-odd). The zero energy is a purely hypothetical one for no pairing at all among the last nucleons.

the pairing energy should increase suddenly and reach its maximum after the closed shell, indicating the large energy needed to break this pair. From Equation 6.4, the pairing energy is then $2\Delta_{nn}$ for Z-even and $\Delta_{nn} - \Delta_{np}$ for Z-odd. Thus, the pairing energy curve of Z-even indicates the n-n pairing and the distance between the neighbor Z-even and Z-odd curves indicates the p-n pairing. For this purpose, in Figure 6.15 are shown experimental values of the pairing energy for the Z-odd (Mn, Co, Cu) with their Z-even neighbors (Fe, Ni, Zn). Unfortunately, the Cr masses are missing to complete the first plot of this figure. From the new Mn masses it is difficult to conclude anything about $N = 40$ since the ^{67,68}Mn S_n values are needed to see the behavior of the pairing energy at $N = 41, 42$ (see Equation 6.5). The Ni and Cu pairing energies show a small increase but not big enough to consider $N = 40$ as closed shell. However, this plots show a large proton-neutron interaction in this region between ~ 0.2 MeV and ~ 0.5 MeV. In

the Mn isotopes the pairing energy drops at $N = 32$ and goes up at $N = 37$. From the orbital occupation point of view, this correspond exactly to the neutron filling of the $\nu f_{5/2}$ and the protons and neutrons are in the same shell (large overlap between their wave-functions). As it was mentioned in previous studies (see subsection 6.1.1), the interaction between the $\nu f_{5/2}$ and $\pi f_{7/2}$ is expected to be very strong and is responsible for the lowering of the $\nu g_{9/2}$ and its occupation. Indeed, from the new masses this interaction is very strong and estimated to be around 0.5 MeV. If the reasoning in terms of orbital occupation is correct, one would expected a sudden change at $N = 38$ where this orbital is closed and not at $N = 37$. Examining the manganese S_n values plotted versus N in Figure 6.16, the distance between the odd and even Mn isotopes (by definition correspond to the pairing energy) from $N = 32$ to $N = 36$ is constant and is the smallest. At $N = 37$ this distance is larger because of the increase in the neutron separation energy of $N = 38$. There might be two explanations of this anomaly: either the p-n interaction is weaker when approaching the closed $\nu f_{5/2}$-shell or the neutrons start to occupy the higher shells already at $N = 38$. A similar argument could be used for Co since the proton orbital $\pi f_{7/2}$ is not closed ($Z = 27$). The pairing energies in Co isotopes are higher than the Mn pairing energies, either due to low p-n interaction or high p-p pairing, or both. It could be that by approaching the closed $\pi f_{7/2}$-shell the proton orbital makes the p-n interaction weaker, which would confirm the first hypothesis of the anomaly observed at $N = 37$. However, the second hypothesis cannot be excluded and the occupation of higher orbitals ($\nu g_{9/2}$) in the Mn isotopes is in good agreement with the long half-lives observed by Gaudefroy *et al.* [Gau05][4].

In the Co isotopes, the pairing energy decreases slowly when approaching $N = 40$ indicating the slow increase of the p-n interaction. This might reveal more complex configuration mixing as suggested by the discovery of an isomeric state in $^{67}Co_{40}$ due to a proton intruder state. For higher Z-odd mass (Cu isotopes) the pairing energy is higher, which reveals a even lower p-n interaction since the protons and neutrons do not occupy the same orbitals and the spin is lower in the *p*-shell. The drop at $N = 30$ is very specific to the $N = Z$ Z-odd nuclei due to the symmetry energy between N and Z (the so-called "Wigner term") which is not the case for Z-even nuclei where the high pairing energy is dominating.

For the Z-even nuclei in this region, one can study the n-n pairing since the pairing energy is $2\Delta_{nn}$. The Fe chain of isotopes shows an incredibly stable behavior of the n-n pairing energy but when going to higher masses (Ni and Zn) this energy drops at $N = 37$ (very sharply for Ni). This drop in the pairing energy does not completely support the arguments of Langanke *et al.* [Lan+03] to explain the small ^{68}Ni $B(E2)$ values. From the orbital occupation point of view, it costs less energy to break the pair (37,38) in the $\nu f_{5/2}$ shell than exciting a pair of protons in the closed shell $\pi f_{5/2}$. From the pairing energies, this pair seems to be very weak and the system does not gain much energy by doing so. If it is the case, then it is clear that it costs less energy to break this very weak pair of neutrons than exciting the pair of protons in a strong closed shell. However, this is not in contradiction with their conclusion and even supports the hypothesis that the

[4]The experimental half-lives were found to be much longer than the calculated ones when using only the *pf* shell (without including the *g* shell). The spin measurement of ^{63}Mn is needed to confirm the occupation of the $\nu g_{9/2}$ shell. The pairing effect shifts up neutrons from the $\nu f_{5/2}$ to the $\nu g_{9/2}$ shell already before reaching $N = 40$ which increases the life-time.

$B(E2)$ is dominated by neutron excitations. This drop in the pairing energy (in Z-even) appears later in the Zn isotopes but does not appear for Fe isotopes.

One should keep in mind that any conclusion could be made from this mass filter concerning the occupation of the orbitals since it could be masked by other collective effects but at least this indicates unexpected phenomena happening in this region which needs to be explained by more experimental and theoretical investigations.

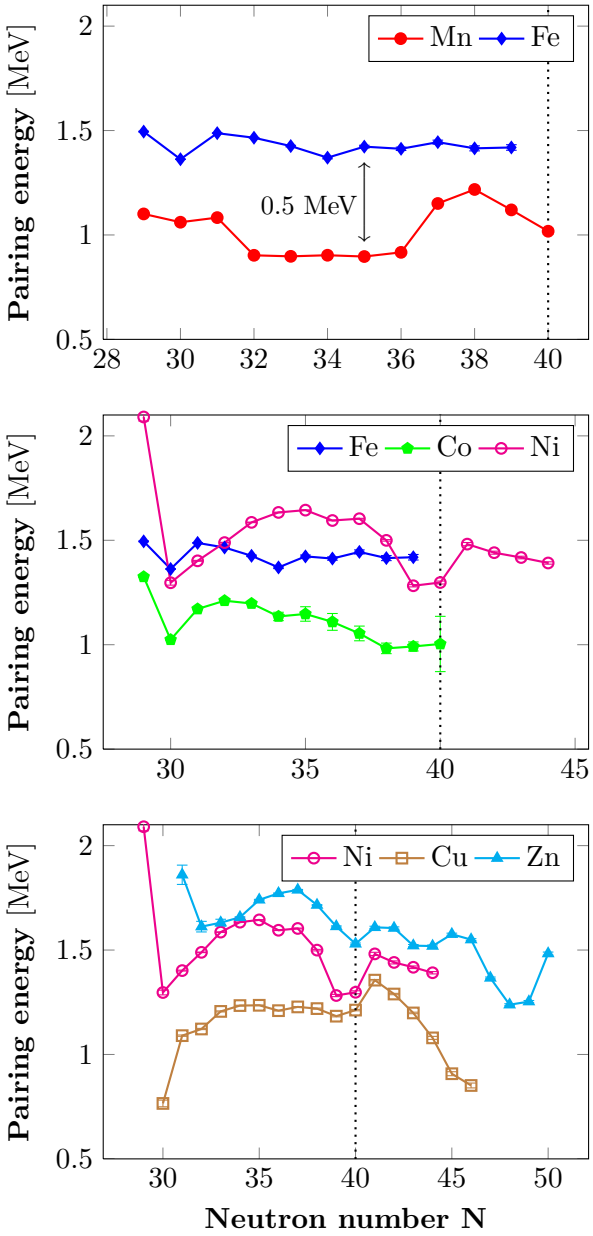

Figure 6.15.: The experimental pairing energies plotted with N for $25 < Z < 30$ (Mn, Fe, Co, Ni, Cu and Zn).

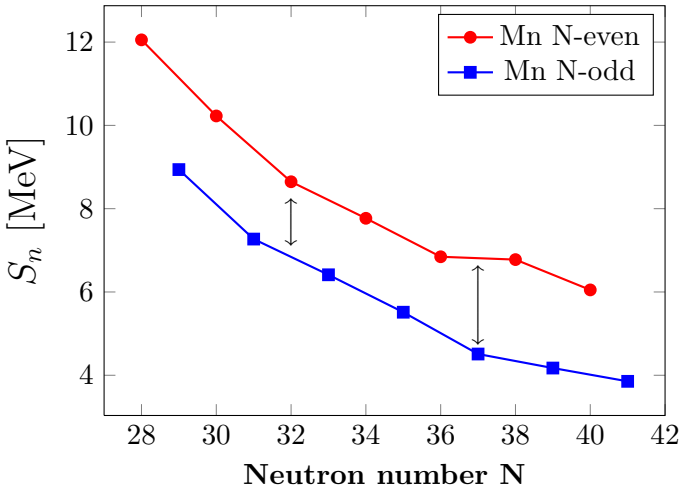

Figure 6.16.: The neutron separation energy S_n values for the Mn isotopes versus N. The pairing energy is the distance between the odd and even neutron curves. One can see the increase of the pairing at $N = 37$ caused by the increase of the S_n of $N = 38$.

Pairing energy from models In Figure 6.17, Figure 6.18 and Figure 6.19 are shown the predicted pairing energies of the HFB-14, FRDM and Duflo-Zuker models with comparison to the experimental values.

The model which reproduces the best estimation of the p-n strength (distance between Z-odd and Z-even curves) is the FRDM model, while the Duflo-Zuker model seems to ignore it completely. However, the FRDM model overestimates the pairing energies while the Duflo-Zuker model underestimates them. The HFB-14 model reproduces quite well the pairing energy of the Mn isotopes but fails when going for higher masses (even for iron). These models reach their limit here since the pairing energy varies at the level of around 100 keV, which is very difficult to reach for most of the theoretical models.

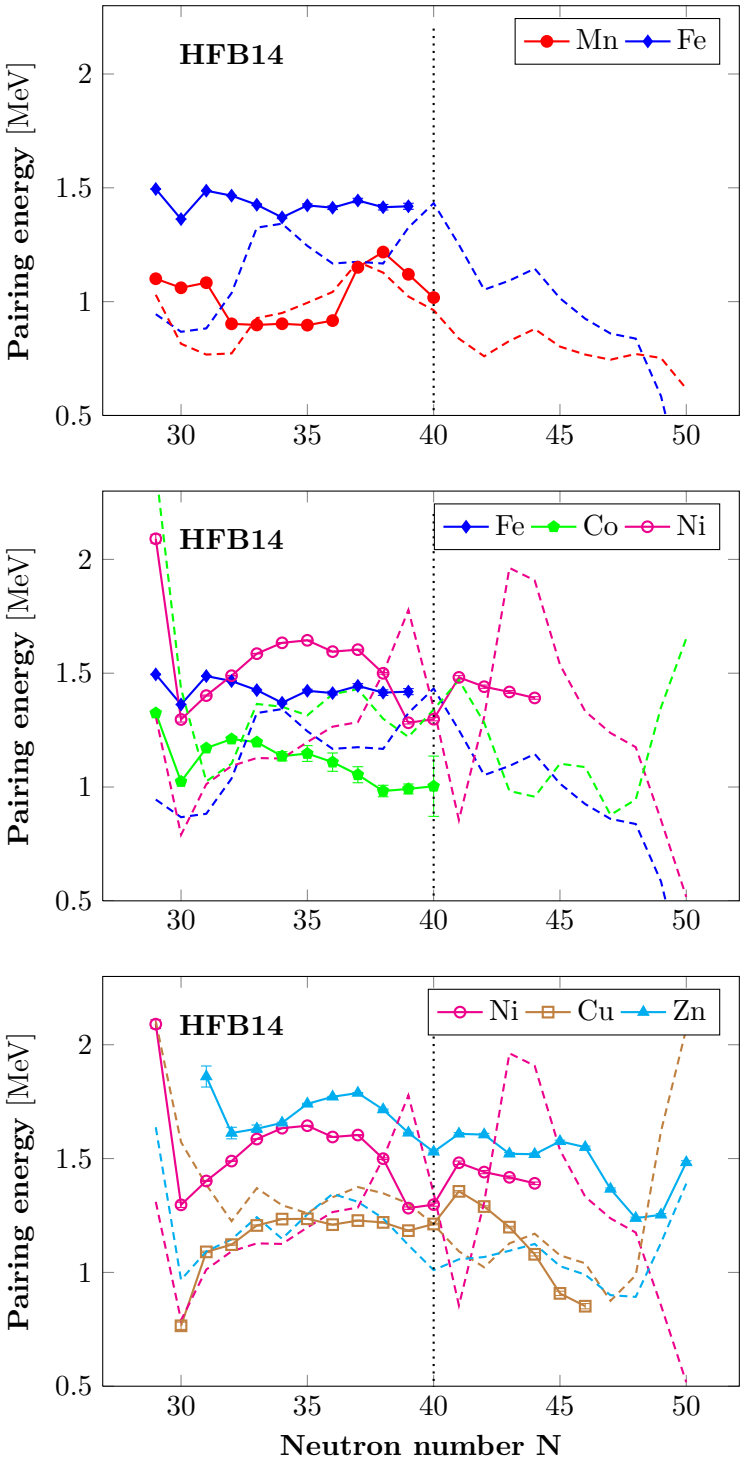

Figure 6.17.: Pairing energy versus N. For each isotopes chain the data are shown (solid lines) with comparaison to the HFB-14 predicted values (dashed lines).

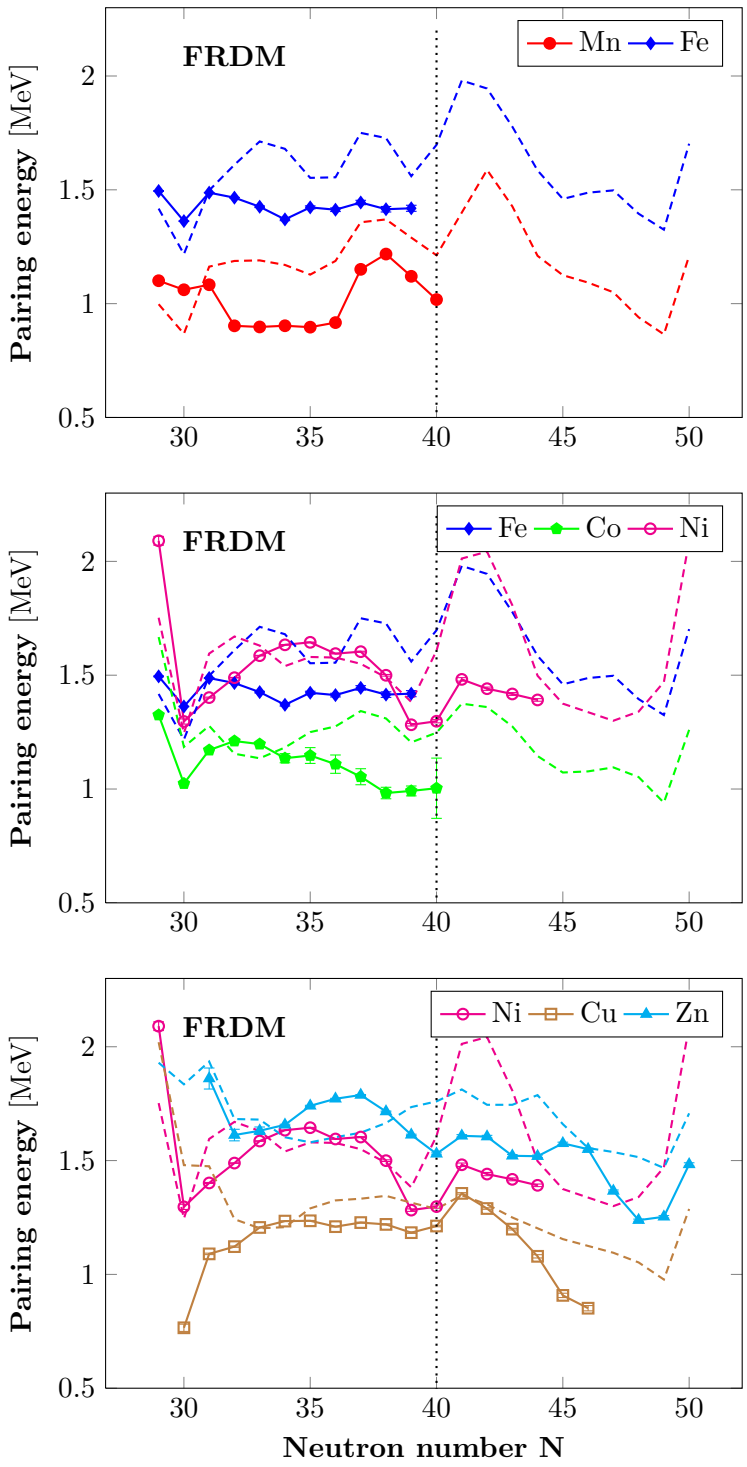

Figure 6.18.: Pairing energy versus N. For each isotopes chain the data are shown (solid lines) with comparison to the FRDM predicted values (dashed lines).

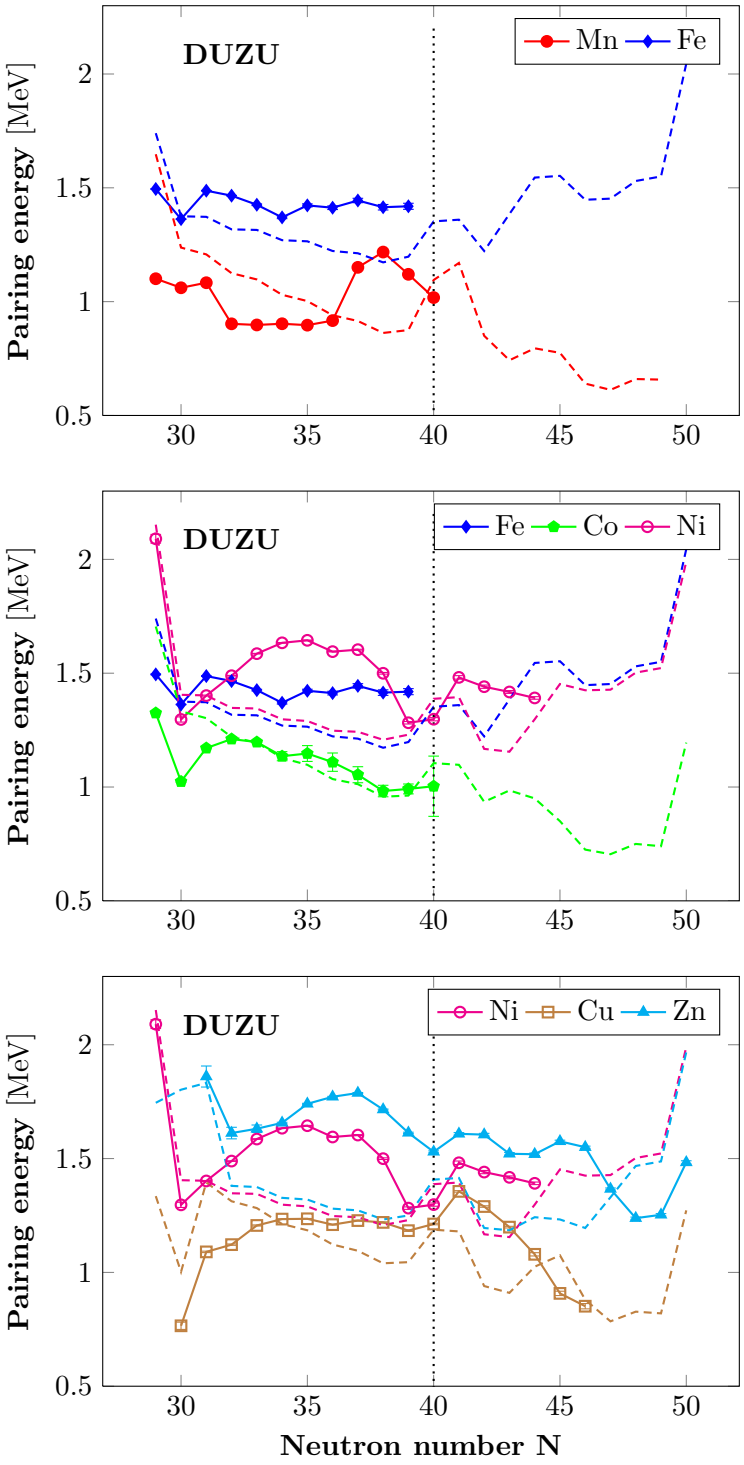

Figure 6.19.: Pairing energy versus N. For each isotopes chain the data are shown (solid lines) with comparison to the Duflo-Zuker predicted values (dashed lines).

6.1.3. What did we learn from the new mass surface?

From the examination of different mass derivatives, the onset of collectivity seen from the decrease of the energies of the first excited state 2^+ and the increase of the $B(E2)$ of the neutron rich Cr and Fe isotopes [Adr+08; Gad+10; Lju+10], is supported by the new mass surface. Because of this onset of collectivity, the $N = 40$ sub-shell disappears and no signature is seen from S_{2n} values neither from the "empirical" shell gap nor from the pairing energies. However, the increase of the S_{2n} values is very similar to the increase of the S_{2n} values in the "island of inversion" in the magnesium region as illustrated in Figure 6.20. This behavior in the manganese isotopes could be a signature of a new "island of inversion" below nickel which was proposed by Ljungvall *et al.* [Lju+10] from their observation on the iron $B(E2)$ values.

The occupation of the $\nu g_{9/2}$ orbital might explain the changes in the pairing energies calculated from the new mass surface. The anomaly observed at $N = 37$ in the Mn isotopes pairing energies might support the interpretation of Gaudefroy *et al.* [Gau+05]; *the pairing effects shifts up the neutrons from* $\nu f_{5/2}$ *to the* $\nu g_{9/2}$ *shell already before reaching* $N = 40$ *which increase the half-lives of these isotopes.* The strength of proton-neutron interaction (or pairing) is determined from the new mass surface via the distance between the pairing energies of Z-odd and Z-even nuclides. The p-n interaction between the $\nu f_{5/2}$ and $\pi f_{7/2}$ orbitals responsible for the lowering of $\nu f_{5/2}$ orbital and then the neutron occupation of the $\nu g_{9/2}$, is estimated to be around 0.5 MeV.

In summary, from the new mass surface $N = 40$ is clearly not a closed shell. The increase of collectivity in this region and the increase of the S_{2n} values at $N = 37$ might be a signature of a new "island of inversion" starting already at the Mn isotopes, which would support the conclusion of Ljungvall *et al.*

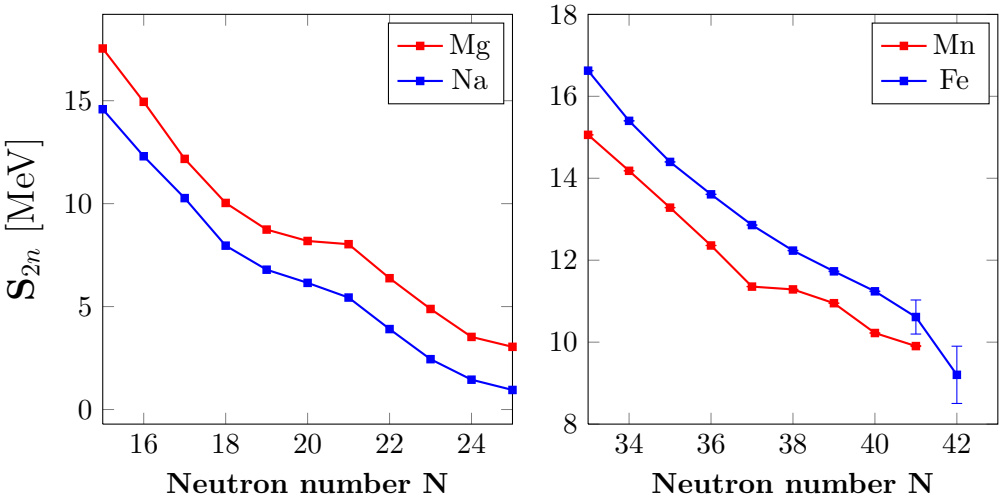

Figure 6.20.: Two neutron separation energy in the 'island of inversion' around ^{32}Mg (left). The similar behavior of S_{2n} values which increases along the Mn isotopic chain (right).

6.2. The quantum nuclear phase transition near A = 100

Another region where the nucleus takes a sudden and dramatically deformed shape is the region around $A = 100-$One of the most remarkable examples of nuclear shape transition (both for its intensity and its suddenness). Since its discovery [Joh65] many extensive experimental and theoretical studies have been performed. In this work, the mass surface is extended to more exotic nuclei: ^{96,97}Kr. A key information is brought from these new masses concerning the understanding of the deformation in term of quantum nuclear phase transition.

6.2.1. Understanding the region of strong deformation around A = 100

As it was pointed out in chapter 2, the deep indentations of the mass surface visible in the $A \approx 100$ region is the result of nuclear deformation. This feature is the manifestation of a first-order quantum phase transition where the nucleus change its shape suddenly at specific neutron number ($N = 60$). In Figure 6.21 are shown the S_{2n} values in this region. Most of the mass data was present in the 2003 Atomic-Mass Evaluation [AWT03] but was extended and considerably refined thanks to Penning-trap measurements by ISOLTRAP [Del+06] and JYFLTRAP [Hag+06; Hag+07].

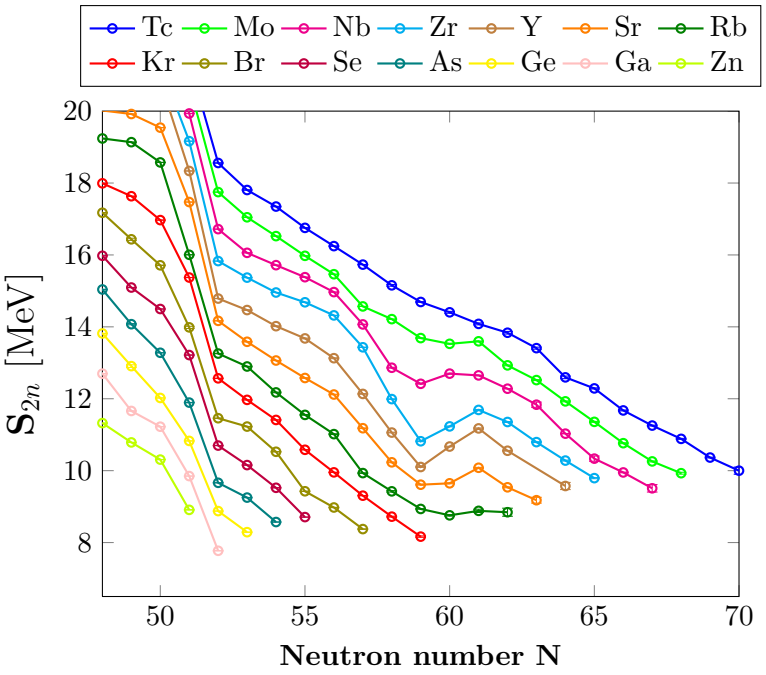

Figure 6.21.: S_{2n} values versus N in $A \approx 100$ region from the tabulated values of AME2003 [AWT03], new data from JYFLTRAP-2006/2007 [Hag+06; Hag+07] and ISOLTRAP-2006 [Del+06].

The Interaction Boson Model could reproduce the masses and the energy spectra of the neutron-rich even-even Zr isotopes as shown in Figure 6.22 [GR+05]. These calculations show how the Zr isotopes evolve from spherical into deformed shapes passing through a region where two minima exist (the potential energy surface has spherical minimum

and deformed minimum). By performing calculations along one isotopic chain, the IBM describes this evolution as quantum shape/phase transition. Unfortunately, no other calculation were performed in this mass region.

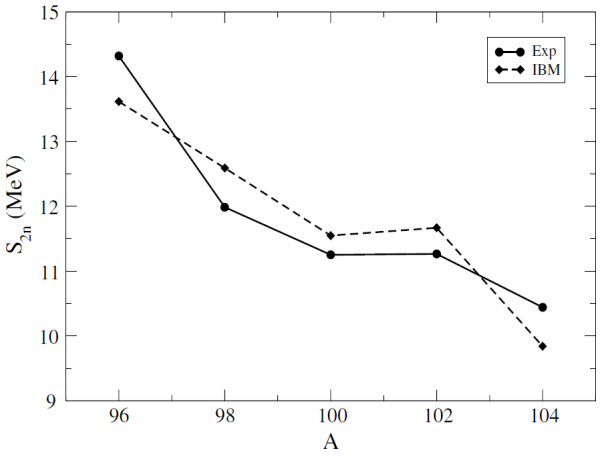

Figure 6.22.: Two-neutron separation energies for neutron-rich even-even Zr isotopes. Full lines correspond to experimental data, while dashed lines correspond to the IBM calculations (figure from [GR+05]).

Accompanying the discovery of this deformation region was the statement that ^{96}Kr would "most likely" have the same deformation as the neighboring nuclides. It is interesting to point out that the first microscopic calculations of shapes in this region [ASS69] predicted the same deformation for ^{96}Kr as for ^{98}Sr and ^{100}Zr. Likewise, recent density-functional-theory calculations using the Gogny force and collective Hamiltonian [Del+10], give a good overall description of this region. Another microscopic model, Hartree-Fock-Bogoliubov 17 (HFB-17) using Skyrme force [GCP09], predicts a strong deformation appearing at $N = 60$ for the krypton isotopes as illustrated in Figure 6.23.

Many experimental investigations concerning the krypton isotopic chain has been carried out. γ-ray spectroscopy of microsecond isomers of ^{95}Kr was performed with the Lohengrin spectrometer at ILL by Genevey *et al.* [Gen+06] who found that spherical shape predominates (at least at low energy) already at $N = 59$ for Kr. Coulomb excitation of ^{92}Kr performed at REX-ISOLDE [Müc+09] revealed an increased $E2$ strength and hence, enhanced quadrupole collectivity at the $N = 56$ $d_{5/2}$ sub-shell closure in contrast to previous conclusions [Lhe+01]. This sub-shell is clearly visible from the mass surface in Figure 6.21 for $Z = 37 - 42$ (Rb−Mo). The disappearance of this sub-shell for ^{92}Kr was illustrated by the ISOLTRAP mass measurements of Delahaye *et al.* [Del+06] and corroborates the REX-ISOLDE results. A γ-ray study of ^{96}Kr, recently performed at Legnaro with the PRISMA spectrometer and CLARA clover array by Marginean *et al.* [Mar+09], reported an excited state with a very low energy of 241 keV. Their assignment of this state to the first 2^+ state, though advanced with great caution, would be indicative of rather strong deformation which confirms the theoretical predictions.

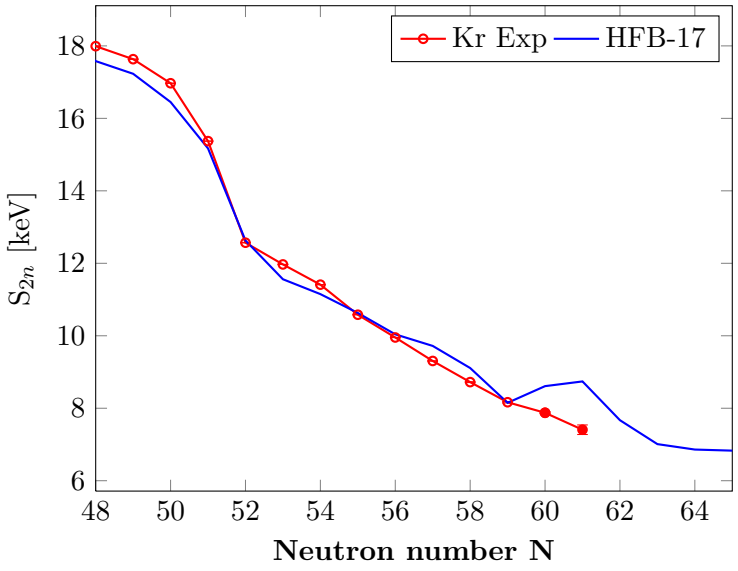

Figure 6.23.: Comparison between experimental S_{2n} values and calculated HFB-17 S_{2n} values. In contrast with the new measured ^{96,97}Kr mass values, the HFB-17 model predict large deformation for these isotopes.

6.2.2. The borders

The two new S_{2n} values resulting from the measurements of ^{96,97}Kr masses are indicated by solid points in Figure 6.24. Contrary to the heavier isotopic chains, where an increase in S_{2n}values indicates a gain in binding energy due to deformation, the S_{2n} values for Kr continue to decrease steadily with N. The behavior in this new area of the mass surface is in marked contrast with that shown by isotopes with higher Z. A "normal" linear trend only starts to be re-established for the $Z = 42$ (Mo) isotopes. Thus the critical points delimiting the area of the quantum phase transition appear quite clearly.

Additional support for this conclusion comes from comparing the new results with other observables. First, optical isotope-shift measurements by Keim *et al.* [Kei+95] (see Figure 6.24) revealed that the mean-square charge radius of ^{96}Kr ($N = 60$) did not significantly increase with respect to ^{95}Kr. This is in stark contrast with the heavier isotopic chains of Sr and Rb. Subsequent laser spectroscopy work on Y [Che+07], Zr [Cam+02], and Nb [Che+09] has also corroborated the dramatic shape change at $N = 60$. As in the case of Kr, both masses and recently measured Mo charge radii also smooth out when crossing the border region near $N = 60$, giving credence to the idea of a critical point [Cha+09]. To illustrate this transitional region, the difference between S_{2n} values at $N = 60$ and $N = 59$ is plotted in Figure 6.25 (top) along the isotonic chain ($Z = 36 - 45$). One can clearly see that this phase transition starts at $Z = 36$ (Kr) and stops at $Z = 43$ (Tc). The quantum phase transition reaches its maximum at the Y isotopes, where the nuclei gain a binding energy of nearly 1 MeV via deformation. On the same figure (bottom) is plotted the corresponding differences of the mean-square charge radii between the isotones $N = 60$ and $N = 58$ (unfortunately no data are available for all $N = 59$ isotones). The mean-square charge radii shows the same behavior where the strength of the phase transition reaches also its maximum at $Z = 39$ (Y) and is smaller

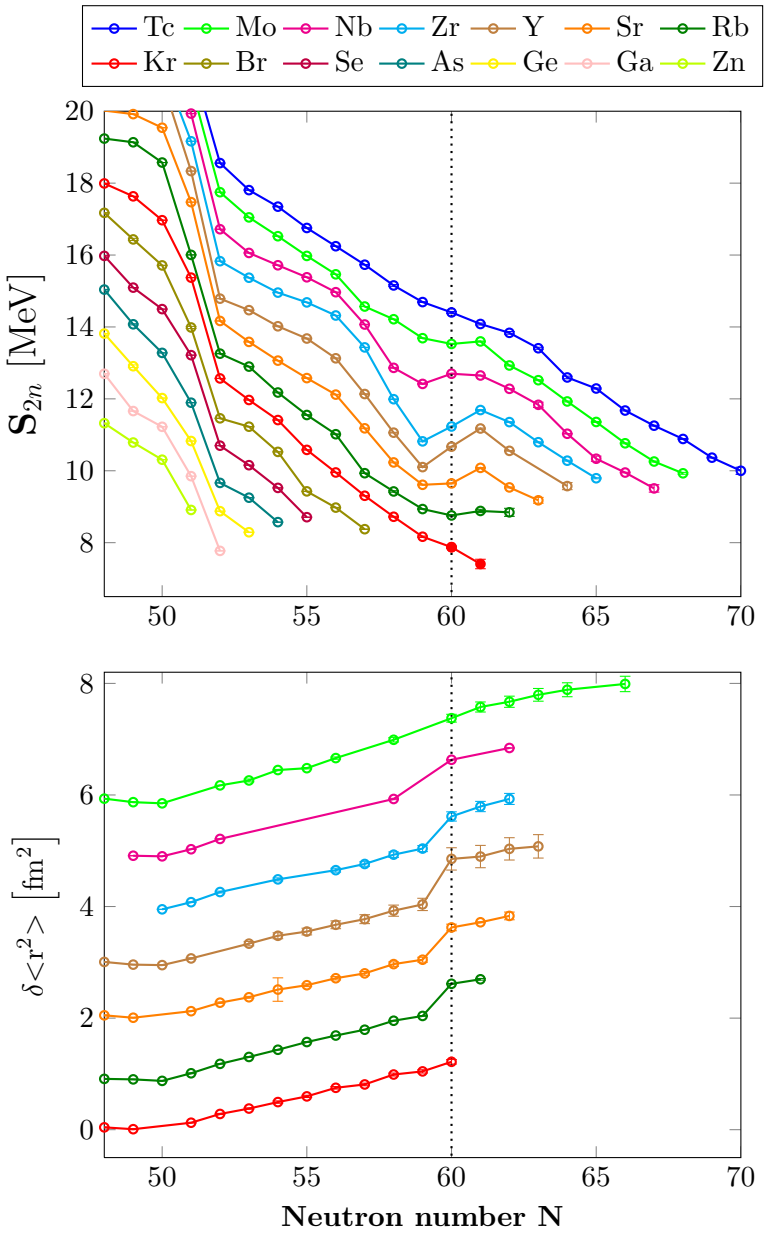

Figure 6.24.: (top) Two-neutron separation energies (S_{2n}) for $Z = 32 - 45$ versus N. The new Kr data reported here are represented by filled circles (error bars smaller than the points). Other data from [AWT03], complemented by [Del+06] for Kr, [Hag+06] for Sr, Mo and Zr, and [Hag+07] for Y and Nb. (bottom) Difference in mean-square charge radii for the $N = 60$ region. Data are from [Kei+95] for Kr, [Thi+81] for Rb, [Buc+90; Lie+91] for Sr, [Che+07] for Y, [Cam+02] for Zr, [Che+09] for Nb and [Cha+09] for Mo.

at $Z = 36$ (Kr) and $Z = 42$ (Mo). Technetium ($Z = 43$) charge radii are needed as well as the missing ^{101}Mo and ^{100}Nb in order to draw conclusion for the mean-square charge radii and its consistence with the masses.

γ-ray spectroscopy of ^{96}Kr by Marginean *et al.* which reveals a rather strong defor-

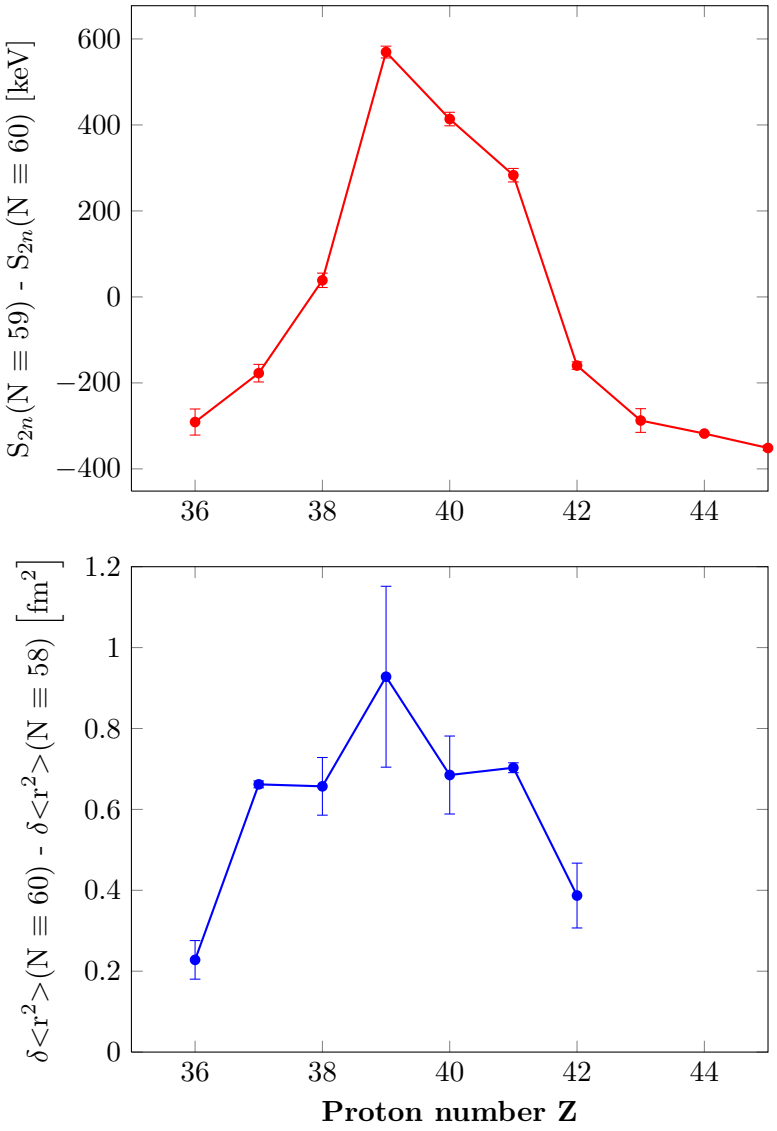

Figure 6.25.: (top) Difference between the two neutron separation energies of the isotones $N = 60$ and $N = 59$ plotted versus the proton number Z. (bottom) Difference between the mean-square charge radii of the isotones $N = 60$ and $N = 58$ plotted versus the proton number Z. The two observable illustrate the quantum nuclear shape/phase transition and its lower limits: krypton ($Z = 36$).

mation is then in strong disagreement with the masses and charge radii results of this isotope. Also, the new measured masses are in contradiction with the predicted ones from HFB-Gony and HFB-17.

The present masses of ^{96,97}Kr establish the limit of the region of strong deformation and allow for the first time, mapping the lower boundary of the region of critical-point behavior. These masses also reveal another border, the one of the microscopic models (HFB-17 and HFB-Gony) which cannot reproduce the binding energies behavior for

the Kr isotopes. Experimental measurements are encouraged as well as the theoretical calculations especially with Interaction Boson Model which was very successful for the reproduction of the Zr isotopic chain masses. It will be very interesting to see if these calculations can describe the critical-point boundary for the Kr isotopes.

7. Conclusion and outlook

In this work, mass measurements of the neutron-rich isotopes $^{58-66}$Mn, $^{61-63}$Fe and ^{96,97}Kr were presented. These measurements were motivated by the study of nuclear deformations of these nuclides and their impact on two important questions: $N = 40$ shell closure in the Ni region and the study of a nuclear phase transition in the Zr region ($A \approx 100$).

The measurements were performed using the mass spectrometer ISOLTRAP situated at the ISOLDE facility at CERN. This spectrometer is based on the Penning trap technique–the most powerful tool for high precision mass measurements, which allowed the measurement of short-lived neutron rich isotopes $^{64-66}$Mn and ^{96,97}Kr for the first time. ^{66}Mn (64 ms) is the shortest-lived nuclides never measured with ISOLTRAP. In the case of ^{97}Kr, the preparation Penning trap was used as a measurement trap since the transport to the precision Penning trap (where the measurements are usually performed) was not possible. A new fit function was needed to fit data from this trap, usually used to cool and purify the beam before the measurement in the second Penning trap. Simulations of the resonance shapes of ions detected after the preparation Penning trap were performed. A fit function was derived in the form of the "double Woods-Saxon"; inspired by the well-known nuclear potential, which gave very satisfying fit results to the measurements performed with this trap. Combining the cooling process and the measurement may offer an attractive prospect for mass measurements of nuclides even farther from stability. However, studies need to be done to estimate the systematic errors, which were inflated in the case of ^{97}Kr.

The results concerning the masses of the Mn isotopes showed no evidence for a shell closure at $N = 40$. Instead of showing a drop (behavior expected at shell closure), the two neutron separation energy plotted from the new Mn masses showed a sudden increase at $N = 37$. This behavior is similar to that revealed by spectroscopic observations in the same region where the first excited states and the probability transitions between the first excited state and ground state were measured. These measurements revealed an increase of collectivity due to deformations arising in this region which was also reflected from the increase of the two neutron separation energy of the Mn isotopes. These deformations may find their origin in the neutron occupation of a higher shell ($g_{9/2}$) which could result from the large proton-neutron interaction, estimated from new masses to be around 0.5 MeV. To confirm the analogy made with the "island of inversion" in the Mg region, the spins of Z-even and N-odd nuclei in the Mn region should be measured. The neutron-rich Cr masses are needed and the existing ones should be remeasured with higher precision in order to probe the fine structure and confirm the onset of deformation starting from the Mn isotopes at $N = 37$.

Another onset of deformation was expected for the Kr isotopes from a measurement of the first excited state of ^{96}Kr. Also a sudden deformation was predicted from microscopic calculations of shapes in this region and the same deformation for ^{96}Kr as for ^{98}Sr and

^{100}Zr is expected. In contradiction with experimental findings and theoretical prediction, no sudden deformation was observed from the new masses of ^{96}Kr and ^{97}Kr. The Interacting Boson Model calculations have focused on the collective features present in the rare-earth region around $A = 150$ and provide a good picture in terms of a quantum phase transition. Also some calculations were performed in the Kr region but only for the Zr isotopic chain. The sudden increase observed for the Zr two neutron separation energies was nicely described as quantum nuclear shape/phase transition. It would be interesting to test the predictive power of this model by extending these calculations for the Kr isotopes. However, in the framework of this model, the behavior of the new mass surface delimits the border of the quantum phase transition. The Kr masses could be considered then as boundaries of critical-point in the $A \approx 100$ quantum phase transitional region.

The IBM model calculations are encouraged as well in the Mn region in order to see if this onset of deformations at $N = 37$ could be also explained in terms of quantum nuclear shape/phase transition.

The other important result of the work of the thesis is the on-line commissioning of new spectroscopy decay setup–an extension of the ISOLTRAP experiment. Installed behind ISOLTRAP and at the ISOLDE facility, this unique setup will offer many opportunities to perform spectroscopic and decay studies with highly pure radioactive beam. The reader is invited to review Appendix A for technical details of the setup.

Appendices

A. Isoltrap extension for spectroscopy: Tape station setup

A.1. Physics motivation

Decay spectroscopy of rare isotopes becomes challenging at conventional ISOL-facilities when going far from stability due to high background generated by the isobars of the wanted nuclide. 'In-flight' facilities do not suffer from this limitation but the radioactive products are implanted deep in the focal-plane detector which may limit the resolution and sensitivity. To overcome the contamination problem of the ISOL-facilities, many techniques were developed such as the resonant laser ionization ion source (RILIS)[Fed+03]. Other solution is the use of a neutron converter in which reactions with secondary neutrons favors the production of neutron-rich nuclides [Kös02] or a quartz transfer line which can slow down the release of many surface-ionized beams. Ongoing developments include an ionizer cavity made of a low work-function material [Men+08] or the laser ion source trap (LIST) where the surface-ionized ions are repelled by a positive potential [Bla+03; Sch+08].

These methods improved a lot the efficiency of the ISOL-facilities, but still cannot suppress all isobars. Therefore a use of mass separator with high resolving power is needed to perform decay studies with pure beams. Using a mass spectrometer based on Penning trap techniques as mass separator might give a very good alternative between half-lives and high purity beams. The considerable advantage of Penning traps is their selective capability, they can clean the contaminated beam and also select the wanted ions from huge bunch of unwanted ones. Also Penning traps can reach a resolving power needed not only to resolve isobars but also isomers which will offer a decay study of isomeric pure beam–something not possible with other mass spectrometer[1]. In addition to decay study one can perform simultaneous mass measurements and use the decay system to verify the purity of the beam in the case of unknown masses and known half-lives and/or γ-scheme, etc. Unfortunately and like other systems, Penning traps have also their limitations. The main limitation is the half-life of the wanted nuclides, one have to find a compromise between half-lives and resolving power (see section 4.4). The other limitation is the efficiency of these mass spectrometers, the ion loss is mainly due to the cooling techniques essential for trapping which is no limiting for mass measurement since only few ions are need in the trap (the RFQ-Buncher in the case of ISOLTRAP where the efficiency is bellow 1%).

The first use of a Penning-trap system as a spectroscopy tool was perform with the mass spectrometer JYFLTRAP in Jyväskylä where β-decays of neutron-rich ^{100,102,104}Zr isotopes

[1] Usually the isomer mass is very close to the ground state mass (from few ten to few hundred of keV).

were studied as well as their direct mass measurements [RA+07]. The determination of the β-strength distributions of the latter isotopes have been studied with significantly improved precision in addition to the determination of the Q-values (difference of two masses) of the same isotopes in the same experiment. Thus, this shows that Penning trap is a powerful tool in nuclear spectroscopy in addition to its use for high precision atomic mass measurements.

Using the mass spectrometer ISOLTRAP as spectroscopy tool will offer access to more radioactive nuclides since it is placed at ISOLDE where more nuclides could be produced.

A.2. Technical requirements and challenges

The main intent is to make a decay study with pure isobaric beam and if possible pure isomeric beam which can be achieved by the use of the two ISOLTRAP Penning traps. However, this will not avoid the radioactivity contamination coming from the decay of the mother nucleus. For this purpose a movable tape is usually used to remove the contamination from the implantation/observation point after a certain observation time. For long-lived species, the tape is used to transport the radioactivity to another observation point (far from the implantation point and where other detectors are placed). To perform efficient implantation of the ions in the tape and avoid any losses due to the gradual diffuseness of the ions in the tape material, the beam is accelerated behind the trap from a few eV to 20-30 keV.

The other requirement is to have a large solid-angle coverage by radiation detectors to avoid decay radiation losses. Very efficient solution is to place β or/and α detectors inside the vacuum, to avoid attenuation when the light particles go through any material. Gamma detectors could be placed outside vacuum behind a Kapton window[2] or thin aluminum walls of the vacuum chamber. At the same time, relatively small ion beam size is needed in order to have correct coincidence measurements.

To satisfy all these requirements, many challenges in the installation of such system at ISOLTRAP had to be overcome. The main challenge is to retain the vacuum to at least 10^{-8} mbar which is crucial for the resolving power of the precision Penning trap and also for the precision in case the masses are measured simultaneously. A typical decay spectroscopy system supports vacuum of $10^{-5} - 10^{-6}$ mbar and some systems even kept under atmospheric pressure. Such poor vacuum is mainly due to unavoidable out-gassing of the transport tape and of the plastic Kapton windows used often for efficient beta-radiation transmission.

The other main challenge is the limited height available behind ISOLTRAP for ion optics elements necessary to focus and re-accelerate the beam in front of the decay chamber where the tape and γ and β detectors are installed. The limit is given by the ISOLDE crane, which leaves only 40 cm for these elements and the decay chamber itself. Also, the proximity of the 5.9 Tesla precision Penning trap magnet disrupts the ion trajectories and the photomultipliers needed for the β-detection.

[2] Insulator very stable for a wide range of temperature from 0 to 673 K, the vacuum which can be reached with such insulator is about 10^{-6} mbar.

A.3. Solutions and the present setup

A.3.1. Isoltrap modification

The main modification to ISOLTRAP after adding the decay-spectroscopy system are in hardware behind the precision trap. Previously, the last element of the ISOLTRAP system was a vacuum chamber housing a Channeltron ion detector fixed to the upper vacuum flange and used for recording the time-of-flight resonances and multichannel-plate (MCP) system which could be used as a spare detector and was mounted on a movable feedthrough several centimeters below. The chamber hosted two electrodes which could be used to focus the ion beam onto the detector surface (see Figure A.1).

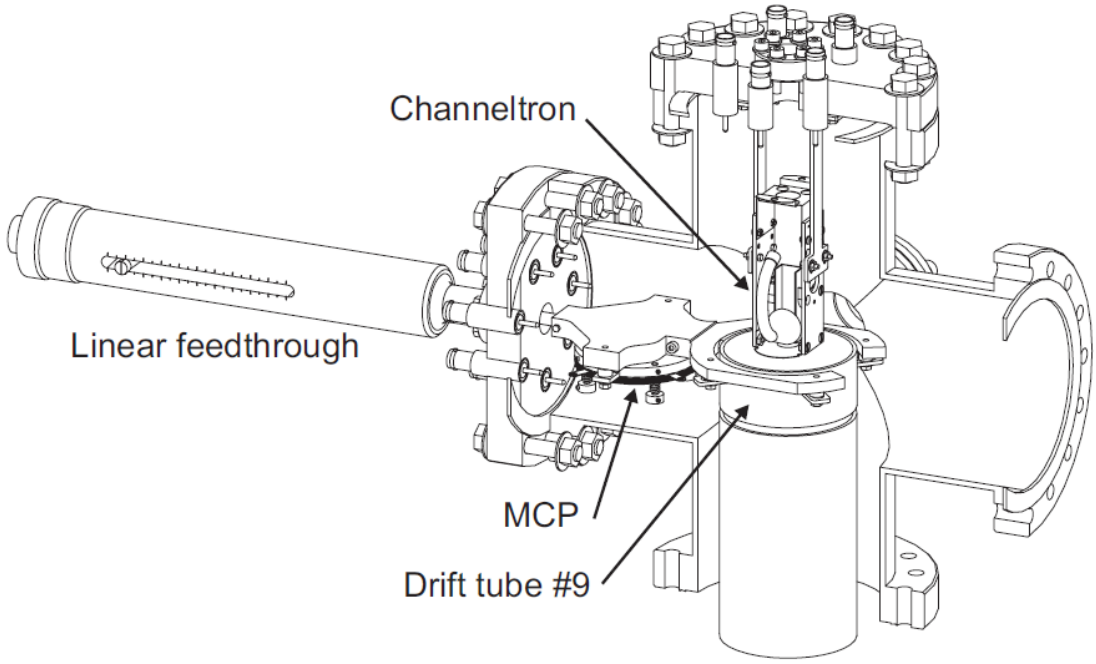

Figure A.1.: The last ISOLTRAP vacuum cross before the decay setup installation. Two ion detectors could be used, Channeltron fixed on the upper flange and a movable multichannel-plate (MCP) detector.

For the purpose of decay studies the above-mentioned chamber was exchanged and several elements were mounted above it. Figure A.2 presents in more detail the new elements of the ISOLTRAP setup.

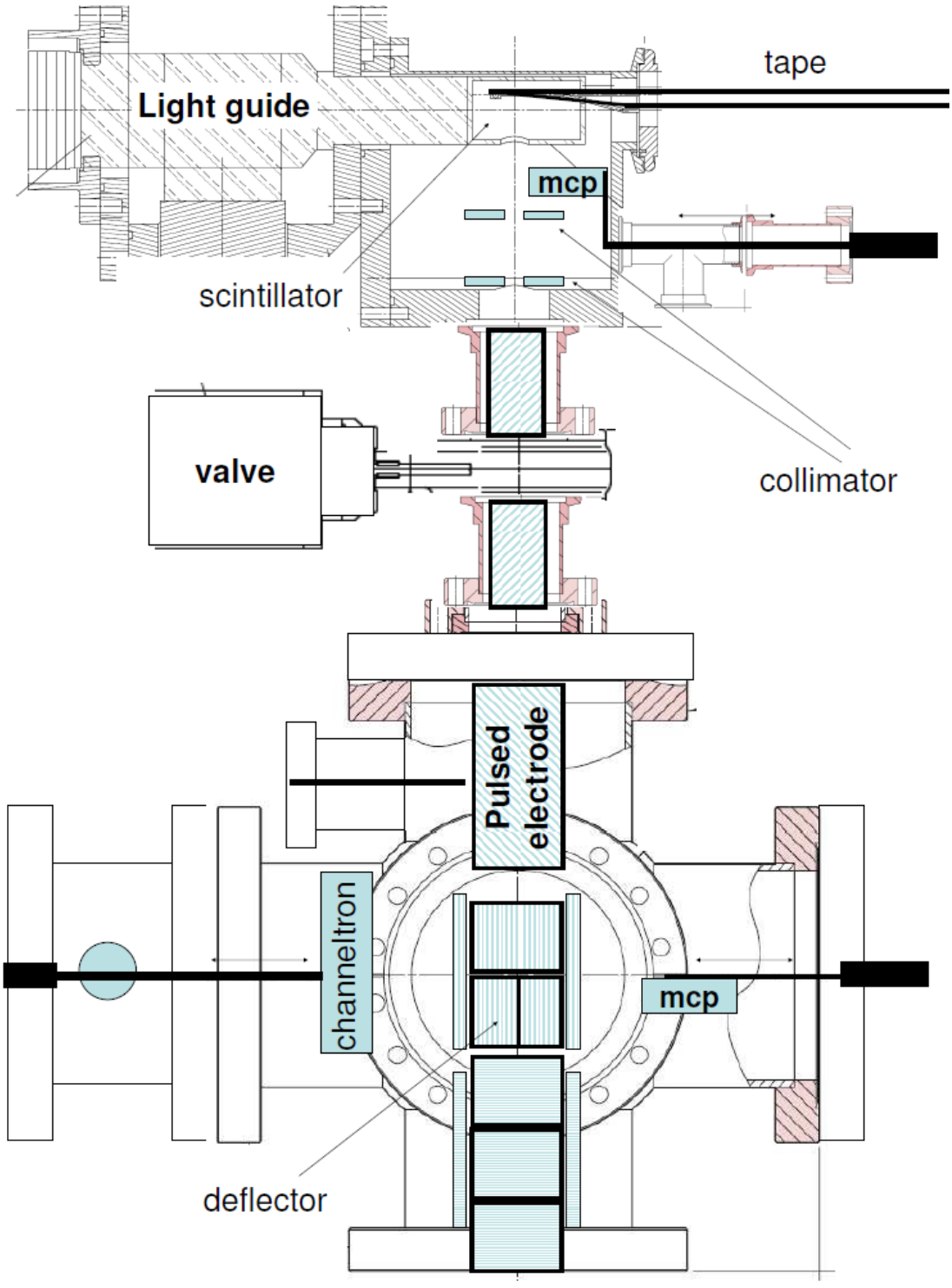

Figure A.2.: Schematic view of the modified ISOLTRAP last vacuum chamber used conventionally for mass measurements. The ion optics elements used to focus and accelerate the beam onto movable tape, together with the decay-detection chamber hosting the collimators, ion detector, scintillator, and implantation tape. Ion beam elements are marked in stripes.

The two electrodes in the previous ion detection chamber were exchanged with three electrodes, which can act as an Einzellens. Above, three mechanical feedthroughs are installed, hosting the channeltron, the MCP, and two focusing electrodes. In the case of mass measurements, either the channeltron or the MCP are moved into the ion path. For decay-spectroscopy studies the two electrodes are used, with the lower one split in four segments, for beam deflection. The upper flange is holding an insulated electrode which can be switched from -1.5 kV up to 20-30 kV in order to accelerate the ion beam. The electrode is only 7-cm long (because of the height limitation), but it is just enough to fit the whole ion bunch of 5-7 cm length. Behind these elements there are two small electrodes with an ultra-high-vacuum valve between them which allows separating the good vacuum part below it from the decay chamber above it during mass measurements. The small size of these electrodes allows the use of small vacuum tubes acting as a pumping barrier and saving the limited space with a small, thin vacuum valve. Tests with a diaphragm (4 mm in diameter and 40 mm in length) at the position of the first electrode behind the pulsed electrode did not improve very much the vacuum in the precision trap, and led to large losses in ion transfer.

A.3.2. The decay system

Behind the second electrode comes the implantation and decay chamber (shown in more detail together with the detectors and tape-movement box in Figure A.3). The vacuum challenge was addressed by making the decay chamber of aluminum, with very thin walls (1.6 mm), through which γ-particles pass with almost no energy losses. This was combined with strong pumping in the decay chamber and the mass-determination chamber, as well as small vacuum flanges below the decay chamber, as described before. The chamber and beta-detection part are a modified version of the system designed used by the CENBG-Bordeaux group [Mat+08]. In the lower part of the chamber one or two collimators can be placed in order to block the ions which would be otherwise deposited on the scintillator and could give rise to unwanted background. Above it a small, 2.5-cm MCP detector, is mounted on a mechanical feedthrough and can be moved into the ions' path for ion transfer optimization. Just 1 cm above it comes the beta-scintillator tube with the implantation tape located in its center. The conducting tape is mounted on conducting rollers on a support which is fixed to the tape-movement system. This allows very short intervention time in case the tape breaks or a radioactive source should be inserted into the chamber and it makes it an easy-to-handle system. Until recently the tape-movement setup was the system designed and used previously at the GSI Mass Separator and the results presented here were obtained using this system. Its advantages include compact size and a very reproducible tape movement (better than 1-mm precision), which is essential for studies on longer-lived species, whose decay should be observed further away from the implantation point, after accumulating several ion pulses. However, its large drawback is the tape width, only 6-mm, and the need to minimize tape path to avoid tape breaking and sliding. For this reason the tape is placed at 45 degrees with regard to ion trajectory, which leads to only 4.5-mm available for ion implantation. As will be shown later, this led to problems in accurate ion implantation. At the beginning of 2010 an old ISOLDE tape-station with a broad tape became available and it has been since implemented in the ISOLTRAP setup. Its clear advantage is the

10-mm tape width oriented at 90 degrees to the ion path. However, its movement is not so reliable and it cannot be used efficiently for beta- and gamma- studies on longer-lived species.

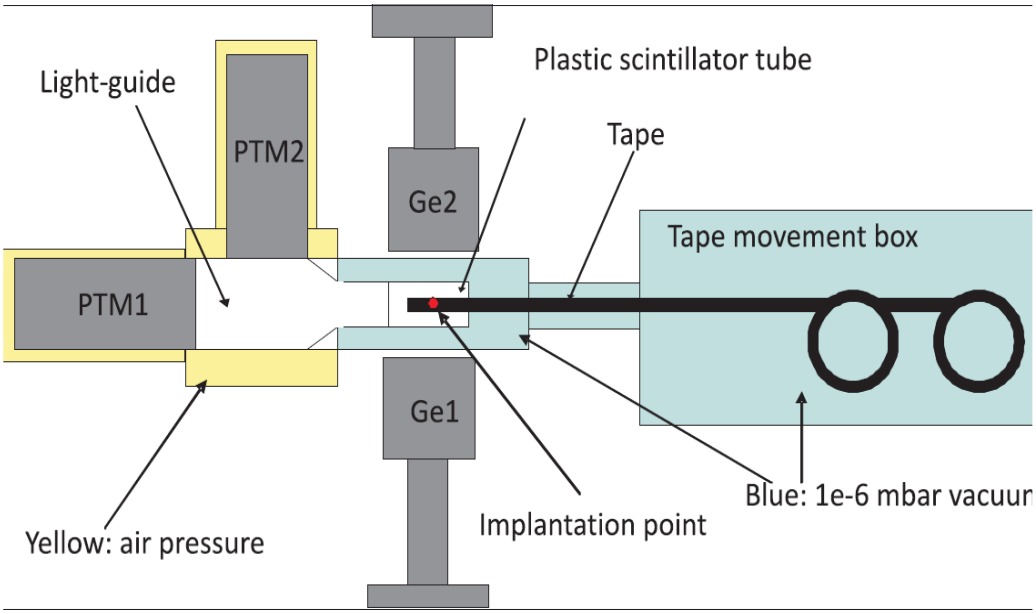

Figure A.3.: The top view of the ISOLTRAP decay-detection chamber, together with the beta- and gamma-detectors and the tape-movement system. The chamber and tape-box are kept under vacuum, while the lightguide, photomultipliers and Ge detectors are placed outside the vacuum.

The first part of the decay detection system is a thin, 2-mm thick, plastic beta-scintillator tube (BE408 from Saint Gobain) of 5 cm length and 3 cm diameter located inside the vacuum chamber (see Figure A.2 and Figure A.3). It is glued to a lightguide which is in contact with a rubber ring which ensures the vacuum tightness of the chamber. The lightguide guides the scintillating light to two photomultipliers (PTM, XP 2262B by Photonis) whose coincidence signal is recorded. Both PTMs are surrounded by mu-metal tubes to ensure shielding from the 10-30 Gauss residual magnetic field of the precision Penning trap magnet. This beta-detection system is an integral part of the full detection setup and should be in principle used in an unchanged configuration for all envisaged experiments.

The gamma-detection part is more modular, since the detectors are placed outside the vacuum and it can be thus modified more easily. In the commissioning studies presented here, ISOLDE coaxial germanium detectors were used: Canberra model GC 7020 and Eurisis model EGFP 3800-20-R with a thin window allowing the detection of X-rays. So far, no detector was placed on top of the detection chamber due to height limits. It is however envisaged to place there a NaI detector, which is more compact than a conventional Ge detector.

Concerning the data acquisition system (DAQ), at present it is still independent of the ISOLTRAP DAQ used for mass measurements [Bec+04] (using the LabView-based Control System software from GSI). So far, two decay DAQ systems have been used, both of which can be triggered by the ISOLTRAP measuring cycle (usually the trigger

comes when the ion beam is ejected from the precision trap towards the tape). In the first case, the ISOLDE DAQ for decay studies was used, based on the GSI MBS general purpose DAQ [NK08] and Go4 software package [Ess09]. MBS allows recording the β- and γ- spectra, as well as obtaining coincidence events. The second system is much less complex and can be used mainly for assisting the mass measurements. It uses a multichannel scaler (Stanford Research SRS340) to count beta signals read-out by a small LabView-based program and Canberra multichannel analyzer DSA-1000 connected to Canberra Genie-2000 software to record gamma spectra. This system is very easy to use, but has no capability of coincidence studies.

A.3.3. Simulations of the ion-trajectory

After studying all the possibilities and according to all the mechanical constraints, simulations of the ion-trajectory were needed before machining the electrodes in order to check the feasibility of this new setup. The ion-trajectory simulations in electric fields of the electrodes and the fringe field of the precision Penning trap magnet were performed using the SimIon 8.0 software package [Ser06]. Two kind of simulations were performed for the two modes of the setup: the *spectroscopy* mode and the *mass measurement* mode.

Initial conditions Before starting the simulations with SimIon software, the correct initial conditions had to be defined. For this purpose, a C++ program was used to simulate the quadrupolar excitation (this program was developed by [Yaz07]). With this program, the coordinates and the energy of the ions after the quadrupolar excitation can be computed according to the equations of motions as described in chapter 3. The frequency scan around the cyclotron frequency is simulated with this program, the ions are then created in the center of the trap and are ready for the trajectory simulation with SimIon software. The ions used for all the simulations are the singly charged $^{133}Cs^{+}$. The ejection from the trap is simulated using a *lua* program [ICF10] running during the ion-flight in SimIon workbench.

Spectroscopy mode The simulations for this mode consist on defining a set of electrodes voltages from the trap to the last ion-detector placed in front of the β-detector and on the beam-line axis as shown in Figure A.4. Also the ion energy should be switched to 30kV for efficient implantation in the tape. Another *lua* program was used to simulate the pulse of the pulsed electrode from -1.5 kV to 30 kV. This electrode is switched when the bunch of ions is inside the electrode, which correspond to $\approx 172\mu s$. This value could be adjusted according to ion-bunch length. In order to reduce the ion-bunch size, to switch all ions at the same time, an acceleration is need after the trap. This can be insured by relatively high voltage in drift 2 & 3. These two electrodes are usually used to decelerate the ions behind the trap. This deceleration is crucial for mass measurement, by doing so all the cyclotron motion can be converted to axial motion since the ions are decelerated when the magnetic field is at its maximum (see Figure A.5). In the spectroscopy mode the deceleration is not needed. It is even problematic because of the increase of the ion-bunch size which makes the switching very inefficient. An example of the simulations performed for the spectroscopy mode is shown in Figure A.6 in 2D plan. Figure A.7 illustrate the pulsing from -1.5 kV to 30 kV of the same example.

The figure shows the surface of the electric potential from the pulsed electrode to the ion detector. All ions are switched at $172\mu s$. The ion-energy is not switched at the same ion-position which reflects the ion-energy spread. The settings used for this example are -200 volts for drift 2 and -600 volts for drift 3, instead of -2.6 volts for both in the mass measurement mode.

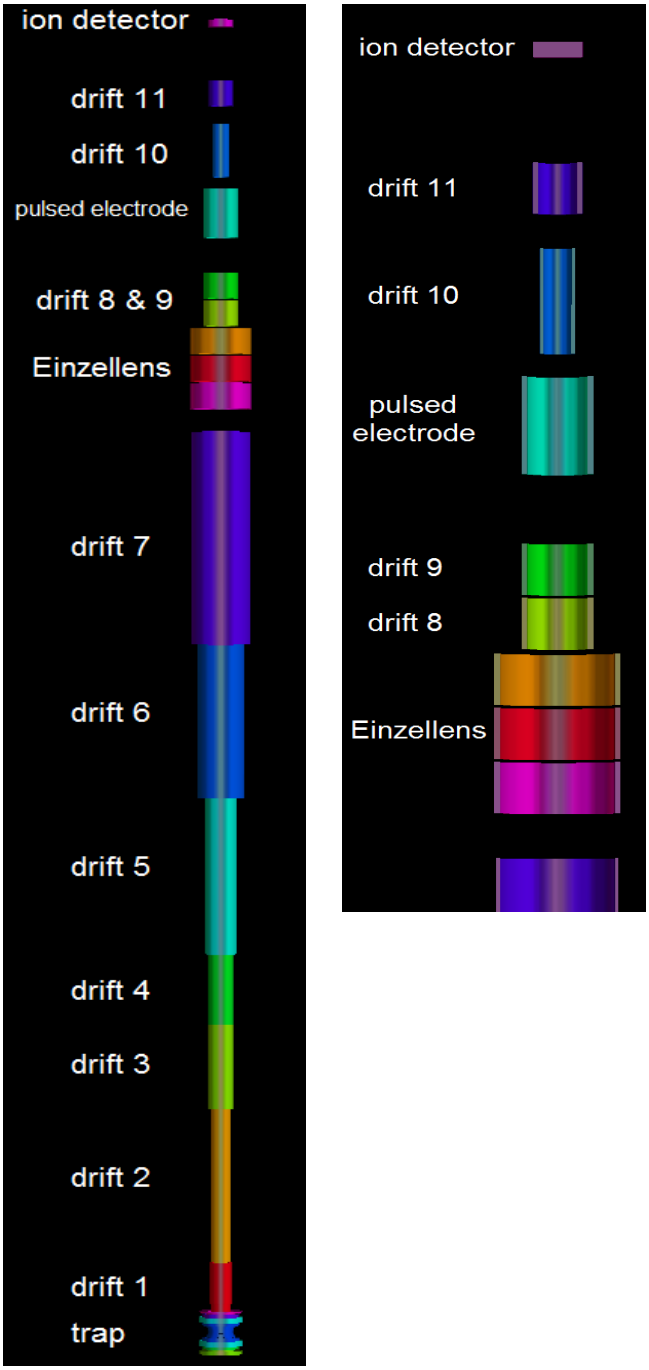

Figure A.4.: Geometry of the spectroscopy mode from the precision Penning trap to the last detector in front of the β-detector. On the right is shown a zoom of the modified part.

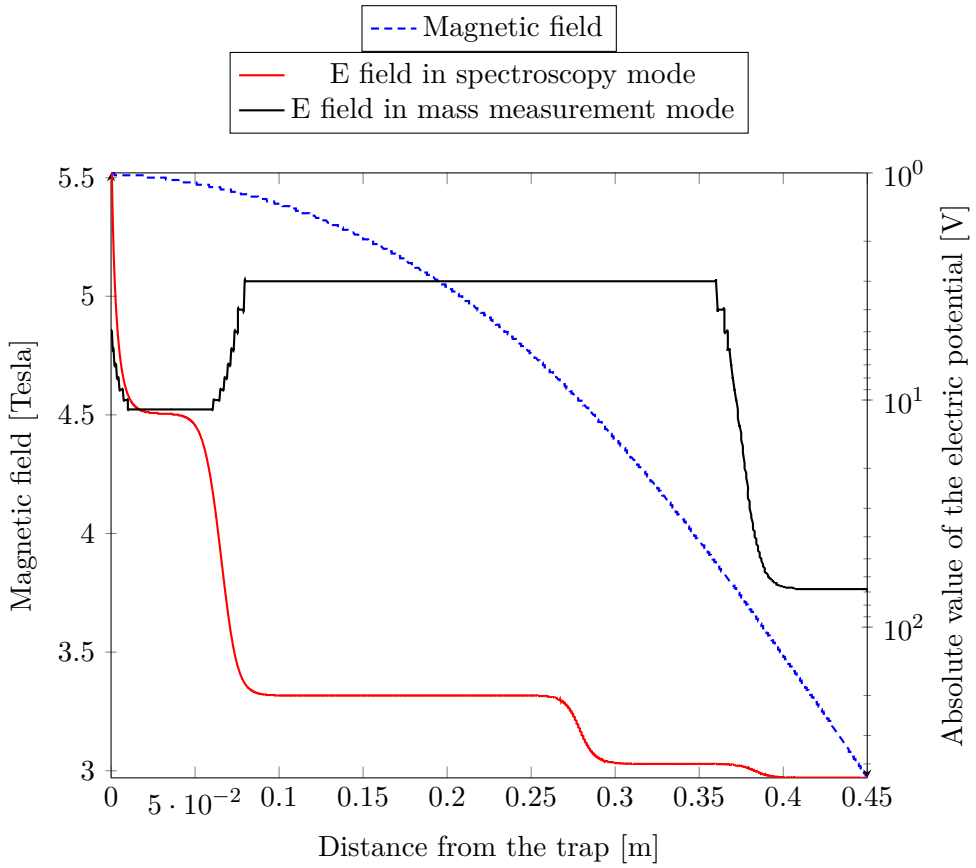

Figure A.5.: Magnetic and electric fields behind the precision Penning trap. Two sets of electric field versus a distance from the trap are shown: (red) electric field in the spectroscopy mode, (black) electric field for the mass measurement mode.

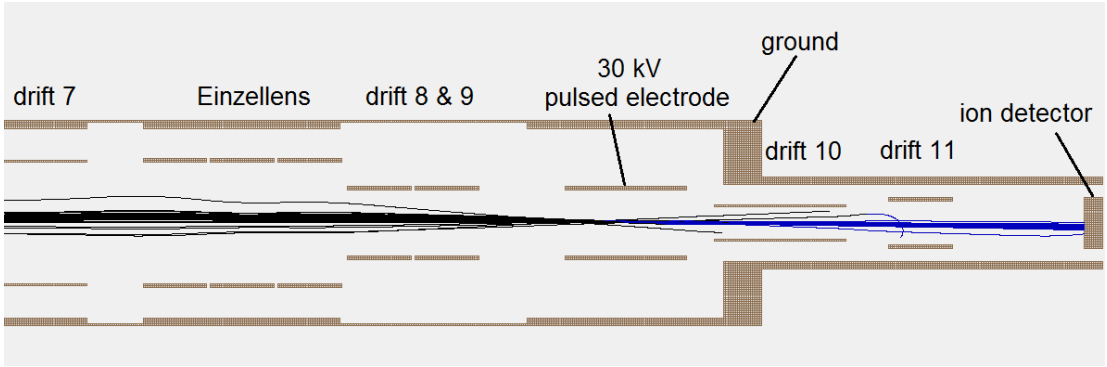

Figure A.6.: Example of trajectory simulation of a bunch of $^{133}Cs^{+}$ ions with SimIon software. Zoom on the last ISOLTRAP modified part, the black lines represent the ions with the energy as ejected from the trap and the blue lines represent the accelerated ions at $\approx 172\mu s$ after the trap ejection.

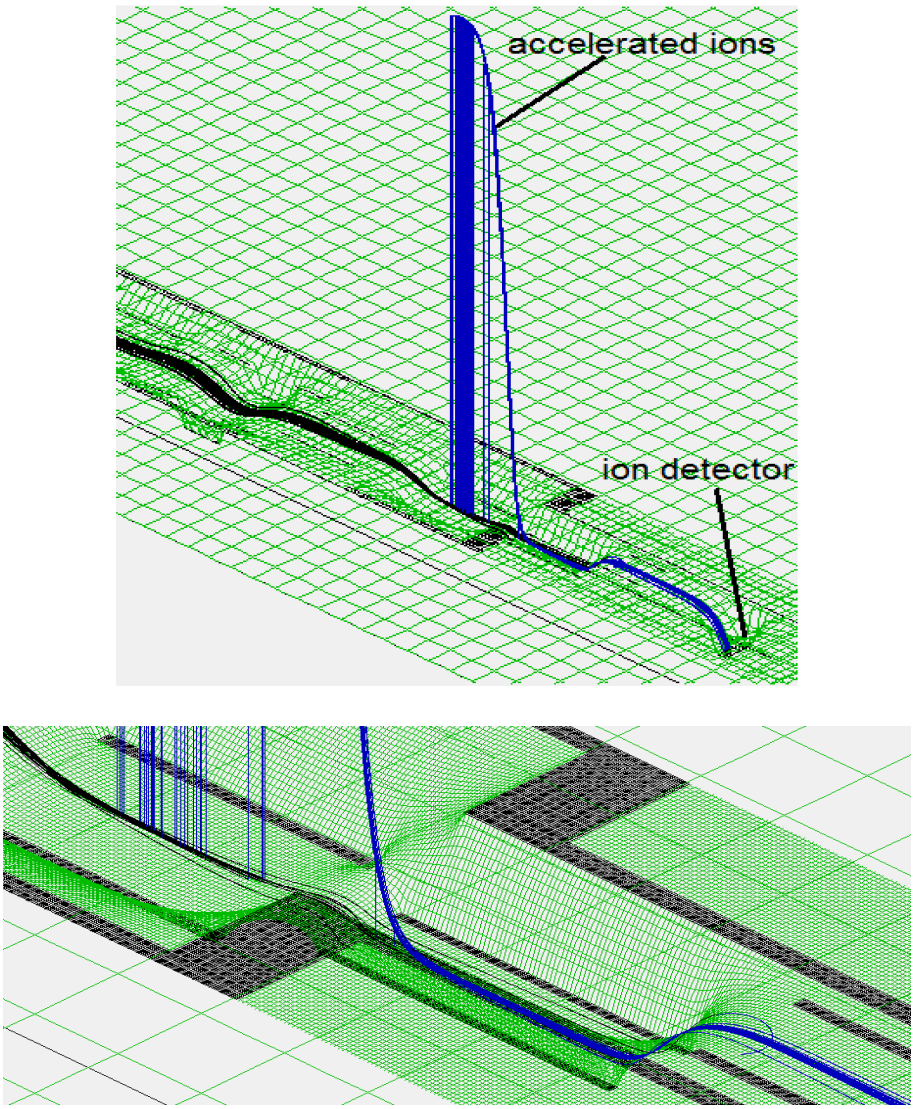

Figure A.7.: (top) Electric potential surface of same simulation in Figure A.6. One can see how the ions are lifted from -1.5 kV to 30 kV. The zoom (bottom) shows that all ions are not lifted at the same place in the electrode because of their different time-of-flight (all ions are lifted at $\approx 172\mu s$ after their ejection from the trap).

Mass measurement mode The ion detector (a Channeltron) for the mass measurement is placed behind the Einzellens (or the focusing electrodes). It is sufficient to focus the beam in the small opening of the Channeltron plate as shown in Figure A.8. The ions will be then sucked on the dynode placed at -4 kV (see Figure A.9) and converted to secondary electrons which are driven to the Channetron cone (- 2 kV) and then detected (details on the Channeltron detection principle can be found in [TEC08]). To tune different voltages (dirft 4-7 & Einzellens) the Simplex optimization routine was used. The Simplex method [NM65] is implemented in the SimIon software and can be easily used via a *lua* program. An example of the results of one optimization is shown in Figure A.8.

The settings of the two examples of the simulation performed for the two modes are shown in Table A.1. The settings of the decay mode listed in this table were used for the commissioning beamtime. The settings from the simulation for the mass measurement mode are not used at the present setup. Different simulations results in this mode did not gave a decent efficiency during the off-line tests. Micro Channel plate (MCP) of 50 mm diameter is now used for mass measurement instead of the Channeltron. This question has to be addressed by checking the alignment of the Channeltron-vacuum chamber with the trap.

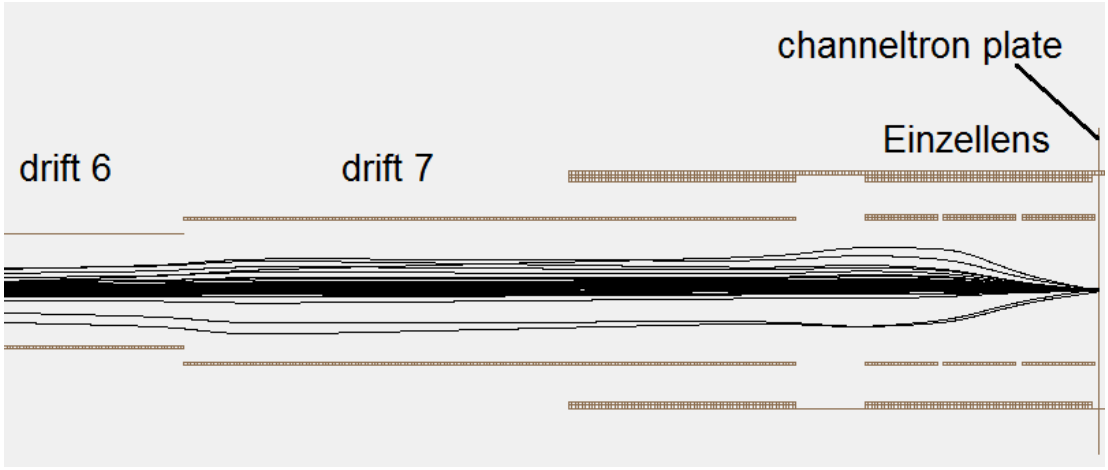

Figure A.8.: Example of trajectory simulation of a bunch of $^{133}Cs^{+}$ ions with SimIon software in the mass measurement mode. The Channeltron ion detector is placed behind the Einzellens. The focusing is performed on the small opening (5 mm diameter) of the Channeltron plate.

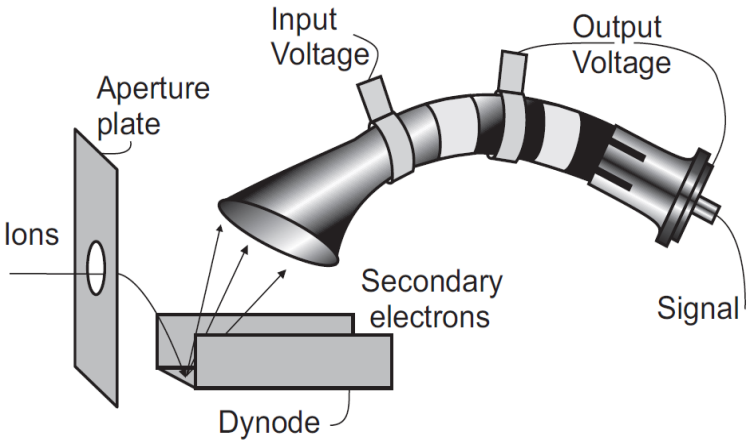

Figure A.9.: Principle of the conversion dynode and connection scheme of the Channeltron detector [TEC08].

Electrode	Spectroscopy mode	Mass measurement mode
Drift 1	-11.5 V	-11.5 V
Drift 2	-200 V	-2.6 V
Drift 3	-400 V	-2.6 V
Drift 4	-460 V	-400 V
Drift 5	-1000 V	-1100 V
Drift 6	-1200 V	-1070 V
Drift 7	-1200 V	-460 V
Einzellens 1	-700 V	-130 V
Einzellens 2	-2300 V	-30 V
Einzellens 3	-700 V	-1000 V
Drift 8	-600 V	not used
Drift 9	-600 V	not used
Pulsed electrode	-1500 V to 30000 V	not used
Drift 10	-1500 V	not used
Drift 11	0 V	not used

Table A.1.: Example of a voltage settings for the two modes: spectroscopy mode and mass measurement mode. The settings shown here correspond to the settings of the simulations illustrated in Figure A.6 and Figure A.8.

A.4. Off-line tests and commissioning

A.4.1. Off-line tests

Before commissioning the setup with radioactive ions, many tests were performed off-line with stable ions or with radioactive sources. The studies using alkali-stable ions from the ISOLTRAP off-line ion source were mostly concentrated on optimizing ion transfer efficiency and partly on the resolving power and sensitivity in the preparation Penning trap. The tests with real ions gave optimal potentials of the electrodes similar to the simulated values. However, the measured transmission was 50% when one collimator was used, and 10% when two collimators were used. Improving the ion transmission is presently one of the main remaining tasks. These off-line tests allowed also optimizing the parameters of the switched electrode which re-accelerates the ions. The energy of the ions was probed by lifting an electrode in front of the last ion detector to + 1000 V. This blocked the non-accelerated ions, but let all accelerated ions through. As a result, close to 100% ions are re-accelerated.

The off-line tests using radioactive sources aimed at optimizing the β and γ-detection efficiency. The β-decay tests were focused on the detection efficiency, since a thin scintillator was used. The solid angle covered by the beta scintillator is around 80%, which sets the upper limit for detection efficiency. Off-line tests with ^{90}Sr source showed the detection efficiency of 50%. For this, a coincidence signal of the two PTMs was used which allowed avoiding the dark counts and non-β background. Although the scintillator is only 2 mm thick, we were also able to obtain partial energy spectra. The

tests of gamma detection efficiency were performed using ^{60}Co (strongest lines at 1173 and 1332 keV), ^{133}Ba (81, 303, 356, 384 keV), and ^{137}Cs sources (662keV). An example of recorded spectra is shown in Figure A.10. The absolute efficiency for each detector at gamma energies around 0.5-0.7 keV was 0.5%, which agrees with rough estimations based on the solid angle covered by each detector and the usual Ge-detection efficiencies for these γ energies. Geant4 simulations and studies of absolute detector efficiencies are presently under way.

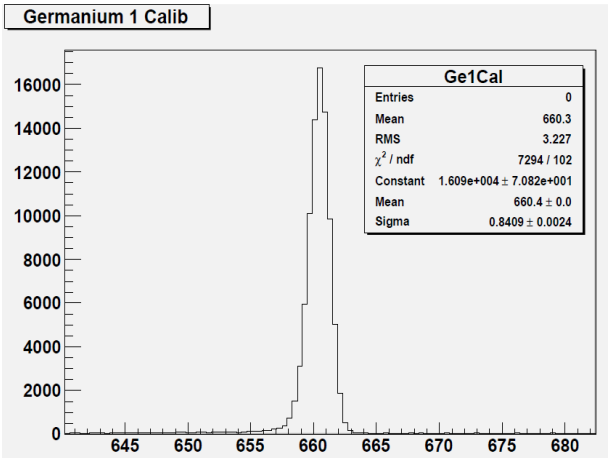

Figure A.10.: The 662-keV line from decay of the 30-kBq ^{137}Cs source placed inside the ISOLTRAP decay-spectroscopy chamber, recorded with one of the ISOLDE Ge-detectors

A.4.2. On-line tests and commissioning

The on-line commissioning run was performed with ^{80}Rb beam, chosen for several reasons:

- it is easily available at ISOLDE, requires only surface ionization, and its production rate is around a dozen pA.
- it has a relatively short half-life of 34 s, which is feasible for β- and γ-studies (decay scheme shown in Figure A.11).
- it decays to stable ^{80}Kr (stable), so in case part of the beam is not moved away with the tape, after several minutes there is no background decay in the detection chamber

The ^{80}Rb beam was produced in a UC_x target, surface ionized, accelerated to 30 keV and mass selected in the ISOLDE high resolution separator (HRS). The measured intensity of the beam in front of the ISOLTRAP buncher was around 5×10^7 ions $/s$. The cooling resonance behind the preparation Penning trap is shown in Figure A.12. It shows the ^{80}Rb peak with no significant ^{80}Sr signal, meaning that the beam was relatively clean.

Between decay measurements, time-of-flight spectra of ^{80}Rb were also recorded. The vacuum was very good already 2-5 minutes after closing the small UHV valve below the

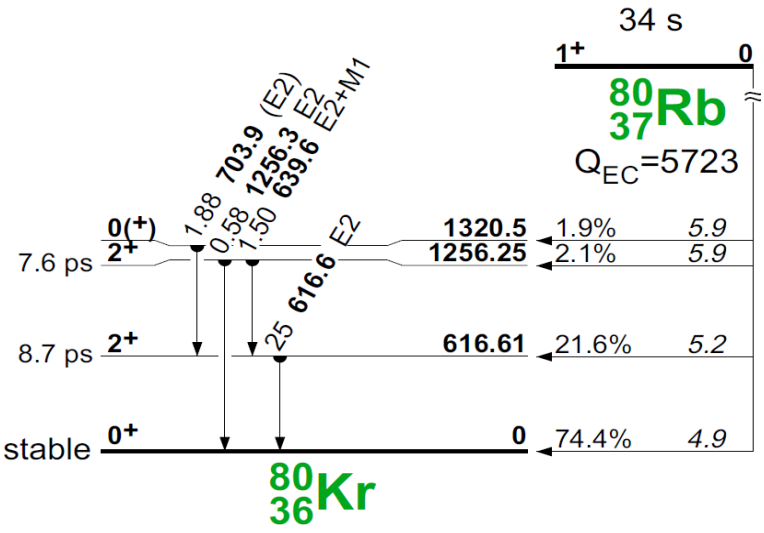

Figure A.11.: Decay scheme of ^{80}Rb (from [Fir+99])

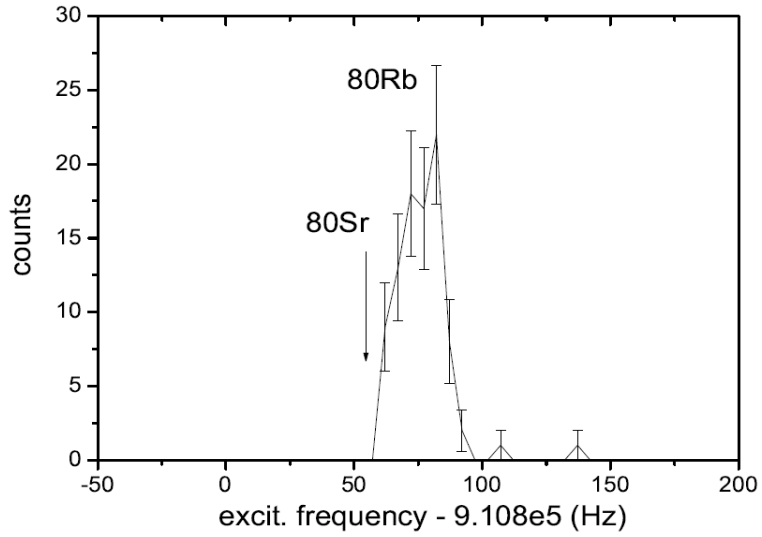

Figure A.12.: Cooling resonance for ^{80}Rb behind the preparation Penning trap. No signal at ^{80}Sr frequency, showing that the ISOLDE beam was clean

detection chamber. Therefore, the damping effects (visible in the decrease of sidebands) were very low and the fit parameters were comparable with those recorded in usual conditions.

Examples of β- and γ- spectra recorded using the ISOLDE β- and γ-DAQ system are shown in Figure A.13. It should be noted that the thin scintillator allowed recording only a partial beta energy spectrum. Two measurement modes were used, as presented in Figure A.14. In the basic mode the ion bunches were implanted all the time into the tape and the β- and γ-spectra were also recorded the whole time. In the other mode, ion bunches implanted in the tape every 600 ms were collected for 50 s (around $3 \times t_{1/2}$) and then the decay was observed for another 100 s, which allowed determining

the ^{80}Rb half-life. The resulting weighted mean value from 4 measurements is 31.7(4.0) s, which agrees well with the literature value of 34 s [Fir+99]. This shows that the ion re-acceleration to 10-20 keV indeed worked and allowed deep enough implantation so that no visible ion losses took place even over a period of several minutes.

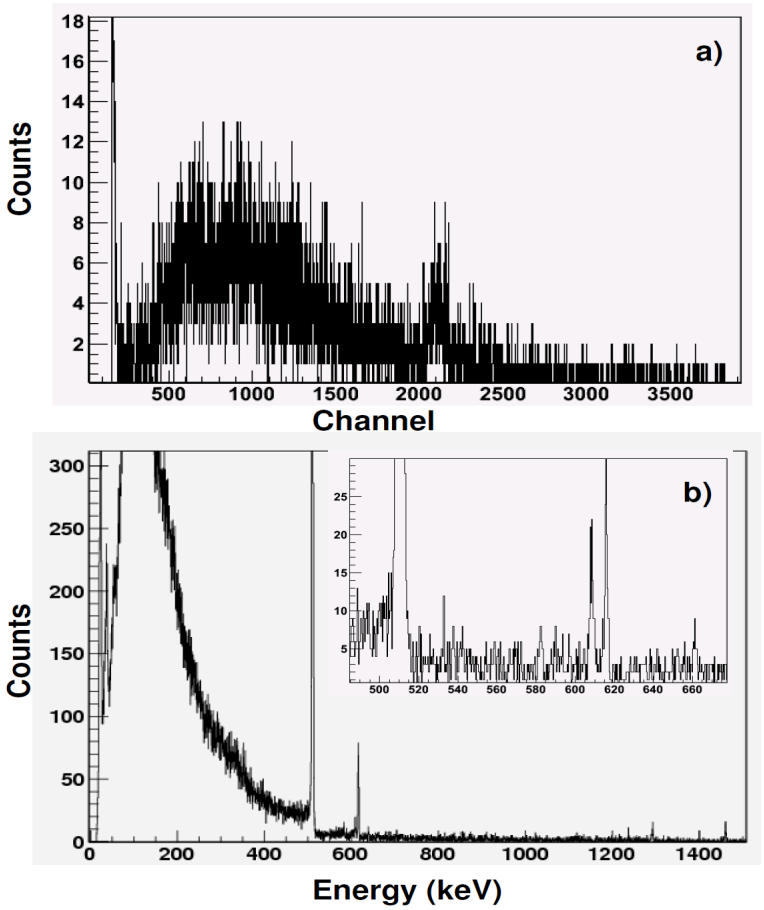

Figure A.13.: Beta (not calibrated) a) and gamma b) spectra recorded during ^{80}Rb implantation into the tape. Rb γ-line is visible at 617 keV.

A.5. Improvement and outlook

Presently, work is under way on the decay spectroscopy system in order to allow optimal ion transfer, detection efficiency, and higher ease of use. This includes simulations of ion behavior in the preparation trap when space charge becomes a problem, in order to see how one can improve the sensitivity and resolution of buffer-gas cooling in presence of many ions [Her+10]. In addition, Geant4 simulations of the present decay chamber are being performed in order to compare the simulated β and γ-spectra with those obtained in experiment. As a second step, the simulations will allow improving the decay chamber so that the signal-to-noise ratio is as good as possible. Also ion trajectory simulations is being performed in electric in magnetic field behind the precision trap

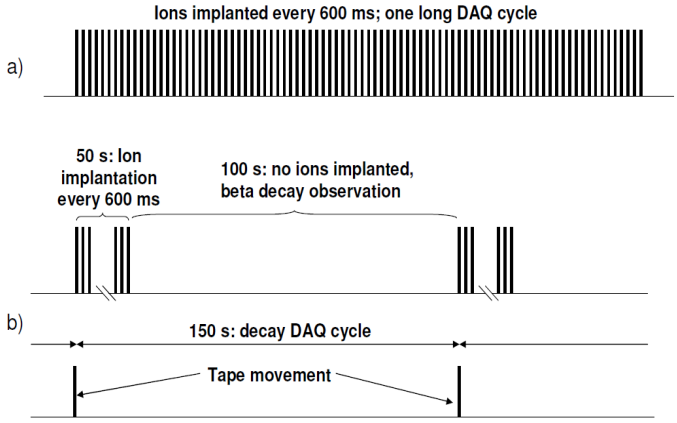

Figure A.14.: Two measuring cycles used in ^{80}Rb tests. a) Basic cycle used for optimizing β- and γ-detection efficiency. b) 150-s cycle used for determining ^{80}Rb half-life, where the daughter radioactivity was carried away on the tape at the end of each cycle.

using the Simion package. The aim is to verify the feasibility of a deflector installed at the height of Channeltron detector, which would allow bending the ion beam into horizontal direction. If possible to obtain a well focused ion beam after such a 90 degree bend in the magnetic field of around 30 Gauss, then one might move the ion optics into the horizontal direction. This would solve the problem of limited height and would for example allow using a third γ-detector on top of the detection chamber. Furthermore, connecting the β and γ-acquisition software to the ISOLTRAP measuring cycle, when in mass-assisted mode, is being investigated. This will allow recording automatically more information on the number of implanted ions, number of implantations, etc, when observing the β and γ-spectra of species whose masses are determined.

B. Kr isotopes resonances

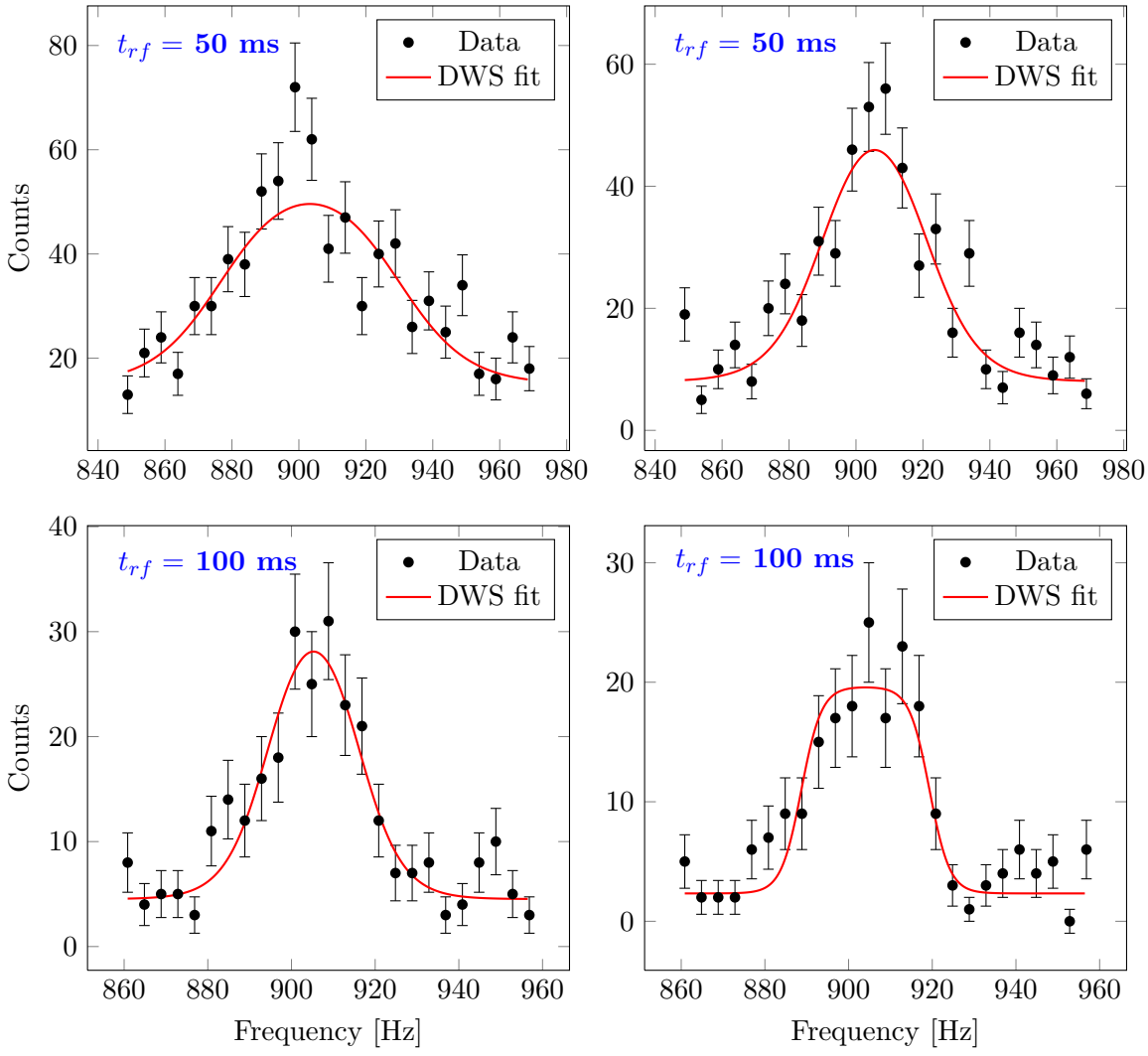

Figure B.1.: Cooling resonances of $^{97}Kr^{+}$ from the preparation Penning trap. Excitation time T_{rf} = 50 ms (top) and T_{rf} =100 ms (bottom).

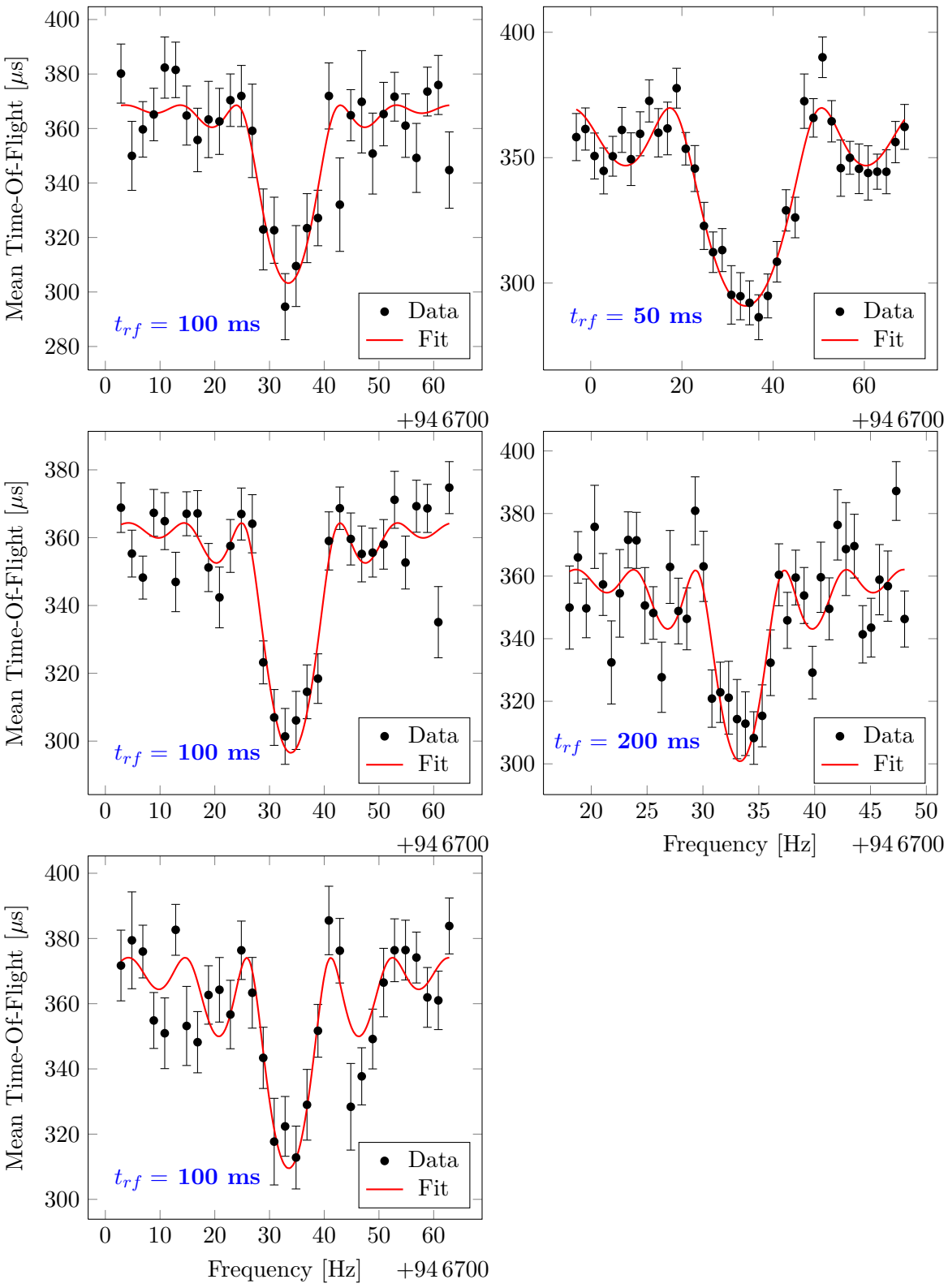

Figure B.2.: TOF resonances of $^{96}Kr^{+}$ from the precision Penning trap. Excitation time T_{rf} = 100 ms (left), T_{rf} = 50 ms (top right) and T_{rf} =200 ms (bottom right).

Bibliography

[Adr+08] P. Adrich et al. "In-beam γ-ray spectroscopy and inclusive two-proton knockout cross section measurements at $N \approx 40$". In: *Phys. Rev. C* 77 (2008), p. 054306.

[ASS69] D. A. Arseniev, A. Sobiczewski, and V. G. Soloviev. "Equilibrium Deformations of Neutron-Rich Nuclei in the A $\approx$ 100 Region". In: *Nucl. Phys. A* 139 (1969), p. 269.

[Aud03] G. Audi. *Nucleus-Win software*. 2003. URL: http://amdc.in2p3.fr/web/nubdisp_fr.html.

[Aud10] G. Audi. "Updated mass table". private communication. 2010.

[AWT03] G. Audi, A. H. Wapstra, and C. Thibault. "The AME2003 atomic mass Evaluation (II). Tables, graphs, and references". In: *Nucl. Phys. A* 729 (2003), p. 337.

[Bai+98] Y. Bai et al. private communication to A.H. Wapstra. 1998.

[Bar+08] S. Baruah et al. "Mass Measurements beyond the Major r-Process Waiting Point ^{80}Zn". In: *Phys. Rev. Lett.* 101 (2008), p. 262501.

[Bec+04] D. Beck et al. "A new control system for ISOLTRAP". In: *Nucl. Instru. and Meth. in Phys. A: Accelerators, Spectrometers, Detectors and Associated Equipment* 527 (2004), pp. 567–579.

[BBH08] M. Bender, G. F. Bertsch, and P.-H. Heenen. "Collectivity-induced quenching of signatures for shell closures". In: *Phys. Rev. C* 78 (2008), p. 054312.

[BBH06] M. Bender, G. F. Bertsch, and P.-H. Heenen. "Global study of quadrupole correlation effects". In: *Phys. Rev. C* 73 (2006), p. 034322.

[Ber+82] M. Bernas et al. "Magic features of 68Ni". In: *Physics Letters B* 113 (1982), pp. 279–282.

[Ber+81] M. Bernas et al. "Masses and Energy Levels of ^{62}Fe and ^{68}Ni: (^{14}C, ^{16}O) Reaction on even Ni and Zn isotopes". In: *Phys. Rev. C* 24 (1981), p. 756.

[Bha+77] T. S. Bhatia et al. "Masses of ^{62}Fe and the New Isotope ^{68}Ni from (^{18}O, ^{20}Ne) Reactions". In: *Z. Phys.* A281 (1977), p. 65.

[Bla06] K. Blaum. "High-accuracy mass spectrometry with stored ions". In: *Phys. Rep.* 425 (2006), pp. 1–78.

[Bla+03] K. Blaum et al. "A novel scheme for a highly selective laser ion source". In: *Nucl. Instru. and Meth. in Phys. B* 204 (2003). 14th International Conference on Electromagnetic Isotope Separators and Techniques Related to their Applications, pp. 331–335.

[Blo+08] M. Block et al. “Discovery of a Nuclear Isomer in ^{65}Fe with Penning Trap Mass Spectrometry”. In: *Phys. Rev. Lett.* 100 (2008), p. 132501.

[Bol+96] G. Bollen et al. “ISOLTRAP: a tandem Penning trap system for accurate on-line mass determination of short-lived isotopes”. In: *Nucl. Instrum. Meth. A* 368 (1996), pp. 675–697.

[Bol+92] G. Bollen et al. “Resolution of nuclear ground and isomeric states by a Penning trap mass spectrometer”. In: *Phys. Rev. C* 46 (1992), R2140–R2143.

[Bos+88] U. Bosch et al. “Beta- and Gamma-Decay Studies of Neutron-Rich Chromium, Manganese, Cobalt and Nickel Isotopes Including the New Isotopes ^{60}Cr and ^{60g}Mn”. In: *Nucl. Phys. A* 477 (1988), p. 89.

[Bro+95] R. Broda et al. “$N = 40$ Neutron Subshell Closure in the ^{68}Ni Nucleus”. In: *Phys. Rev. Lett.* 74 (1995), pp. 868–871.

[Buc+90] F. Buchinger et al. “Systematics of Nuclear Ground State Properties in $^{78-100}$Sr by Laser Spectroscopy”. In: *Phys. Rev. C* 41 (1990), p. 2883.

[Cam+02] P. Campbell et al. “Laser Spectroscopy of Cooled Zirconium Fission Fragments”. In: *Phys. Rev. Lett.* 89 (2002), p. 082501.

[Cam+75] X. Campi et al. “Shape Transition in the Neutron Rich Sodium Isotopes”. In: *Nucl. Phys. A* 251 (1975), p. 193.

[Cas+81] R. F. Casten et al. “Relation between the Z = 64 Shell Closure and the Onset of Deformation at N = 88-90”. In: *Phys. Rev. Lett.* 47 (1981), p. 1433.

[Cas09] R.F. Casten. “Quantum phase transitions and structural evolution in nuclei”. In: *Prog. Part.* 62 (2009), pp. 183–209.

[Cha+09] F. C. Charlwood et al. “Nuclear charge radii of molybdenum fission fragments”. In: *Phys. Lett. B* 674 (2009), p. 23.

[Che+09] B. Cheal et al. “Laser Spectroscopy of Niobium Fission Fragments: First Use of OpticalPumping in an Ion Beam Cooler Buncher”. In: *Phys. Rev. Lett.* 102 (2009), p. 222501.

[Che+10] B. Cheal et al. “Nuclear Spins and Moments of Ga Isotopes Reveal Sudden Structural Changes between $N = 40$ and $N = 50$”. In: *Phys. Rev. Lett.* 104 (2010), p. 252502.

[Che+07] B. Cheal et al. “The shape transition in the neutron-rich yttrium isotopes and isomers”. In: *Phys. Lett. B* 645 (2007), pp. 133–137.

[CTK77] J. D. Cossairt, R. E. Tribble, and R. A. Kenefick. “Masses of ^{61}Fe and ^{62}Fe”. In: *Phys. Rev. C* 15 (1977), p. 1685.

[Dau+00] J. M. Daugas et al. “The 8^+ isomer in ^{78}Zn and the doubly magic character of ^{78}Ni”. In: *Phys. Lett. B* 476 (2000), pp. 213–218.

[Del+06] P. Delahaye et al. “High-accuracy mass measurements of neutron-rich Kr isotopes”. In: *Phys. Rev. C* 74 (2006), p. 034331.

[Del+10] J. P. Delaroche et al. "Structure of even-even nuclei using a mapped collective Hamiltonian and the D1S Gogny interaction". In: *Phys. Rev. C* 81 (2010), p. 014303.

[Del+06] P. Delheij et al. "The TITAN mass measurement facility at TRIUMF-ISAC". In: *Hyper. Interac.* 173 (1 2006), pp. 123–131.

[Dét+79] C. Détraz et al. "Beta decay of $^{27-32}$Na and their descendants". In: *Phys. Rev. C* 19 (1979), pp. 164–176.

[DZ95] J. Duflo and A.P. Zuker. "Microscopic mass formulas". In: *Phys. Rev. C* 52 (1995), R23–R27.

[DH71] N. C. Dyer and J. H. Hamilton. "The Decay of ^{58}Mn". In: *Nucl. Phys. A* 173 (1971), p. 393.

[Els33] Elsasser, W. M. "Sur le principe de Pauli dans les noyaux". In: *J. Phys. Radium* 4 (1933), pp. 549–556.

[Eph+79] M. Epherre et al. "Direct measurements of the masses of rubidium and cesium isotopes far from stability". In: *Phys. Rev. C* 19 (1979), pp. 1504–1522.

[Ess09] H.G. Essel. *New GSI Analysis System GO4*. 2009. URL: http://www-win.gsi.de/go4/.

[Fed+03] V. N. Fedosseev et al. "Atomic spectroscopy studies of short-lived isotopes and nuclear isomer separation with the ISOLDE RILIS". In: *Nucl. Instru. and Meth. in Phys. B* 204 (2003). 14th International Conference on Electromagnetic Isotope Separators and Techniques Related to their Applications, pp. 353–358.

[Fer+10] R. Ferrer et al. "Penning trap mass spectrometry of neutron-rich Fe and Co isotopes around N=40 with the LEBIT mass spectrometer". In: *Phys. Rev. C* 81 (2010), p. 044318.

[Fir+99] R. B. Firestone et al. *Table of Isotopes*. Update. New York: John Wiley and Sons, 1999.

[Fla+09] K. T. Flanagan et al. "Nuclear Spins and Magnetic Moments of ^{71,73,75}Cu: Inversion of $\pi 2p_{3/2}$ and $\pi 1f_{5/2}$ Levels in ^{75}Cu". In: *Phys. Rev. Lett.* 103 (2009), p. 142501.

[FSA77] E. R. Flynn, J. W. Sunier, and F. Ajzenberg-Selove. "States of ^{54}V and ^{58}Mn". In: *Phys. Rev. C* 15 (1977), p. 879.

[Gad+10] A. Gade et al. "Collectivity at $N = 40$ in neutron-rich ^{64}Cr". In: *Phys. Rev. C* 81 (2010), p. 051304.

[GR+05] J. Garcia-Ramos et al. "A theoretical description of energy spectra and two-neutron separation energies for neutron-rich zirconium isotopes". In: *Eur. Phys. J. A* 26 (2005), pp. 221–225.

[Gau05] L. Gaudefroy. "Etude de la fermeture de couche N=28 autour du noyau $^{46}Ar_{28}$ par réaction de transfert d'un neutron : application à l'astrophysique et Spectroscopie $\beta\gamma$ de noyaux riches en neutrons autour de $N = 32/34$ et $N = 40$". PhD thesis. Université Paris XI Orsay, 2005.

[Gau+05] L. Gaudefroy et al. “Beta-decay studies of neutron-rich Sc-Cr nuclei”. In: *Eur. Phys. J. A* 23 (2005), p. 41.

[Gen+06] J. Genevey et al. “First observation of low-lying excited states in the very neutron-rich ^{95}Kr”. In: *Phys. Rev. C* 73 (2006), p. 037308.

[GCP09] S. Goriely, N. Chamel, and J. M. Pearson. “Skyrme-Hartree-Fock-Bogoliubov Nuclear Mass Formulas: Crossing the 0.6 MeV Accuracy Threshold with Microscopically Deduced Pairing”. In: *Phys.Rev.Lett.* 102 (2009), p. 152503.

[GSP07] S. Goriely, M. Samyn, and J. M. Pearson. “Further explorations of Skyrme-Hartree-Fock-Bogoliubov mass formulas. VII. Simultaneous fits to masses and fission barriers”. In: *Phys. Rev. C* 75 (2007), p. 064312.

[GL01] H. Grawe and M. Lewitowicz. “Shell structure of nuclei far from stability”. In: *Nucl. Phys. A* 693 (2001), pp. 116–132.

[Grz+95] R. Grzywacz et al. “Identification of μs-isomers produced in the fragmentation of a ^{112}Sn beam”. In: *Phys. Lett. B* 335 (1995), pp. 439–446.

[Grz+98] R. Grzywacz et al. “New Island of μs Isomers in Neutron-Rich Nuclei around the $Z = 28$ and $N = 40$ Shell Closures”. In: *Phys. Rev. Lett.* 81 (1998), pp. 766–769.

[Gu07] C. Guénaut et al. “High-precision mass measurements of nickel, copper, and gallium isotopes and the purported shell closure at $N = 40$”. In: *Phys. Rev. C* 75 (2007), p. 044303.

[Hag+06] U. Hager et al. “First Precision Mass Measurements of Refractory Fission Fragments”. In: *Phys. Rev. Lett.* 96 (2006), p. 042504.

[Hag+07] U. Hager et al. “Precision mass measurements of neutron-rich yttrium and niobium isotopes”. In: *Nucl. Phys. A* 793 (2007), p. 20.

[Hak+08] J. Hakala et al. “Evolution of the N = 50 Shell Gap Energy towards ^{78}Ni”. In: *Phys. Rev. Lett.* 101 (2008), p. 052502.

[Han+99] M. Hannawald et al. “Decay of Neutron-Rich Mn Nuclides and Deformation of Heavy Fe Isotopes”. In: *Phys. Rev. Lett.* 82 (1999), p. 1391.

[HT09] J. C. Hardy and I. S. Towner. “Superallowed $0^+ \to 0^+$ nuclear B decays: A new survey with precision tests of the conserved vector current hypothesis and the standard model”. In: *Phys. Rev. C* 79 (2009), p. 055502.

[Hau+84] R. Haupt et al. “Mass Excesses of ^{60,62}Fe, ^{68}Ni, ^{69}Cu, ^{74}Zn, ^{73,75}Ga”. In: *Z. Phys.* A317 (1984), p. 193.

[Hau+06] P. A. Hausladen et al. “Opportunistic mass measurements at the Holifield Radioactive Ion BeamFacility”. In: *Int. J. Mass. Spectrom.* 251 (2006), p. 119.

[Her+01] F. Herfurth et al. “A linear radiofrequency ion trap for accumulation, bunching, and emittance improvement of radioactive ion beams”. In: *Nucl. Instrum. Meth. A* 469 (2001), pp. 254–275.

[Her+10] A. Herlert et al. “Effects of space charge on the mass purification in Penning traps”. In: *hyper. interac.* (2010). submitted to Conf. Proc. TCP.

[Her+05] A. Herlert et al. “Mass spectrometry of atomic ions produced by in-trap decay of short-lived nuclides”. In: *New Journal of Physics* 7 (2005), p. 44.

[Hic+76] G. T. Hickey et al. “Mass Measurement of ^{62}Fe Using the ^{64}Ni(^{18}O, ^{20}Ne)^{62}Fe Reaction”. In: *J. Phys.* G2 (1976), p. L143.

[IA87] F. Iachello and A. Arima. *The Interacting Boson Approximation Model*. Cambridge University Press, Cambridge, 1987.

[ICF10] R. Ierusalimschy, W. Celes, and L. H. de Figueiredo. *Lua the programming language*. 2010. URL: http://www.lua.org/.

[Ish+02] T. Ishii et al. “Gamma-ray spectroscopy of the neutron-rich Ni region through heavy-ion deep-inelastic collisions”. In: *Eur. Phys. J. A* 13 (2002), pp. 15–19.

[Joh65] S. A. E. Johansson. “Gamma De-Excitation of Fission Fragments (II). Delayed Radiation”. In: *Nucl. Phys.* 64 (1965), p. 147.

[Jok+06] A. Jokinen et al. “Precision experiments on exotic nuclei at IGISOL”. In: *Int. Jour. Mass. Spectrom.* 251 (2006), pp. 204–211.

[Kas+76] E. Kashy et al. “Observation of Highly Neutron-Rich ^{43}Cl and ^{59}Mn”. In: *Phys. Rev. C* 14 (1976), p. 1773.

[Kei+95] M. Keim et al. “Laser-spectroscopy measurements of 72-96Kr spins, moments and charge radii”. In: *Nucl. Phys. A* 586 (1995), pp. 219–239.

[Kel+01] A. Kellerbauer et al. “Buffer gas cooling of ion beams”. In: *Nucl. Instrum. Meth. A* 469 (2001), pp. 276–285.

[Kel+02] A Kellerbauer et al. “From direct to absolute mass measurements: a study of the accuracy of ISOLTRAP”. In: *Eur. Phys. J. D* 22 (2002), pp. 53–64.

[Knö08] R. Knöbel. “Neuartige Isochrone Massenmessung kurzlebiger neutronenreicher, gespeicherter Kerne am FRS-ESR”. PhD thesis. Justus - Liebig Universität Gießen, 2008.

[Kön+95] M. König et al. “Quadrupole excitation of stored ion motion at the true cyclotron frequency”. In: *Int. J. Mass Spectrom. Ion. Process* 142 (1995), pp. 95–116.

[KH76] O. Kofoed-Hansen. “The birth of on-line isotope separation”. In: *Proc. 3rd Internat. Conf. on Nuclei Far from Stability, Cargèse, France,* 19Ű26 *May 1976, CERN Report* (1976), pp. 65–70.

[Kol+04] V. S. Kolhinen et al. “JYFLTRAP: a cylindrical Penning trap for isobaric beam purification at IGISOL”. In: *Nucl. Instrum. Meth. A* 528 (2004), pp. 776–787.

[Kos02] U. Koster. “Resonance Ionization Laser Ion Sources”. In: *Nucl. Phys. A* 701 (2002), p. 441c.

[Kow+09] M. Kowalska et al. “Preparing a journey to the east of 208Pb with ISOLTRAP: Isobaric purification at A = 209 and new masses for $^{211-213}$Fr and ^{211}Ra”. In: *Eur. Phys. J. A* 42 (2009), pp. 351–359.

[Kre99] M. Kretzschmar. "A quantum mechanical model of Rabi oscillations between two interacting harmonic oscillator modes and the interconversion of modes in a Penning trap". In: *Conf. Proc. TCP, Asilomar, California, AIP Conference Proceedings* 457 (1999), pp. 242–251.

[Kre92] M. Kretzschmar. "Single particle motion in a Penning trap: description in the classical canonical formalism". In: *Phys. Scr.* 46 (1992), p. 544.

[Kös02] U. Köster. "Intense radioactive-ion beams produced with the ISOL method". In: *Eur. Phys. J. A* 15 (2002), pp. 255–263.

[Kug00] E. Kugler. "The ISOLDE facility". In: *Hyper. Interac.* 129 (2000), p. 23.

[Lan+03] K. Langanke et al. "How magic is the magic ^{68}Ni nucleus?" In: *Phys. Rev. C* 67 (2003), p. 044314.

[Lhe+01] G. Lhersonneau et al. "First decay study of the very neutron-rich isotope ^{93}Br". In: *Phys. Rev. C* 63 (2001), p. 034316.

[Lid+04] S. N. Liddick et al. "Development of shell closures at $N = 32, 34$. I. β decay of neutron-rich Sc isotopes". In: *Phys. Rev. C* 70 (2004), p. 064303.

[Lid+06] S. N. Liddick et al. "Half-life and spin of ^{60}Mn^{g}". In: *Phys. Rev. C* 73 (2006), p. 044322.

[Lie+91] P. Lievens et al. "Nuclear Ground State Properties of ^{99}Sr by Collinear Laser Spectroscopy with Non-Optical Detection". In: *Phys. Lett. B* 256 (1991), p. 141.

[Lin04] M. Lindroos. "Review of ISOL-type Radioactive Beam Facilities". In: *Proceedings of EPAC 2004, Lucerne, Switzerland* (2004), pp. 45–49.

[LZ76] S. Liran and N. Zeldes. "A semiempirical shell-model formula". In: *Atomic Data and Nuclear Data Tables* 17 (1976), pp. 431–441.

[Lit+05] Yu.A. Litvinov et al. "Mass measurement of cooled neutron-deficient bismuth projectile fragments with time-resolved Schottky mass spectrometry at the FRS-ESR facility". In: *Nucl. Phys. A* 756 (2005), pp. 3–38.

[Lju+10] J. Ljungvall et al. "Onset of collectivity in neutron-rich Fe isotopes: Toward a new island of inversion?" In: *Phys. Rev. C* 81 (2010), p. 061301.

[Lun08] D. Lunney. "The legacy of A.H. Waspstra and the future of the mass evaluation". In: (2008).

[LPT03] D. Lunney, J. M. Pearson, and C. Thibault. "Recent trends in the determination of nuclear masses". In: *Rev. Mod. Phys.* 75 (2003), p. 1021.

[Mar+09] N. Marginean et al. "Evolution of deformation in the neutron-rich krypton isotopes: The ^{96}Kr nucleus". In: *Phys. Rev. C* 80 (2009), p. 021301.

[Mat+08] Matea, I. et al. "Precise half-life measurement of the ^{26}Si ground state". In: *Eur. Phys. J. A* 37 (2008), pp. 151–158.

[Müc+09] D. Mücher et al. "Shell Structure and Shape Changes in Neutron Rich Krypton Isotopes". In: *AIP Conf. Proc.* 1090 (2009), pp. 587–588.

[Men+08] M. Menna et al. "R and D for the development of negative ion beams of halogens". In: *Nucl. Instru. and Meth. in Phys. B* 266 (2008). Proceedings of the XVth International Conference on Electromagnetic Isotope Separators and Techniques Related to their Applications, pp. 4391–4393.

[Mol+95] P. Moller et al. "Nuclear Ground-State Masses and Deformations". In: *Atomic Data and Nuclear Data Tables* 59 (1995), pp. 185–381.

[MS98] D.J. Morrissey and B.M. Sherrill. "Radioactive nuclear beam facilities based on projectile fragmentation". In: *Phil. Trans. R. Soc. Lond. A* 356 (1998), pp. 1985–2006.

[Muk+08] M. Mukherjee et al. "ISOLTRAP: An on-line Penning trap for mass spectrometry on short-lived nuclides". In: *Eur. Phys. J. A* 35 (2008), p. 1.

[NK08] H.G. Essel N. Kurz. *MBS multi branch system. General purpose DAQ.* 2008. URL: http://www-win.gsi.de/daq/.

[NM65] J. A. Nelder and R. Mead. "A Simplex Method for Function Minimization". In: *The Computer Journal* 7 (1965), pp. 308–313.

[Nor+78] E. B. Norman et al. "Mass and β Decay of the New Neutron-Rich Isotope ^{60}Mn". In: *Phys. Rev. C* 17 (1978), p. 2176.

[Oza+00] A. Ozawa et al. "New Magic Number, $N = 16$, near the Neutron Drip Line". In: *Phys. Rev. Lett.* 84 (2000), pp. 5493–5495.

[Par+77] R. C. Pardo et al. "Mass and Beta Decay of ^{59}Mn". In: *Phys. Rev. C* 16 (1977), p. 370.

[Pau+08] D. Pauwels et al. "Shape isomerism at N = 40: Discovery of a proton intruder state in ^{67}Co". In: *Phys. Rev. C* 78 (2008), p. 041307.

[Pea01] J. Pearson. "The Quest for a Microscopic Nuclear Mass Formula". In: *Hyper. Interac.* 132 (2001), pp. 59–74.

[Pen+08] L. Penescu et al. "Numerical simulations of space charge effects and plasma dynamics for FEBIAD ion sources". In: *Nucl. Instrum. Methods B* 266 (2008), pp. 4415–4419.

[Rah+07] S. Rahaman et al. "Masses of neutron-rich Ni and Cu isotopes and the shell closure at Z = 28, N = 40". In: *Eur. Phys. J. A* 34 (2007), p. 5.

[Rah+06] S. Rahaman et al. "On-line commissioning of SHIPTRAP". In: *Int. J. Mass. Spectrom.* 251 (2006), pp. 146–151.

[RS80] P. Ring and P. Schuck. *The Nuclear Many Body Problem.* Berlin: Springer, 1980.

[Rin+07] R. Ringle et al. In: *Int. J. Mass Spectrom* 262 (2007), pp. 33–44.

[Rin+06] R. Ringle et al. "Precision mass measurements with LEBIT at MSU". In: *Int. Jour. Mass. Spectrom.* 251 (2006), pp. 300–306.

[RA+07] S. Rinta-Antila et al. "Decay study of neutron-rich zirconium isotopes employing a Penning trap as a spectroscopy tool". In: *Eur. Phys. Jour. A* 31 (1 2007), pp. 1–7.

[Ros09] M. Rosenbusch. "Excitation Modes for the Cooling of the Ion motion in Penning Traps". MA thesis. Ernst-Moritz-Arndt-Universität, Greifswald, Germany, 2009.

[Run+85] E. Runte et al. "Decay Studies of Neutron-Rich Isotopes of Manganese, Iron, Cobalt, Nickel, Copper and Zinc". In: *Nucl. Phys. A* 441 (1985), p. 237.

[Sav+91] G. Savard et al. "A new cooling technique for heavy ions in a Penning trap". In: *Phys. Lett. A* 158 (1991), pp. 247–252.

[Sav+01] G. Savard et al. "The Canadian Penning Trap Spectrometer at Argonne". In: *Hyper. Interac.* 132 (2001), pp. 221–228.

[Sch+92] W. D. Schmidt-Ott et al. "Conversion Measurements in the Odd-Odd Isotopes ^{58,60}Mn". In: *Contrib. 6th Intern.Conf.on Nuclei Far from Stability + 9th Intern. Conf. on Atomic Masses and Fundamental Constants*. 1992.

[Sch+08] F. Schwellnus et al. "The laser ion source and trap (LIST) - A highly selective ion source". In: *Nucl. Instru. Meth. Phys. B* 266 (2008). Proceedings of the XVth International Conference on Electromagnetic Isotope Separators and Techniques Related to their Applications, pp. 4383–4386.

[Sei+94] H. L. Seifert et al. "Mass Measurement of Neutron-Rich Isotopes from ^{51}Ca to ^{72}Ni". In: *Z. Phys.* A349 (1994), p. 25.

[Ser06] Scientific Instrument Services. *Simion charged particle optics simulation software*. 2006. URL: http://simion.com/.

[Sor+02] O. Sorlin et al. "^{68}Ni: Magicity versus Superfluidity". In: *Phys. Rev. Lett.* 88 (2002), p. 092501.

[Stu+09] S. Sturm et al. "Investigation of Space-Charge Phenomena in Gas-Filled Penning Traps". In: *AIP Conf. Proc* 1114 (2009), pp. 185–190.

[TEC08] BURLE TECHNOLOGIES. *CHANNELTRON ELECTRON MULTIPLIER HANDBOOK FOR MASS SPECTROMETRY APPLICATIONS*. 2008. URL: http://www.burle.com/cgi/byteserver.pl/pdf/ChannelBook.pdf.

[Thi+75] C. Thibault et al. "Direct measurement of the masses of ^{11}Li and $^{26-32}$Na with an on-line mass spectrometer". In: *Phys. Rev. C* 12 (1975), pp. 644–657.

[Thi+81] C. Thibault et al. "Hyperfine Structure and Isotope Shift of the D_2 Line of $^{76-98}$Rb and Some of their Isomers". In: *Phys. Rev.* 23 (1981), p. 2720.

[Tu+90] X. L. Tu et al. "Direct Mass Measurements of the Neutron-Rich Isotopes of Chlorine through Iron". In: *Z. Phys.* A337 (1990), p. 361.

[Tul10] J. Tuli. *Evaluated Nuclear Structure Data File*. 2010. URL: http://www.nndc.bnl.gov/ensdf/.

[Wan+09] M. Wang et al. "First isochronous mass measurements at CSRe". In: *Int. J. Mod. Phys. E* 18 (2009), pp. 352–357.

[WPK69] T. E. Ward, P. H. Pile, and P. K. Kuroda. "Mn^{58} Isomers". In: *Phys. Rev.* 182 (1969), p. 1186.

[WS54] R. D. Woods and D. S. Saxon. “Diffuse Surface Optical Model for Nucleon-Nuclei Scattering”. In: *Phys. Rev.* 95 (1954), pp. 577–578.

[Xu+09] H. Xu et al. “First mass measurement of short-lived nuclides at HIRFL-CSR”. In: *Chinese Science Bulletin* 54 (2009), pp. 4749–4752.

[Yaz07] C. Yazidjian. “A new detector setup for ISOLTRAP and test of the isobaric multiplet mass equation”. PhD thesis. Université de Caen - Caen, France, 2007.

"Quantum mechanics means anything can happen at any time for no reason"

Professor Farnsworth, year 3000, Futurama